

**UCLA**

**UCLA Electronic Theses and Dissertations**

**Title**

Rapid Biophysical Characterization of Cancer Cells by Quantitative Deformability Cytometry

**Permalink**

<https://escholarship.org/uc/item/92v4c839>

**Author**

Nyberg, Kendra Dee

**Publication Date**

2017

Peer reviewed|Thesis/dissertation

UNIVERSITY OF CALIFORNIA

Los Angeles

Rapid Biophysical Characterization of Cancer Cells  
by Quantitative Deformability Cytometry

A dissertation submitted in partial satisfaction of the  
requirements for the degree Doctor of Philosophy  
in Bioengineering

by

Kendra Dee Nyberg

2017

© Copyright by  
Kendra Dee Nyberg  
2017

## ABSTRACT OF THE DISSERTATION

Rapid Biophysical Characterization of Cancer Cells

by Quantitative Deformability Cytometry

by

Kendra Dee Nyberg

Doctor of Philosophy in Bioengineering

University of California, Los Angeles, 2017

Professor Amy Catherine Rowat, Chair

Cells are complex, viscoelastic materials that undergo changes in their mechanical phenotype, or ‘mechanotype’, during diverse physiological and disease processes, such as malignant transformation. As cancer cells exhibit altered cell mechanical properties compared to their benign counterparts, cell mechanotype is an emerging hallmark of cancer and demonstrates potential to enhance cancer detection and classification. However, widespread adoption of cell mechanotype as a clinical biomarker for cancer requires standardized metrics for high throughput mechanotyping measurements.

This dissertation presents a microfluidic platform, quantitative deformability cytometry (q-DC), for rapid, calibrated measurements of single-cell mechanical properties. Cells are driven to deform through micron-scale constrictions at 100 cells/second, while changes in cell strain are tracked by a high-speed camera. The applied mechanical stresses induced by the driving pressure are determined using gel calibration particles, which enables calibrated measurements of elastic modulus and fluidity from the single-cell stress-strain relationships. Additional physical properties, such as cell size, strain, transit time, and creep time, are also measured for individual cells by q-DC. This dissertation highlights a comprehensive methodology for

designing, analyzing, and reducing variability in q-DC measurements; the calibration method for measuring the applied stress in the microfluidic channels; and the influence of stress and strain in q-DC mechanotyping.

This dissertation also demonstrates how multiple physical phenotypes from q-DC can be used to distinguish human cancer cell lines and predict the ability of cells to invade through a matrix. A physical phenotyping model of invasion is trained and validated using breast and ovarian human cancer cell lines with both genetic and pharmacologic perturbations, which correctly predicts the invasion of five cancer cell samples; whereas one context is identified where the model does not accurately predict invasion. Taken together, this work lays the groundwork for calibration in high throughput mechanotyping methods, demonstrates the predictive power of multiple physical phenotypes for cell invasion, and incites deeper investigation into additional predictive markers for cancer cell invasion.

The dissertation of Kendra Dee Nyberg is approved.

Dino Di Carlo

Siavash K. Kurdistani

Gerard Chee Lai Wong

Amy Catherine Rowat, Committee Chair

University of California, Los Angeles

2017

## DEDICATION

I dedicate this dissertation to my loving mother and father. You cultivate a life for me full of curiosity, challenges and opportunities. Thank you for supporting me through my endless, unpredictable endeavors and for helping me hone in on this one. I also recognize my mentors who believed in me when I didn't believe in myself. This work is for you—Miriam, Raghu, Vinny, Gerard, and Amy. Lastly, I would like to thank Colin Mulligan; I am forever grateful for your support and encouragement throughout this journey.

## TABLE OF CONTENTS

Acknowledgements .....	vii
Vita .....	viii
Introduction.....	1
Chapter 1: The Physical Origins of Transit Time Measurements .....	11
Chapter 2: Quantitative Deformability Cytometry.....	41
Chapter 3: Prediction of Cancer Cell Invasion by Quantitative Deformability Cytometry.....	88



## ACKNOWLEDGEMENTS

**Chapter 1.** Adapted from Nyberg, *et al.* 2016, *Lab on a Chip*. KDN and ACR designed the experiments and wrote the manuscript. KDN, SLB, DB, and TGM performed experiments. KDN, MBS, SLB, and ABG developed the data analysis code.

**Chapter 2.** Adapted from Nyberg, *et al.* 2017, *Biophysical Journal*. KDN and ACR designed the experiments and wrote the manuscript. KDN, KHH, SHK and MJB performed experiments. KDN designed and implemented the q-DC algorithm. DBK performed simulations.

**Chapter 3.** Adapted from Nyberg, *et al.*, submitted to *Integrative Biology*, 2017. KDN and ACR designed experiments and prepared the manuscript. KDN, AVN, CKC, NKG, and THK performed experiments. KDN and SLB designed, implemented and evaluated machine learning algorithms. EKS provided guidance throughout the manuscript and study.

Cells and microRNAs were generously gifted from Don and Ada Olins (HL-60 cell line), Timothy Donahue (pancreatic ductal adenocarcinoma cell lines), Ming-Sound Tsao (non-transformed human pancreatic ductal epithelial (HPDE) cell line), Preethi Gunaratne (tumor-suppressor microRNAs), and Ruprecht Wiedemeyer and Barbie Taylor-Harding (OVCA433-GFP and Snail-expressing cell lines).

Art Evans, Alex Levine, Ben Fabry, Howard Stone, and Massoud Karimzadeh provided fruitful discussions throughout the work. The Integrated Systems Nanofabrication Cleanroom at the California NanoSystems Institute and its staff supported the fabrication of the microfluidic devices through training and facilities.

The work has been supported by the National Science Foundation (CAREER DBI-1254185 to ACR), Broad Stem Cell Research Center, UCLA Life Sciences Innovation Fund Award, UCLA Dissertation Year Fellowship, and the Farber Family Foundation.

## VITA

### EDUCATION

**M.S., Bioengineering**, *specialization in Biomedical Instrumentation* (2014)

University of California, Los Angeles

**B.S., Physics**, *Departmental Honors* (2012)

University of Oregon

### HONORS

**Dissertation Year Fellowship** (2017), Graduate Division, UCLA

**Distinguished Teaching Assistant Award** (2017), Academic Senate Committee on Teaching, UCLA

**Farber Family Scholar** (2014 - 2017), Farber Family Scholarship, Los Angeles, CA

**Biomedical Engineering Fellowship** (2012, 2017), Bioengineering Department, UCLA

**University Fellowship** (2013), Bioengineering Department, UCLA

**Weiser Leadership Award** (2012), Physics Department, UO

**Science Literacy Program Fellow** (2011 - 2012), Howard Hughes Medical Institute and UO

### RESEARCH POSITIONS

**Bioengineering Graduate Student Researcher** (2012 - 2017), University of California, Los Angeles

Rowat Lab – Integrative Biology and Physiology Department

**Biophysics Undergraduate Student Researcher** (2009 - 2012), University of Oregon

Parthasarathy Lab – Physics Department

**Research Experience for Undergraduates Fellow** (2011), University of California, Berkeley

Fletcher Lab – Bioengineering Department

**Research Experience for Undergraduates Fellow** (2010), Harvard University

Manoharan Lab – Physics Department

## PUBLICATIONS

1. **Nyberg KD**, Bruce SL, Nguyen AV, Chan CK, Gill NK, Kim TH, Sloan EK, Rowat AC. “Label-free prediction of cancer cell invasion by single-cell physical phenotyping.” *Submitted. Integrative Biology*.
2. **Nyberg KD**, Hu KH, Kleinman SH, Khismatullin DB, Butte MJ, Rowat AC. “Quantitative Deformability Cytometry (q-DC): rapid, calibrated measurements of single cell viscoelastic properties.” (2017) *Biophysical Journal*. 113(7): 1574-1584.
3. Gill NK, Qi D, Kim TH, Chan CK, Nguyen AV, **Nyberg KD**, Rowat AC. “A protocol for screening cells based on deformability using parallel microfiltration.” (2017) *Nature Protocol Exchange*.
4. Evans AA, Cheung E, **Nyberg KD**, Rowat AC. “Wrinkling of milk skin is mediated by evaporation.” (2017) *Soft Matter*. 13(5): 1056-1062.
5. Chan CK, Pan Y, **Nyberg KD**, Lim E, Robertson G, Maar D, Gunaratne PH, Rowat AC. “Tumour-suppressor microRNAs regulate ovarian cancer cell physical properties and invasive behaviour.” (2016) *Open Biology*. 6(11): 160275.
6. Kim TH, Gill NK, **Nyberg KD**, Nguyen AV, Hohlbauch SV, Geisse NA, Nowell CJ, Sloan E, Rowat AC. “Cancer cells are less deformable and more invasive with activation of  $\beta$ -adrenergic signaling.” (2016) *Journal of Cell Science*. 129(24): 4563-4575.
7. Nguyen AV, **Nyberg KD**, Scott MB, Nguyen A, Hohlbauch SV, Geisse NA, Robertson G, Gibb E, Welsh A, Wu N, Donahue T, Rowat AC. “Stiffness of pancreatic cancer cells is associated with increased invasive potential.” (2016) *Integrative Biology*. 8(12): 1232-1245.
8. **Nyberg KD**, Scott MB, Bruce SL, Gopinath AB, Bikos D, Mason TG, Kim JW, Choi HS, Rowat AC. “The physical origins of transit time measurements for rapid, single cell mechanotyping.” (2016) *Lab on a Chip*. 16: 3330 - 3339.
9. Zhou L, **Nyberg KD**, Rowat AC. “Understanding Fick’s law and diffusion theory through food & cooking.” (2015) *Advances in Physiology Education*. 39: 192–197.

## INTRODUCTION

Changes in cell physical properties are implicated in diverse physiological and disease phenomena, ranging from stem cell differentiation to malignant transformation. For example, cell and nuclear morphology is broadly used in cytology (1–3), while the stiffness of a mass is assessed for initial cancer detection (4). The deformability of single cells, or the ability for a cell to deform under a mechanical load, is also emerging as a label-free biomarker to enhance clinical decision-making and diagnosis (5–7). Altered cell deformability is especially relevant in cancer, where more invasive cancer cells tend to be more deformable than their benign counterparts (8–14). While the origins of altered cell deformability in cancer are not well understood, measurements of the mechanical phenotype of cells, or ‘mechanotype’, demonstrate the utility of mechanotype in cancer classification and diagnosis (15). The mechanical signature of cancer cells also incites deeper biophysical questions, such as whether altered mechanotype solely reflects altered genetic and epigenetic regulation or if it provides a selective advantage during metastasis.

Standardized measurements of cell mechanotype include elastic modulus,  $E$ , compliance,  $J$ , and viscosity,  $\eta$ . Such measurements are achieved by probing cells with well-defined stresses and measuring the resultant deformations using atomic force microscopy (AFM) (11, 14, 16), micropipette aspiration (17–19), optical stretching (20–23), and microplate compression (24, 25). These standardized measurements provide valuable insights into the physical principles that underlie cell mechanical properties, including viscoelastic and stress stiffening behaviors (26–28), as well as the passive and active contributions of cytoskeletal and nuclear structures in cell mechanotype (14, 29–34). Identifying such physical and molecular origins of cell mechanotype deepen our understanding of the role of cell mechanical properties in physiology and disease; however, measurements of mechanical moduli, such as those obtained using AFM or micropipette aspiration, are acquired at rates of  $<1$  cell/min. Widespread adoption of cell mechanotyping in both clinical and research settings requires higher throughput to efficiently assess large cell samples.

Fluid-based deformability cytometry (DC) methods enable rapid, single-cell measurements of cell deformability at faster rates of  $10^2 - 10^6$  cells per minute. With the transit DC method, cells are driven to deform and transit through microfluidic constrictions on millisecond timescales (13, 21, 35–41). The time required for cells to transit through microfluidic constrictions can depend on cell size, mechanical properties, and surface properties, but the initial deformation into microfluidic constrictions is dominated by cell deformability (39, 40, 42); Such transit experiments are widely used to mechanotype various cell types from breast cancer cells to neutrophils based on relative deformation timescales (13, 35). In the DC method using a cross-slot microfluidic channel, the hydrodynamic forces of inertial flow deform cells at faster timescales on the order of microseconds, and provide relative measurements of deformability (43). In the real-time DC (rt-DC) method, the shear stresses of fluid flow induce cell deformations on millisecond to microsecond timescales (44). These shape changes are well described by a continuum elastic model (45), which enable single-cell measurements of elastic modulus (44).

While such DC methods highlight the promising applications of rapid mechanotype in classifying cells at different stages of the cell cycle (44) and identifying pluripotent stem cells from their lineages (46), cells are non-linear materials, and fluid-based mechanotyping methods are susceptible to varying applied strains and stresses (47). In AFM studies, the influence of length and time scales of deformation on elastic modulus measurements are observed in cells (26–28, 48–51) and biopolymer networks (26, 48, 52–54). For example, cells exhibit strain-stiffening behavior (16). Cells are also spatially heterogeneous materials, where the nucleus is typically 2- to 5-times stiffer than the surrounding cytoplasmic region (14). Therefore, the magnitude of deformation depth, or strain, may impact the resultant mechanotype measurements. Additionally, stress stiffening behavior of cells is also observed across varying cell types from airway smooth muscle cells to fibroblasts (23, 26, 48, 55). Therefore, successful translation of mechanotyping to clinical and research applications calls for a deeper understanding of the influence of applied strain and stress in high throughput mechanotyping measurements. Moreover, an established calibration standard for

fluid-based mechanotyping methods that addresses fluctuations in applied strain and stress will also further advance the adoption of high throughput mechanotyping.

This dissertation highlights a method for rapid, calibrated, single-cell mechanotyping using quantitative deformability cytometry (q-DC). An applied pressure gradient is used to drive cells to deform through micron-scale constrictions of a transit-based DC microfluidic device at rates of thousands of cells per minute (47). To obtain standardized measurements of cell mechanotype, the time-dependent strain of an individual cell is tracked and the applied stress is calibrated using gel particles with well-defined elastic moduli. As the time-dependent strain of single cells follows power law rheology (PLR), apparent elastic modulus,  $E_a$ , and power law exponent,  $\beta$  or fluidity, is acquired for individual cells. Using human promyelocytic leukemia (HL-60) cells as a model system,  $E_a$  is observed to increase with cell strain and applied stress on these time and length scales, which further substantiates the importance of calibration standards in mechanotyping measurements. q-DC is also shown to be sensitive to changes in HL-60 mechanotype following treatment with cytoskeletal-perturbing drugs and differences in the mechanotype between human breast cancer cell lines, MCF-7 and MDA-MB-231 cells.

In addition to laying a foundation for calibration in rapid mechanotyping measurements, this dissertation also investigates the power of mechanotyping for predicting functional cancer phenotypes. Specifically, *in vitro* invasion provides an experimental model for the ability of cells to metastasize *in vivo*. Predicting disease and treatment outcomes based on single cell phenotypes is critical in medicine from cancer diagnosis to stem cell therapies. In clinical oncology and immunology, single cell analysis of protein markers and DNA content using flow cytometry is used for diagnosis, prognosis, and monitoring patient response to therapy (56). Yet pathological and physiological changes can also manifest as altered cell physical phenotypes, including cell and nuclear size, stiffness, and viscosity, which are convenient, label-free biomarkers. While DC methods have demonstrated the potential for mechanotyping in classification of cancer cells, the association between single-cell physical properties and invasion could establish physical phenotype biomarkers for cancer prognosis.

By performing q-DC mechanotyping across well-established pancreatic cancer cell lines as well as ovarian cancer cells that overexpress tumor-suppressor microRNAs, a predictive physical phenotyping model for invasion is trained and assessed against both genetic and pharmacologic perturbations of cancer cells. The q-DC method for single-cell physical phenotyping coupled with machine learning algorithms establishes a framework for predicting invasion based on label-free biomarkers that can be rapidly measured. The ability of q-DC to enable calibrated, multiparameter cell physical phenotyping to classify cell types and predict cellular behaviors is valuable for biomedical applications, and should offer unprecedented insight into the biophysical properties of cells and their link to disease progression.

## References

1. Elston, C.W., and I.O. Ellis. 1991. Pathological prognostic factors in breast cancer. I. The value of histological grade in breast cancer: experience from a large study with long-term follow-up. *Histopathology*. 19: 403–410.
2. Webster, M., K.L. Witkin, and O. Cohen-Fix. 2009. Sizing up the nucleus: nuclear shape, size and nuclear-envelope assembly. *J. Cell Sci.* 122: 1477–86.
3. Guilak, F., J.R. Tedrow, and R. Burgkart. 2000. Viscoelastic properties of the cell nucleus. *Biochem. Biophys. Res. Commun.* 269: 781–786.
4. Lyman, G.H., A.E. Giuliano, M.R. Somerfield, A.B. 3rd Benson, D.C. Bodurka, H.J. Burstein, A.J. Cochran, H.S. 3rd Cody, S.B. Edge, S. Galper, J.A. Hayman, T.Y. Kim, C.L. Perkins, D.A. Podoloff, V.H. Sivasubramaniam, R.R. Turner, R. Wahl, D.L. Weaver, A.C. Wolff, and E.P. Winer. 2005. American Society of Clinical Oncology guideline recommendations for sentinel lymph node biopsy in early-stage breast cancer. *J. Clin. Oncol.* 23: 7703–7720.
5. Bongiorno, T., J.L. Chojnowski, J.D. Lauderdale, and T. Sulchek. 2016. Cellular Stiffness as a Novel Stemness Marker in the Corneal Limbus. *Biophys. J.* 111: 1761–1772.
6. Bongiorno, T., J. Kazlow, R. Mezencev, S. Griffiths, R. Olivares-Navarrete, J.F. McDonald, Z.

- Schwartz, B.D. Boyan, T.C. McDevitt, and T. Sulchek. 2014. Mechanical stiffness as an improved single-cell indicator of osteoblastic human mesenchymal stem cell differentiation. *J. Biomech.* 47: 2197–2204.
7. Tse, H.T.K., D.R. Gossett, Y.S. Moon, M. Masaeli, M. Sohsman, Y. Ying, K. Mislick, R.P. Adams, J. Rao, and D. Di Carlo. 2013. Quantitative diagnosis of malignant pleural effusions by single-cell mechanophenotyping. *Sci. Transl. Med.* 5: 212ra163.
  8. Guck, J., S. Schinkinger, B. Lincoln, F. Wottawah, S. Ebert, M. Romeyke, D. Lenz, H.M. Erickson, R. Ananthakrishnan, D. Mitchell, others, J. Käs, S. Ulvick, and C. Bilby. 2005. Optical deformability as an inherent cell marker for testing malignant transformation and metastatic competence. *Biophys. J.* 88: 3689–98.
  9. Cross, S.E., Y.-S. Jin, J. Rao, and J.K. Gimzewski. 2007. Nanomechanical analysis of cells from cancer patients. *Nat. Nanotechnol.* 2: 780–3.
  10. Hur, S.C., N.K. Henderson-MacLennan, E.R.B. McCabe, and D. Di Carlo. 2011. Deformability-based cell classification and enrichment using inertial microfluidics. *Lab Chip.* 11: 912–920.
  11. Xu, W., R. Mezencev, B. Kim, L. Wang, J. McDonald, and T. Sulchek. 2012. Cell stiffness is a biomarker of the metastatic potential of ovarian cancer cells. *PLoS One.* 7: e46609.
  12. Swaminathan, V., K. Mythreye, E.T. O’Brien, A. Berchuck, G.C. Blobe, and R. Superfine. 2011. Mechanical stiffness grades metastatic potential in patient tumor cells and in cancer cell lines. *Cancer Res.* 71: 5075–5080.
  13. Hou, H.W., Q.S. Li, G.Y.H. Lee, a. P. Kumar, C.N. Ong, and C.T. Lim. 2009. Deformability study of breast cancer cells using microfluidics. *Biomed. Microdevices.* 11: 557–564.
  14. Agus, D.B., J.F. Alexander, W. Arap, S. Ashili, J.E. Aslan, R.H. Austin, V. Backman, K.J. Bethel, R. Bonneau, W.-C. Chen, C. Chen-Tanyolac, N.C. Choi, S.A. Curley, M. Dallas, D. Damania, P.C.W. Davies, P. Decuzzi, L. Dickinson, L. Estevez-Salmeron, V. Estrella, M. Ferrari, C.



- Fischbach, J. Foo, S.I. Fraley, C. Frantz, A. Fuhrmann, P. Gascard, R.A. Gatenby, Y. Geng, S. Gerecht, R.J. Gillies, B. Godin, W.M. Grady, A. Greenfield, C. Hemphill, B.L. Hempstead, A. Hielscher, W.D. Hillis, E.C. Holland, A. Ibrahim-Hashim, T. Jacks, R.H. Johnson, A. Joo, J.E. Katz, L. Kelbaskas, C. Kesselman, M.R. King, K. Konstantopoulos, C.M. Kraning-Rush, P. Kuhn, K. Kung, B. Kwee, J.N. Lakins, G. Lambert, D. Liao, J.D. Licht, J.T. Liphardt, L. Liu, M.C. Lloyd, A. Lyubimova, P. Mallick, J. Marko, O.J.T. McCarty, D.R. Meldrum, F. Michor, S.M. Mumenthaler, V. Nandakumar, T. V O'Halloran, S. Oh, R. Pasqualini, M.J. Paszek, K.G. Philips, C.S. Poultney, K. Rana, C.A. Reinhart-King, R. Ros, G.L. Semenza, P. Senechal, M.L. Shuler, S. Srinivasan, J.R. Staunton, Y. Stypula, H. Subramanian, T.D. Tlsty, G.W. Tormoen, Y. Tseng, A. van Oudenaarden, S.S. Verbridge, J.C. Wan, V.M. Weaver, J. Widom, C. Will, D. Wirtz, J. Wojtkowiak, and P.-H. Wu. 2013. A physical sciences network characterization of non-tumorigenic and metastatic cells. *Sci. Rep.* 3: 1449.
15. Henry, T.K., D.R. Gossett, Y.S. Moon, M. Masaeli, M. Sohsman, Y. Ying, K. Mislick, R.P. Adams, J. Rao, and D. Di Carlo. 2013. Quantitative diagnosis of malignant pleural effusions by single-cell mechanophenotyping. *Sci. Transl. Med.* 5: 212ra163--212ra163.
  16. Rotsch, C., and M. Radmacher. 2000. Drug-induced changes of cytoskeletal structure and mechanics in fibroblasts: an atomic force microscopy study. *Biophys. J.* 78: 520–535.
  17. Evans, E., and A. Yeung. 1989. Apparent viscosity and cortical tension of blood granulocytes determined by micropipet aspiration. *Biophys. J.* 56: 151–160.
  18. Needham, D., and R.M. Hochmuth. 1990. Rapid flow of passive neutrophils into a 4 microns pipet and measurement of cytoplasmic viscosity. *J. Biomech. Eng.* 112: 269–76.
  19. Tsai, M.A., R.S. Frank, and R.E. Waugh. 1993. Passive mechanical behavior of human neutrophils: power-law fluid. *Biophys. J.* 65: 2078–2088.
  20. Zhang, H., and K.-K. Liu. 2008. Optical tweezers for single cells. *J. R. Soc. Interface.* 5: 671–690.

21. Ekpenyong, A.E., G. Whyte, K. Chalut, S. Pagliara, F. Lautenschläger, C. Fiddler, S. Paschke, U.F. Keyser, E.R. Chilvers, and J. Guck. 2012. Viscoelastic Properties of Differentiating Blood Cells Are Fate- and Function-Dependent. *PLoS One*. 7.
22. Guck, J., S. Schinkinger, B. Lincoln, F. Wottawah, S. Ebert, M. Romeyke, D. Lenz, H.M. Erickson, R. Ananthakrishnan, D. Mitchell, J. Käs, S. Ulvick, and C. Bilby. 2005. Optical Deformability as an Inherent Cell Marker for Testing Malignant Transformation and Metastatic Competence. *Biophys. J.* 88: 3689–3698.
23. Maloney, J.M., D. Nikova, F. Lautenschläger, E. Clarke, R. Langer, J. Guck, and K.J. Van Vliet. 2010. Mesenchymal stem cell mechanics from the attached to the suspended state. *Biophys. J.* 99: 2479–87.
24. Thoumine, O., and A. Ott. 1997. Time scale dependent viscoelastic and contractile regimes in fibroblasts probed by microplate manipulation. *J. Cell Sci.* 110 ( Pt 1: 2109–2116.
25. Caille, N., O. Thoumine, Y. Tardy, and J.-J. Meister. 2002. Contribution of the nucleus to the mechanical properties of endothelial cells. *J. Biomech.* 35: 177–187.
26. Fabry, B., G.N. Maksym, J.P. Butler, M. Glogauer, D. Navajas, and J.J. Fredberg. 2001. Scaling the microrheology of living cells. *Phys. Rev. Lett.* 87: 148102.
27. Desprat, N., A. Richert, J. Simeon, and A. Asnacios. 2005. Creep function of a single living cell. *Biophys. J.* 88: 2224–2233.
28. Deng, L., X. Trepate, J.P. Butler, E. Millet, K.G. Morgan, D.A. Weitz, and J.J. Fredberg. 2006. Fast and slow dynamics of the cytoskeleton. *Nat. Mater.* 5: 636–640.
29. Martens, J.C., and M. Radmacher. 2008. Softening of the actin cytoskeleton by inhibition of myosin II. *Pflugers Arch. Eur. J. Physiol.* 456: 95–100.
30. Murrell, M., P.W. Oakes, M. Lenz, and M.L. Gardel. 2015. Forcing cells into shape: the mechanics of actomyosin contractility. *Nat. Rev. Mol. Cell Biol.* 16: 486–498.

31. Wang, N., K. Naruse, D. Stamenovic, J.J. Fredberg, S.M. Mijailovich, I.M. Tolic-Norrelykke, T. Polte, R. Mannix, and D.E. Ingber. 2001. Mechanical behavior in living cells consistent with the tensegrity model. *Proc. Natl. Acad. Sci. U. S. A.* 98: 7765–7770.
32. Wang, N., I.M. Tolic-Norrelykke, J. Chen, S.M. Mijailovich, J.P. Butler, J.J. Fredberg, and D. Stamenovic. 2002. Cell prestress. I. Stiffness and prestress are closely associated in adherent contractile cells. *Am. J. Physiol. Cell Physiol.* 282: C606-16.
33. Park, C.Y., D. Tambe, A.M. Alencar, X. Trepate, E.H. Zhou, E. Millet, J.P. Butler, and J.J. Fredberg. 2010. Mapping the cytoskeletal prestress. *Am. J. Physiol. Cell Physiol.* 298: C1245-52.
34. Jalilian, I., C. Heu, H. Cheng, H. Freittag, M. Desouza, J.R. Stehn, N.S. Bryce, R.M. Whan, E.C. Hardeman, T. Fath, G. Schevzov, and P.W. Gunning. 2015. Cell elasticity is regulated by the tropomyosin isoform composition of the actin cytoskeleton. *PLoS One.* 10: e0126214.
35. Rosenbluth, M.J., W.A. Lam, and D.A. Fletcher. 2008. Analyzing cell mechanics in hematologic diseases with microfluidic biophysical flow cytometry. *Lab Chip.* 8: 1062–1070.
36. Rowat, A.C., D.E. Jaalouk, M. Zwerger, W.L. Ung, I.A. Eydellant, D.E. Olins, A.L. Olins, H. Herrmann, D.A. Weitz, and J. Lammerding. 2013. Nuclear Envelope Composition Determines the Ability of Neutrophil-type Cells to Passage through Micron-scale Constrictions. *J. Biol. Chem.* 288: 8610–8618.
37. Hoelzle, D.J., B.A. Varghese, C.K. Chan, and A.C. Rowat. 2014. A Microfluidic Technique to Probe Cell Deformability. *JoVE.* 91: e51474–e51474.
38. Lange, J.R., J. Steinwachs, T. Kolb, L.A. Lautscham, I. Harder, G. Whyte, and B. Fabry. 2015. Microconstriction Arrays for High-Throughput Quantitative Measurements of Cell Mechanical Properties. *Biophys. J.* 109: 26–34.
39. Byun, S., S. Son, D. Amodei, N. Cermak, J. Shaw, J.H. Kang, V.C. Hecht, M.M. Winslow, T. Jacks, P. Mallick, and S.R. Manalis. 2013. Characterizing deformability and surface friction of

- cancer cells. *Proc. Natl. Acad. Sci.* 110: 7580–7585.
40. Shaw Bagnall, J., S. Byun, S. Begum, D.T. Miyamoto, V.C. Hecht, S. Maheswaran, S.L. Stott, M. Toner, R.O. Hynes, and S.R. Manalis. 2015. Deformability of Tumor Cells versus Blood Cells. *Sci. Rep.* 5: 18542.
  41. Lange, J.R., C. Metzner, S. Richter, W. Schneider, M. Spermann, T. Kolb, G. Whyte, and B. Fabry. 2017. Unbiased High-Precision Cell Mechanical Measurements with Microconstrictions. *Biophys. J.* 112: 1472–1480.
  42. Nyberg, K.D., M.B. Scott, S.L. Bruce, A.B. Gopinath, D. Bikos, T.G. Mason, J.W. Kim, H.S. Choi, and A.C. Rowat. 2016. The physical origins of transit time measurements for rapid, single cell mechanotyping. *Lab Chip.* 16: 3330–3339.
  43. Gossett, D.R., H.T.K. Tse, S. a. Lee, Y. Ying, A.G. Lindgren, O.O. Yang, J. Rao, A.T. Clark, and D. Di Carlo. 2012. Hydrodynamic stretching of single cells for large population mechanical phenotyping. *Proc. Natl. Acad. Sci.* 109: 7630–5.
  44. Otto, O., P. Rosendahl, A. Mietke, S. Golfier, C. Herold, D. Klaue, S. Girardo, S. Pagliara, A. Ekpenyong, A. Jacobi, M. Wobus, N. Töpfner, U.F. Keyser, J. Mansfeld, E. Fischer-Friedrich, and J. Guck. 2015. Real-time deformability cytometry: on-the-fly cell mechanical phenotyping. *Nat. Methods.* 12.
  45. Mietke, A., O. Otto, S. Girardo, P. Rosendahl, A. Taubenberger, S. Golfier, E. Ulbricht, S. Aland, J. Guck, and E. Fischer-Friedrich. 2015. Extracting Cell Stiffness from Real-Time Deformability Cytometry: Theory and Experiment. *Biophys. J.* 109: 2023–2036.
  46. Lin, J., D. Kim, T.T. Henry, P. Tseng, L. Peng, M. Dhar, S. Karumbayaram, and D. Di Carlo. 2017. High-throughput physical phenotyping of cell differentiation. *Microsystems Nanoeng.* 3: 17013.
  47. Nyberg, K.D., K.H. Hu, S.H. Kleinman, D.B. Khismatullin, M.J. Butte, and A.C. Rowat. 2017.

- Quantitative Deformability Cytometry (q-DC): rapid, calibrated measurements of single cell viscoelastic properties. *Biophys. J.* in press.
48. Fernandez, P., P.A. Pullarkat, and A. Ott. 2006. A master relation defines the nonlinear viscoelasticity of single fibroblasts. *Biophys. J.* 90: 3796–3805.
  49. Marcy, Y., J. Prost, M.-F. Carrier, and C. Sykes. 2004. Forces generated during actin-based propulsion: a direct measurement by micromanipulation. *Proc. Natl. Acad. Sci.* 101: 5992–5997.
  50. Bieling, P., T.-D. Li, J. Weichsel, R. McGorty, P. Jreij, B. Huang, D.A. Fletcher, and R.D. Mullins. 2016. Force Feedback Controls Motor Activity and Mechanical Properties of Self-Assembling Branched Actin Networks. *Cell.* 164: 115–127.
  51. Icard-Arcizet, D., O. Cardoso, A. Richert, and S. Henon. 2008. Cell stiffening in response to external stress is correlated to actin recruitment. *Biophys. J.* 94: 2906–2913.
  52. Hoffman, B.D., G. Massiera, K.M. Van Citters, and J.C. Crocker. 2006. The consensus mechanics of cultured mammalian cells. *Proc. Natl. Acad. Sci.* 103: 10259–10264.
  53. Janmey, P.A., U. Euteneuer, P. Traub, and M. Schliwa. 1991. Viscoelastic properties of vimentin compared with other filamentous biopolymer networks. *J. Cell Biol.* 113: 155–160.
  54. Gardel, M.L., F. Nakamura, J.H. Hartwig, J.C. Crocker, T.P. Stossel, and D.A. Weitz. 2006. Prestressed F-actin networks cross-linked by hinged filamins replicate mechanical properties of cells. *Proc. Natl. Acad. Sci.* 103: 1762–1767.
  55. An, S.S., R.E. Laudadio, J. Lai, R.A. Rogers, and J.J. Fredberg. 2002. Stiffness changes in cultured airway smooth muscle cells. *Am. J. Physiol. Physiol.* 283: C792--C801.
  56. Brown, M., and C. Wittwer. 2000. Flow cytometry: principles and clinical applications in hematology. *Clin. Chem.* 46: 1221–1229.

## CHAPTER 1

### *The Physical Origins of Transit Time Measurements for Rapid, Single-cell Mechanotyping*

#### **Abstract**

The mechanical phenotype or ‘mechanotype’ of cells is emerging as a potential biomarker for cell types ranging from pluripotent stem cells to cancer cells. Using a microfluidic device, cell mechanotype can be rapidly analyzed by measuring the time required for cells to deform as they flow through constricted channels. While cells typically exhibit deformation timescales, or transit times, on the order of milliseconds to tens of seconds, transit times can span several orders of magnitude and vary from day to day within a population of single cells; this makes it challenging to characterize different cell samples based on transit time data. Here we investigate how variability in transit time measurements depends on both experimental factors and heterogeneity in physical properties across a population of single cells. We find that simultaneous transit events that occur across neighboring constrictions can alter transit time, but only significantly when more than 65% of channels in the parallel array are occluded. Variability in transit time measurements is also affected by the age of the device following plasma treatment, which could be attributed to changes in channel surface properties. We additionally investigate the role of variability in cell physical properties. Transit time depends on cell size; by binning transit time data for cells of similar diameters, we reduce measurement variability by 20%. To gain further insight into the effects of cell-to-cell differences in physical properties, we fabricate a panel of gel particles and oil droplets with tunable mechanical properties. We demonstrate that particles with homogeneous composition exhibit a marked reduction in transit time variability, suggesting that the width of transit time distributions reflects the degree of heterogeneity in subcellular structure and mechanical properties within a cell population. Our results also provide fundamental insight into the physical underpinnings of transit measurements: transit time depends strongly on particle elastic modulus, and weakly on viscosity and

surface tension. Based on our findings, we present a comprehensive methodology for designing, analyzing, and reducing variability in transit time measurements; this should facilitate broader implementation of transit experiments for rapid mechanical phenotyping in basic research and clinical settings.

## **Introduction**

Changes in cell mechanical properties are implicated in diverse physiological and disease phenomena, ranging from stem cell differentiation to malignant transformation. Cell mechanical phenotype or ‘mechanotype’ is thus emerging as a powerful, label-free biomarker to enhance clinical decision-making and diagnosis (1). Quantitative measurements of mechanotype also facilitate a deeper understanding of the origins of altered cell physical properties. While methods such as micropipette aspiration (2), atomic force microscopy (AFM) (3, 4), and optical stretching (5) provide detailed insight into cytoskeletal and nuclear contributions to cell mechanotype, measurements are typically limited to 10 to  $10^2$  cells per hour. Fluid-based deformation cytometry techniques enable mechanotype measurements at faster rates of 10 to  $10^4$  cells per minute by tracking cells as they are deformed during flow through microfluidic constrictions or by inertial fluid flows (6–11). Microfluidics also enable integration of complementary methods to assay additional physical properties of cells, such as their electrical conductivity and membrane capacitance, as well as the ability to sort cells based on these physical features (12–16).

In microfluidic transit experiments, cells are driven to pass through micron-scale constrictions at rates of 1 to  $10^3$  cells per second by applying a pressure gradient (17) or constant volume flow (6). As cells flow through the constrictions, they deform through gaps that are up to  $\sim 3\times$  smaller than their initial diameter; the timescale for a single cell to transit through a constriction provides a measure of its deformability. This mechanotyping method demonstrates that highly metastatic cancer cells have shorter transit times compared to less metastatic cells (9) and leukemia cells treated with chemotherapy drugs exhibit longer transit times compared to DMSO-treated control cells (6). While transit measurements for cell mechanotyping are relatively simple and fast, there is significant variability in transit times that typically

spans two to three orders of magnitude within a population of single cells. Such marked spread in transit times, in addition to measurement variability between experiments, make it challenging to use this method to robustly compare different cell types.

The broad distributions of transit times could result from phenotypic variability across a population of isogenic cells. For example, cell size varies across a population, and larger cells tend to have longer transit times (9, 18). However, even for cells with similar size ( $\pm 5\%$ ,  $\sim 1 \mu\text{m}$ ), transit times range over an order of magnitude (9, 18). In addition to size, cells from the same population exhibit order-of-magnitude differences in elastic modulus and viscosity, as measured by atomic force microscopy (4, 6, 19), micropipette aspiration (20–23), and optical stretching (5, 24). While stiffer cells have longer transit times (25), the degree to which cell-to-cell heterogeneity in mechanical properties contribute to transit time variability is not well understood. Moreover, cells are viscoelastic materials and the relative contributions of elasticity and viscosity to transit measurements remain unclear. While longer transit times are associated with stiffer cells that have higher elastic moduli (25), the time required for cells to enter microfluidic constrictions is also well predicted by the shear thinning liquid drop model, which describes a cell as a purely viscous material (9); this makes it challenging to obtain a deeper knowledge of cell mechanical properties from transit time data.

Experimental factors may also affect the width of transit time distributions. For example, the entry velocity of cells into micron-scale pores depends on channel surface properties (9) as well as the pressure drop across a cell (23). The impact of surface properties is especially critical when considering cell transit through polydimethylsiloxane (PDMS) channels, which are commonly plasma treated to enable covalent bonding to glass; however, this renders channels hydrophilic up to 48 hours post treatment (26), and the influence of channel hydrophilicity on transit time variability is not well characterized. Moreover, as multiple cells simultaneously transit through the device, channel occlusions can alter flow rates, and thus entry velocities of cells into neighboring constrictions (18); transient lane occlusions may thus also contribute to variation in transit time both within and across experiments.



Here we investigate the role of extrinsic and intrinsic factors in transit time variability with the goal of establishing more robust measurements of cell mechanotype. Using HL-60 cells as a model system, we provide a framework to reduce transit time variability due to cell size, PDMS surface properties, and transient lane occupancies. By fabricating a panel of gel and oil particles with well-defined material properties, we investigate the extent to which the broad distribution in transit times results from mechanical heterogeneity across a population. Our study also provides valuable insight into the physical underpinnings of transit time measurements, revealing that elasticity dominates transit on these millisecond timescales.

### **Device Design and Concept**

**Microfluidic device design.** In transit time experiments, cell deformability is determined by flowing cells through micron-scale constrictions and measuring the timescale of their transit (6–9, 18). Our microfluidic device consists of a branching network of channels that extends into an array of 16 parallel lanes, where each lane contains a series of constrictions (27) (Fig. 1A, B). Cells enter the device through the inlet and first passage through a downstream filter, which helps to remove extraneous contaminants, such as chunks of PDMS that can result from device fabrication, as well as cell aggregates that are larger than 20  $\mu\text{m}$  (Fig. 1A). After passing through the bifurcating channels, the cells reach the constrictions, which have a height of 5.3  $\mu\text{m}$  and width of 5.2  $\mu\text{m}$  (Fig. 1A, B). To transit through these constrictions, the HL-60 cells must deform down to ~40% of their original diameter.

To drive cell suspensions through the microfluidic channels, we apply air pressure, which ensures a constant pressure drop across the microfluidic device. The magnitude of applied pressure dictates the velocity of both the fluid and particles as they flow through the device. For a particle to deform through the constriction, a minimum threshold pressure,  $P_T$ , must be applied to induce sufficient strain of the particle. When the driving pressure,  $P_{driving}$ , is less than  $P_T$ , the particle will occlude the constriction over the experimental timescale, which is on the order of minutes. We find that  $P_{driving} = 28$  kPa (4 psi) is an adequate driving pressure, which exceeds  $P_T$  for HL-60 cell and ensures sufficient tracking of individual

cells and particles.  $P_{driving}$  also dictates the frequency with which cells reach the constrictions; with  $P_{driving} = 28$  kPa and a  $5.3 \times 5.2 \mu\text{m}^2$  constriction, we can achieve transit events at rates of  $\sim 10^2$  cells/min for cell suspensions with a density of  $2 \times 10^6$  cells/mL.

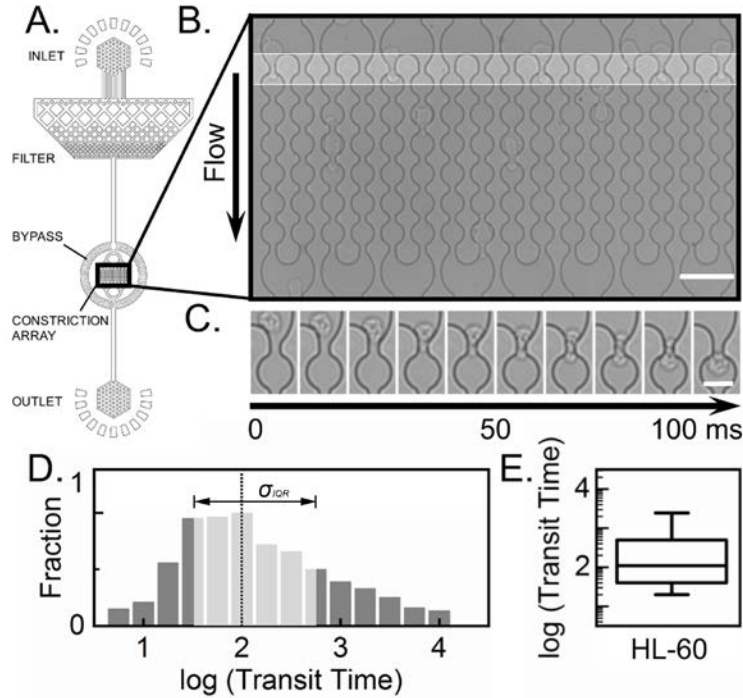


**Fig. 1. Overview of microfluidic device for measuring transit time.** (A) Schematic of the microfluidic device. Suspension of cells/particles enters the device through the inlet. Filters reduce the frequency of clusters of cells and larger particulates that are  $> 20 \mu\text{m}$  from entering the constriction array. Bypass channels help to minimize fluctuations in pressure as particles transit through the device. (B) Brightfield image of the constriction array, which consists of 16 channels that each have a series of  $5 \mu\text{m}$  constrictions. Transit time is defined as the time required for the leading edge of the cell to enter and exit the constriction region, which is denoted by the lighter gray region. Scale,  $50 \mu\text{m}$ ; (C) Time series of a single cell during transit through a  $5 \mu\text{m}$  constriction. The representative cell shown here has a transit time of 80 ms. Scale,  $20 \mu\text{m}$ . (D) Histogram and (E) boxplot of transit times for HL-60 cells. In the histogram, light gray boxes represent the interquartile range, and dotted line represents the median. In the boxplot, the line represents the median, the box represents the interquartile range, and the whiskers represent the 10<sup>th</sup> and 90<sup>th</sup> percentiles.

To determine the transit time of an individual cell, we track its projected area and measure the time required for its leading edge to enter and subsequently exit the constriction region (Fig. 1C). To ensure that each cell has a similar initial state, we measure transit time data only from the first row of constrictions; additional analyses of cell deformation and relaxation responses can be obtained from the transit through subsequent constrictions within each lane. By tracking hundreds of cells for each sample, we generate a histogram of transit times. For a single population of HL-60 cells, we observe median transit times that are on the order of tens to hundreds of milliseconds and vary over three orders of magnitude when  $P_{driving} = 28$  kPa and the constriction is  $5.3 \times 5.2 \mu\text{m}^2$  (Fig. 1D). Since transit times exhibit non-normal distributions, we evaluate the width of a distribution using the bootstrapped interquartile range of the log-transformed data. As shown in Fig. 1D, the bootstrapped interquartile range and confidence interval of the log transform for HL-60 cells are  $\sigma_{IQR} = 1.1 \pm 0.1$ .

**Time and length scales of cell transit.** On these tens to hundreds of millisecond timescales, we estimate that transit time measurements predominantly reflect the passive deformation response of cells as they deform through microfluidic constrictions; this passive deformation response of cells is largely determined by the organization and levels of mechanoregulating proteins, such as actin and tubulin; pharmacological perturbations of both actin and microtubules significantly alter transit times on both millisecond (18) and second (6, 25, 28) timescales. Over longer timescales, cells may additionally invoke active responses to mechanical loads: actomyosin contractions and transcriptional regulation can occur on the order of minutes, while protein levels are regulated on the order of minutes to hours.

**Pressure drop across the constriction region.** As multiple cells simultaneously transit through and occlude the bifurcated array of channels, the fluidic resistance, and thus flow rates, can fluctuate, which can impact the rate at which cells transit through constrictions. We design our microfluidic device to minimize inconsistencies in transit time that may arise from having an array of constrictions. For an array of parallel channels, the fluidic resistance is described by Kirchhoff's Law:

$$\frac{1}{R_{total}} = \frac{1}{R_{bypass}} + \frac{1}{R_{L1}} + \frac{1}{R_{L2}} + \dots + \frac{1}{R_{LN}}. \quad (\text{Eq. 1})$$

Here,  $R_{total}$  is the total fluidic resistance along the cross-section of the channels;  $R_{bypass}$  is the fluidic resistance of the bypass channel; and  $R_{LN}$  is the fluidic resistance of  $N$  individual lanes. For a microfluidic channel with a rectangular cross-section, the relationship between the fluidic resistance, the channel height,  $h$ , and width,  $w$ , is given by the Hagen-Poiseuille relation,  $R \propto \frac{1}{wh^3}$ .

Eq. 1 illustrates how the fluidic resistance can fluctuate as multiple cells transit through the device and transiently obstruct channels. To minimize the effect of simultaneous transit events on transit time, we design our microfluidic device to reduce fluctuations in fluidic resistance due to lane occlusions: by maximizing the number of lanes that can fit into the camera's field of view with a 20 $\times$  objective, we reduce the impact of a single occlusion on the total fluidic resistance. To further buffer changes in fluidic resistance, we also include a wide bypass channel ( $5.3 \times 300 \mu\text{m}^2$ ) that surrounds the constriction region (Fig 1A).

Based on Eq. 1, we estimate that the fluidic resistance will change by <1% when a single cell transits through the array of constrictions. However, during a transit experiment, the number of occupied lanes ranges between 1 and 16 lanes; when all 16 lanes are occupied, the fluidic resistance can increase up to ~12%. To determine the effect of fluctuating lane occupancy on transit time variability and enable more robust measurements, we perform a detailed analysis of transit time as a function of lane occupancy.

## Results and Discussion

**Transient occlusions affect transit time.** With our experimental conditions of  $P_{driving} = 28$  kPa and  $5.3 \times 5.2 \mu\text{m}^2$  constrictions, we find that on average  $9.2 \pm 2.7$  out of 16 lanes are occupied during the transit of an individual HL-60 cell (Fig. 2A). For 1 to 10 lane occupancies, we observe no statistical difference between transit time distributions (Fig. 2B). However, when more than ten channels are occluded (>65% of total channels), there is a significant decrease in transit times (Fig. 2B). While our data shows a slight

increase in transit times for 15 or 16 occlusions, this near-complete occlusion of all lanes happens infrequently (<1% of all transit events), so the resultant effects on cell transit time are inconclusive.

To reduce the variability in transit time that results from transient occlusion of channels, we exclude cell transit events that occur while more than ten channels are occupied. We additionally exclude cells that transit while multiple cells occupy the same lane, since this reduces the pressure drop across a single cell. Channel obstructions can also occur in regions that are outside of the field of view that we monitor during a transit experiment, such as in the filter and bypass regions. However, inspection of these regions after measurement acquisition reveals a sparse number of occluding particles or cell aggregates, which are small compared to the total cross sectional area of the filter and bypass channel. Nonetheless, to minimize any effects of unobserved occlusions, we use a new device for each video.

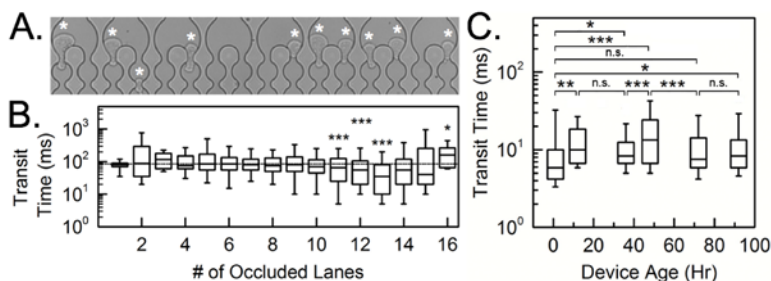


**Fig. 2. Effect of extrinsic sources on transit time variability: transient lane occlusion and PDMS surface properties.** (A) Brightfield image of the constriction array with 10 occupied lanes, which are denoted by the white asterisks. (B) Transit time versus the number of lane occlusions. Statistical significance compares the transit time distribution of each lane to the preceding lane using Mann-Whitney U. (C) Cell transit time as a function of the hours following plasma treatment. Statistical significance shown between the transit time distribution of each device age and the preceding time point using Mann-Whitney U. \* for  $p < 0.05$ , \*\* for  $p < 0.01$ , \*\*\* for  $p < 0.001$ .

**Age of PDMS device after plasma treatment impacts transit time.** While PDMS is inherently hydrophobic, the device walls become more hydrophilic for up to 48 hours following plasma treatment (26), which is commonly used to bond PDMS to the glass substrate. Since transit time can vary depending on the surface charge of microfluidic channels (9), we next investigate how the age of the device

following plasma treatment affects transit time. We conduct transit measurements using devices at 1, 12, 36, 48, 72 and 96 hours following plasma treatment. Compared to transit times that are obtained using a device that is aged for one hour, our results show a significant increase in transit times when measurements are performed 12 or more hours after plasma treatment. While we observe differences in the distributions of transit times at time points beyond 12 hours, there is no significant trend towards increasing or decreasing transit times. Thus, to reduce variability in transit times due to differences in device age, we conduct experiments 24 hours after plasma treatment and bonding. Consistently using 24 hour-aged devices also minimizes error that may arise from differences in the material properties of PDMS as the elastic modulus can increase by 180% following the initial cure (29); this could impact the physical stresses on the cell during transit.

**Transit time scales with cell size.** To determine how variations in cell physical properties impact transit time measurements, we first consider the effects of cell size. The diameter of HL-60 cells ranges from 10 to 21  $\mu\text{m}$  (Fig. 3A.ii.), with a median of 15  $\mu\text{m}$ . By tracking the projected area of cells as they transit through the constrictions, we observe that transit time increases with cell size; these observations are consistent with previous studies (9, 18) (Fig 3A.iii). To determine the scaling relation between transit time and cell size, we measure the median transit times for twelve size bins of 0.5  $\mu\text{m}$  within the interquartile range of projected diameters, ranging from 19 – 25  $\mu\text{m}$ . Performing linear regression on the log-transformed data reveals that transit time has a strong dependence on cell size (slope = 5.8 and  $R^2 = 0.87$ ). By size-filtering our transit time data, we observe a 18% reduction in the variability of transit times for cells of the median size  $\pm 5\%$  (1  $\mu\text{m}$ ) with a resultant  $\sigma_{QR} = 0.9 \pm 0.1$  (Fig. 3A.vi).

**Reduced variability for particles with uniform composition.** Variability in transit time could also result from cell-to-cell differences in mechanotype. The viscous and elastic moduli of cells are largely determined by subcellular organization and structural proteins, which vary in expression level across a population of single cells. To assess particles that have uniform composition and well-defined mechanical properties (30), we fabricate gel particles and oil droplets that have a similar size as HL-60 cells (Fig.

3B.ii., 3C.ii.). Our panel of agarose gel particles exhibits a range of elastic moduli from 3.1 to 43 kPa (S. Fig. 3); this range of elastic moduli is achieved by varying the polymer density within the droplets of a water-in-oil emulsion. We also generate oil-in-water emulsions with silicone oils that have a range of viscosities from  $10^{-2}$  to  $10^2$  Pa·s. In addition, we use a surfactant that enables us to regulate the surface tension of oil droplets.

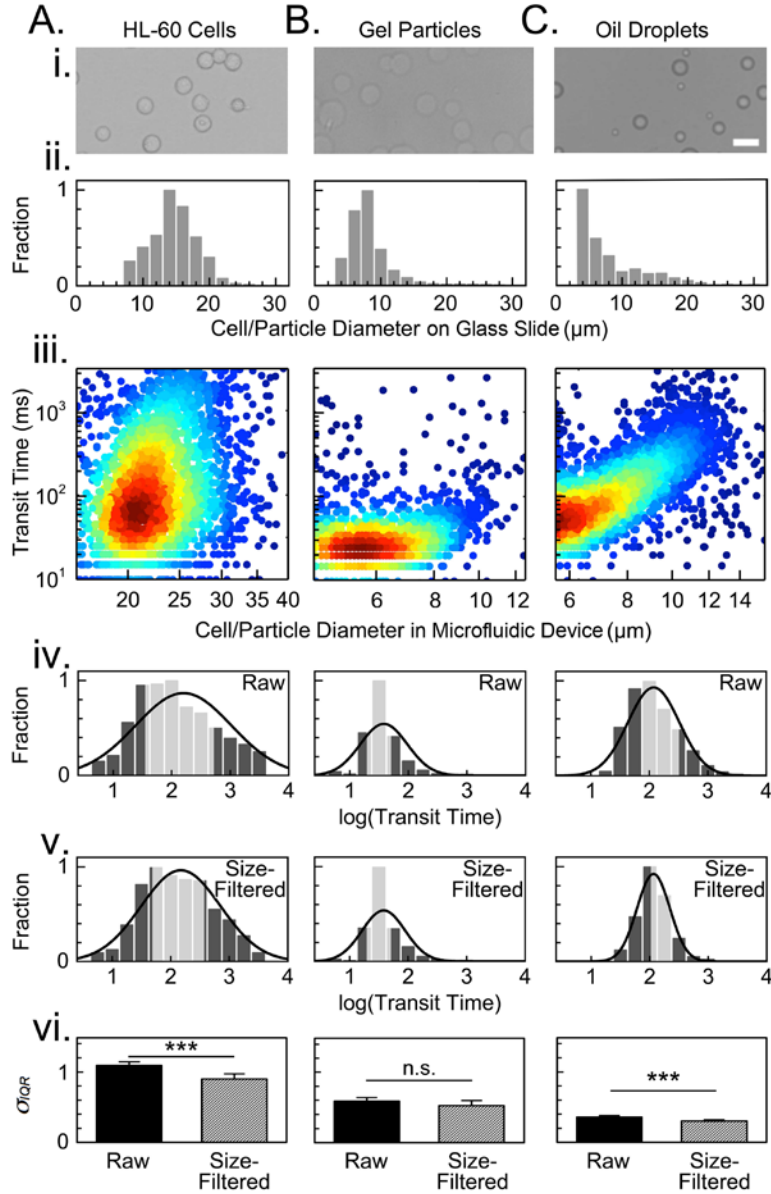


**Fig. 3. Size and transit time distributions for cells and particles.** (i) Brightfield images of (A) HL-60 cells, (B) representative agarose gel particles ( $E = 8.7$  kPa), and (C) representative silicone

oil droplets ( $\eta = 10^2$  Pa s) on a glass slide. Scale, 15  $\mu\text{m}$ . (ii) Histograms of cell/particle sizes on a glass slide. (iii) Density scatter plots of transit time versus cell/particle diameter as determined during flow through the microfluidic device. Color represents density of data points. Cells appear larger when they are compressed in the 5.2  $\mu\text{m}$ -high channels of the microfluidic device; the gel and oil particles appear smaller in the microfluidic device as the larger particles are trapped in the filter upstream from the constriction region. (iv) Transit time distributions for (A) HL-60 cells, (B) representative agarose gel particles ( $E = 8.7$  kPa), and (C) representative silicone oil droplets ( $\eta = 10^2$  Pa·s). (v) Size-filtered transit time distributions for cells and particles with diameters of the median value  $\pm 5\%$ . For cells, the median diameter is 22  $\mu\text{m}$  and for gel and oil particles, the median diameter is 7  $\mu\text{m}$ . The black line overlaying the histogram represents the fitted log-normal distribution. The gray bars represent the interquartile ranges. (vi) average bootstrapped log-transformed interquartile ranges,  $\sigma_{IQR}$ , for transit time distributions across the panels of  $E$  and  $\eta$  of the raw data (solid bar) and the size-filtered data (striped bar). Error bars represent the bootstrapped confidence intervals. Statistical significance is determined using the t-test. \*\*\* for  $p < 0.001$ .

Both gel particles and oil droplets deform through the constrictions of the microfluidic device using the same experimental conditions that are used for cell transit measurements. As the particles flow through the constrictions, we track their size and transit time. While we observe a modest size dependence for the oil droplets, we observe no significant size dependence for our gel particles (Fig. 3B.iii, 3C.iii). To reduce any scaling bias and consistently compare the width of transit time distributions for cells, oil droplets, and gel particles, we filter data for all cells/particles based on the median particle size ( $7 \pm 1$   $\mu\text{m}$ ). Across our panel of particles within our median size filter, gel particles exhibit an average  $\sigma_{IQR} = 0.5 \pm 0.2$  (Fig. 3B.vi); oil droplets have an average  $\sigma_{IQR} = 0.3 \pm 0.0$  (Fig. 3C.vi). The reduction of  $\sigma_{IQR}$  for oil droplets compared to gel particles may be attributed to the uniform molecular composition of the silicone oils; by contrast, spatial heterogeneities within the agarose particles could result from variations in the fabrication process; variability in the elastic moduli of agarose gel microspheres is observed by atomic force microscopy where the standard deviation can vary up to 10% (30). Compared to both gel and oil particles, HL-60 cells have a significantly higher  $\sigma_{IQR} = 0.9 \pm 0.1$  (Fig. 3A.vi); this is consistent with our hypothesis



that heterogeneity in the structure and/or mechanotype of single cells is a major contributor to transit time variability.

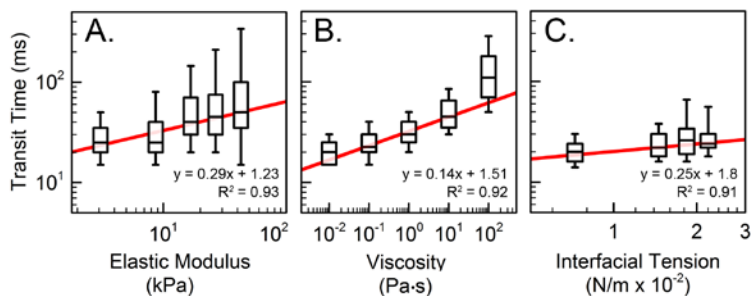


**Fig. 4 Transit time depends on particle mechanical properties.** Transit times for (A) agarose gel particles with increasing elastic modulus; (B) silicone oil droplets with increasing viscosity; and (C) silicone oil droplets with increasing interfacial tension. Size filtered data is shown for particles of the median diameter of  $7 \pm 1 \mu\text{m}$ . Boxplots show medians denoted by line, interquartile ranges represented by box, and 10<sup>th</sup> and 90<sup>th</sup> percentiles shown by whiskers. Linear regression in red displays scaling relation compared to the bootstrapped median transit times.  $N > 200$  cells/particles for each sample.

**Transit time scales with elastic modulus.** Our investigation of transit times for gel and oil particles with well-defined mechanical properties also provides deeper insight into the physical underpinnings of cell transit time measurements. We first investigate how elastic modulus affects transit time using our panel of agarose gel particles, which have a similar stiffness as cells such as leukocytes and ovarian cancer cells with  $E = 0.1$  to  $1.0$  kPa (4, 6). As shown in Fig 5A, our size-filtered data across our panel of gel particles from  $E = 3.1$  to  $43$  kPa reveals that stiffer particles have longer transit times than softer particles. At a fixed driving pressure of  $28$  kPa, gel particles with  $1.0\%$  (w/w) agarose and  $E = 8.7$  kPa have a bootstrapped median transit time and confidence interval of  $28 \pm 2.5$  ms. By contrast, stiffer gel particles with  $2.0\%$  (w/w) agarose and  $E = 17$  kPa, have a bootstrapped median transit time and confidence interval of  $40 \pm 5.0$  ms. Across our panel of gel particles, we find that the bootstrapped median transit time scales with elastic modulus, as shown by a simple linear fit (slope =  $0.29$  and  $R^2 = 0.93$ ) (Fig. 4A). These results support previous findings that cells with larger elastic moduli, as extracted from optical stretching experiments, also exhibit longer transit times (25).

**Transit time weakly depends on particle viscosity.** Cells are complex materials that exhibit both elastic and viscous behaviors. We next investigate how the viscosity of droplets regulates transit time by generating oil-in-water emulsions using silicone oils with well-defined viscosities from  $10^{-2}$  to  $10^2$  Pa·s. We hypothesize that droplets with larger viscosities will have longer transit times, as they are comprised of larger molecules, which have longer rearrangement timescales. We select the oils to have a range of viscosities that are comparable to the viscosities of cells, which range from  $10^{-2}$  Pa·s for adherent HeLa and 3T3 cells (31) to  $10^2$  Pa·s for neutrophil cells (25). To prevent coalescence and ensure that droplets remain intact during transit through the microfluidic device, we add 4% (w/w) Tween 20 surfactant. While the viscosities of our panel of oil droplets ranges over five orders of magnitude, we observe transit times increase by only one order of magnitude (Fig. 4B). For example, droplets with the highest viscosity of  $10^2$  Pa·s have a median transit time of  $75 \pm 2.5$  ms; by contrast, droplets with the lowest viscosity of  $10^{-2}$  Pa·s have a median transit time of  $20 \pm 0.0$  ms. Performing a linear fit to the bootstrapped median transit times of our panel of oil droplets reveals a slope of 0.14 with  $R^2 = 0.92$ , suggesting transit time scales with viscosity as well as elastic modulus. However, transit time scales more significantly with elastic modulus on these millisecond timescales (slope = 0.29 and  $R^2 = 0.93$ ).

**Weak dependence of interfacial tension on transit time.** We next investigate the effect of interfacial tension on the transit time of oil droplets. As out-of-plane bending is required for droplets to enter the constriction, we predict that droplets with higher interfacial tensions will have longer transit times. Surface tension is analogous to the cortical tension of cells, which is largely regulated by actin and hinders out-of-plane bending of the plasma membrane (32, 33). To determine the effects of surface tension on transit time, we modify the concentration of Tween 20 surfactant in our silicone oil droplets from 0.005 to 0.1% (w/w); this results in interfacial tensions ranging from 0.7 to  $2.2 \times 10^{-2}$  N/m, as confirmed by the pendant drop technique (34) (S. Fig. 4). Our experimental range of interfacial tensions is set by the critical micelle concentration (CMC) of the surfactant, which is 0.007% (w/w) at room temperature (35). We observe that transit time tends to increase with increasing interfacial tension. For oil

droplets with the highest surface tension of  $2.2 \times 10^{-2}$  N/m, the median transit time is  $25 \pm 3.0$  ms, whereas oil droplets with a surface tension of  $0.7 \times 10^{-2}$  N/m exhibit a median transit time of  $20 \pm 0.0$  ms. Yet even with interfacial tensions that are approximately two orders of magnitude larger than cells, our statistical analyses reveal that there is a marginal effect of interfacial tension on transit time (slope = 0.25 and  $R^2 = 0.91$ ) compared to the effects of elastic modulus and viscosity (Fig. 4C).

Taken together, our micron-scale characterization particles reveal that elastic modulus dominates transit time when cells/particles undergo 40% strain over 0.01 to 1 second, whereas viscosity and interfacial tension have a weaker effect on these time and length scales.

**Transit time depends on both particle stiffness and driving pressure.** To be useful for biological and clinical applications, cell mechanotyping should have both dynamic range and sensitivity for detecting small and large differences in cell mechanical properties. To further develop a comprehensive framework for transit time experiments, we next investigate how  $P_{driving}$  determines the range of mechanotypes that can effectively be measured. As transit time exhibits the strongest dependence on elastic modulus, we map transit times across our panel of gel particles and generate a phase diagram that illustrates the dynamic range for particles.

Determining the range of  $P_{driving}$  that enables transit events for a range of particles with different elastic moduli is an optimization problem that involves both measurement throughput and sensitivity. To achieve rapid measurements, higher  $P_{driving}$ , and thus flow rates, are required. However, a single cell must be tracked for at least two frames to capture its entry and exit as well as its initial size (S. Fig. 5); this can be achieved by acquiring images with high frame rates and fast exposure times. Using our CMOS fast camera, a minimum exposure time of 0.2 ms is required to reduce object blurring and delineate the location and size of a single cell (S. Fig. 6); this enables us to achieve frame rates of up to 5000 frames per second. While higher image acquisition rates could be achieved with a faster camera, increased  $P_{driving}$  could ultimately result in strain of PDMS channels, since  $E_{PDMS} \sim 10$  MPa. The lower pressure bound must be exceeded for a transit event to occur and is set by the threshold pressure,  $P_T$ . To quantify the

lower pressure bound for particles of a given elastic modulus and size, we analyze the transit of particles with differing elastic moduli over a range of applied pressures.

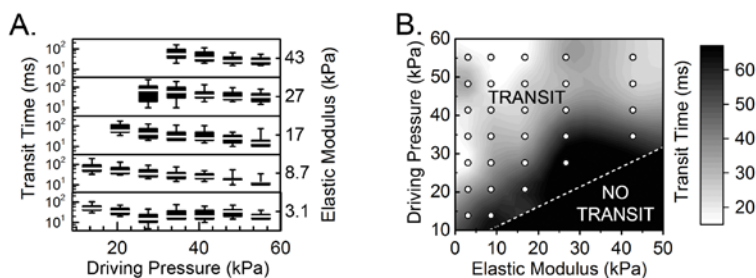


**Fig. 5 Effects of driving pressure and particle elastic modulus on transit time.** (A) Boxplots show transit time for agarose gel particles with well-defined elastic moduli over a range of driving pressures. Median is denoted by line, interquartile range is represented by box, and 10<sup>th</sup> and 90<sup>th</sup> percentiles are shown by whiskers. The absence of a boxplot at a given pressure reflects that no transit events occur, as  $P_T < P_{\text{driving}}$ . (B) Density map of transit time values as a function of driving pressure and gel particle elastic modulus. Dots represent the experimental conditions where transit time data is acquired. Dotted line represents the estimated boundary between transit and no transit regions based on measured  $P_T$  values.  $N > 200$  particles for each sample.

We observe that stiffer particles require larger pressures to transit through the constrictions (Fig. 5). For example, we do not observe any transit events on the experimental timescale for the stiffest particles of  $E = 43$  kPa at  $P_{\text{driving}} \leq 28$  kPa. By contrast, a significant proportion of softer particles with  $E = 3.1$  kPa transit through the constrictions at  $P_{\text{driving}} = 28$  kPa. These results highlight how  $P_{\text{driving}}$  needs to be tuned to optimize the dynamic range for a set of samples with given mechanotypes. For example, to measure transit times for the softest and stiffest gel particles ( $E = 3.1$  and 43 kPa),  $P_{\text{driving}}$  should be between 34 to 55 kPa: below this pressure, stiffer particles do not transit; yet with higher pressures, softer particles transit too quickly to resolve their entry into and exit from the constriction region. Taken together, our mapping of transit times across driving pressures and particle elastic modulus results in a phase diagram, which illustrates regions where transit and no transit occur for particles of varying stiffness as a function of  $P_{\text{driving}}$ .

**Additional sources of transit time variability.** In contrast to our gel and oil particles that have relatively uniform structure and composition, cells are spatially heterogeneous materials. For example, the nucleus can occupy a significant volume within the cell and can be up to five times stiffer than the surrounding cytoplasm (36, 37). Our previous study demonstrates how the nucleus can rate-limit the deformation of cells through micron-scale gaps (8). The nucleus can also vary in size and morphology across a population of single cells (38). Additional geometric differences among cells could contribute to transit time variability, such as heterogeneity in the distribution of actin due to polarization and/or the position of the nucleus in a transiting cell. Moreover, cells at different stages in the cell cycle have markedly different subcellular architecture and mechanotype (39); this likely also contributes to the variability in transit times we observe in populations of cells.

**Deformation time and length scales.** The deformation response of viscoelastic materials ranging from hydrogels to cells is sensitive to the time and length scales of the applied stress. Our results using calibration particles demonstrate that transit time measurements on millisecond timescales are dominated by elastic modulus. These results are consistent with our rheology data for agarose slabs, which determine the relative elastic and viscous contributions to deformations of agarose gels. By measuring the storage ( $G'$ ) and loss ( $G''$ ) moduli across a frequency range of 0.01 to 1 Hz, we observe that  $G'$  is ~350% greater than  $G''$  and remains relatively constant over this linear regime (S. Fig. 3).

Reconstituted actin (40) and intermediate filament (41) networks also exhibit a storage modulus,  $G'$ , that is typically 10 to 100 times larger than the loss modulus,  $G''$ , when probed at strain rates of 0.1 to 10 Hz. In addition, the deformation behavior of cells on similar 0.01 to 1 second timescales is largely determined by their elastic properties (42–44). However, at higher strain rates above 1000 Hz,  $G''$  dominates the deformation behavior, reflecting increased viscous contributions as the deformation timescale approaches the timescale for intracellular macromolecules and water molecules to rearrange (45). For higher throughput fluid-based deformability measurements, which occur on microsecond timescales (10), cell deformation behavior may thus depend more strongly on cell viscous properties.

The mechanical response of cells also depends on the length scale of deformation as cells are spatially heterogeneous structures. For example, the cortical region of the cell can determine the mechanical response to nanometer-scale indentations by AFM and micron-scale, out-of-plane bending induced by micropipette aspiration (22, 46). While out-of-plane bending is a requisite for cell entry into the constricted channel, cell transit events require much larger deformations of the whole cell, which involve shear and compression; these considerations support our findings that transit time exhibits the strongest dependence on elastic modulus. An elastic sphere or shell model can also recapitulate the deformations of cells and agarose beads that are induced by shear stresses during flow through microfluidic channels on millisecond timescales (47). Our results also highlight how viscosity plays a role in transit time measurements. Indeed, viscoelastic models, such as power law rheology, can successfully predict the transit behavior of cells through microfluidic constrictions (18). Such physical models, together with particles that have tunable elastic and viscous moduli, should enable more detailed quantitative measurements of cell mechanical properties. Particles with well-defined mechanical properties also provide much-needed calibration standards in cell mechanotyping; quantitative comparisons of cell deformability across different techniques and laboratories is critical for more advanced clinical applications of mechanotyping.

## **Conclusion**

In this study, we identify major contributors to the cell-to-cell variability of transit times with the goal of enabling precise classification of cell populations. We demonstrate how more robust transit time measurements can be achieved by reducing variability with post acquisition analysis and size binning. We also determine the extent to which the inherent heterogeneity in cell physical properties contributes to the width of transit time distributions. Our results should enable broader application of transit time measurements for rapid, single-cell mechanotyping in basic research to clinical settings.

## Methods

**Device fabrication.** Devices are fabricated using standard photolithography methods (48). The photoresist, SU-8 3005 (MicroChem, Westborough, MA, USA), is patterned onto a silicon wafer using standard photolithography techniques. We confirm SU-8 thickness using a Dektak 150 Surface Profilometer (Veeco, Fullerton, CA). Polydimethylsiloxane (Sylgard 184 silicone elastomer, Dow Corning, Midland, MI, USA) is mixed with crosslinker at a 1:10 w/w ratio, then poured onto the mold and cured at 65°C for 2 hours. The patterned PDMS is subsequently removed from the silicon mold and bonded to #1.5-thickness coverslips after exposure to corona discharge plasma for 1 minute and baking at 80°C for 20 minutes.

**Cell culture.** HL-60 cells are cultured in RPMI-1640 media with L-Glutamine (Life Technologies, Carlsbad, CA, USA), 10% fetal bovine serum, and 1% Pen/Strep (Gemini BioProducts, West Sacramento, CA, USA). Cell viability is determined before and after transit experiments using trypan blue dye and a TC20 Automated Cell Counter (Bio-Rad, Hercules, CA, USA).

**Soft particle fabrication.** To make silicone oil droplets, we generate oil-in-water emulsions in deionized water with Tween 20 surfactant (Sigma-Aldrich, St. Louis, MO, USA). Deionized water with silicone oil (1:5 v/v) and varying concentrations of Tween 20 (5 to 100 mg/mL) are vortexed for 1 minute. The emulsion is then centrifuged at  $157 \times g$  for 3 minutes to remove air bubbles and filtered through a 35  $\mu\text{m}$  mesh cap (BD Biosciences, Franklin Lakes, NJ, USA). For oil droplet experiments, we maintain a concentration of 4% (w/w) Tween 20, which is significantly greater than the critical micelle concentration (CMC) of 0.01% (w/w), so that the droplet surface is saturated and surface tension is effectively minimized.

To fabricate agarose gel particles with defined elastic moduli, we make water-in-oil emulsions with agarose dissolved in the aqueous phase. The desired (w/w) percentage of ultra-low gelling temperature agarose (Sigma-Aldrich, St. Louis, MO, USA) is added to deionized water and heated in the microwave for about 30 seconds until boiling. Mineral oil with 1% w/w Span 80 and agarose solution (1: 5 v/v) are

vortexed on high for 1 minute, filtered through a 35  $\mu\text{m}$  filter (BD Biosciences, Franklin Lakes, NJ, USA), and immediately placed on ice for 1 hour to promote gelation; thereafter, the suspension is filtered a second time through a 35  $\mu\text{m}$  filter. The gel particles are removed from the oil phase by adding 5 mL of deionized water and centrifuging at  $157 \times g$  for 10 minutes. To isolate the aqueous suspension of gel particles, the oil phase is removed from the top of the solution by pipetting.

**Rheology measurements.** To confirm the elastic moduli of our agarose gel particles, we measure the linear storage ( $G'$ ) and loss ( $G''$ ) moduli of agarose slabs using a controlled strain shear rheometer (RFS-II, 25 mm diameter parallel plate geometry, Rheometric Scientific, Inc., Piscataway, NJ, USA). The elastic properties of these agarose slabs are similar to those found for micron-scale agarose particles (30). Agarose solutions of varying concentrations at 20°C are loaded into the rheometer's gap set to 1 mm, gelled to 10°C for one hour, and then brought back to 20°C over 30 minutes prior to measurement acquisition. A vapor trap inhibits water evaporation during gelation and measurement acquisition. To reduce slipping between the gel and the rheometer's plates, sandpaper is adhered to these plates prior to gel casting. We perform a frequency sweep from 0.1 to 10 rad/s at 1.0% strain, in the linear response limit (S. Fig. 3); for each agarose concentration, this measurement is repeated three times (including loading and gelling) to obtain average values and to estimate run-to-run uncertainties. To determine Young's moduli from the measured  $G'$  values, we use a Poisson ratio of 0.5 (49). Here, we estimate the elastic modulus of our agarose gels as the Young's modulus evaluated at 1.0% strain and 1 rad/s.

**Microfluidic experiments.** For cell deformation experiments, 0.1% (w/w) Pluronic F-127 (Sigma-Aldrich, St. Louis, MO, USA) is added to the cell suspension to minimize cell-surface interactions (S. Video 1). We drive suspensions of cells, gels, and droplets through the microfluidic device by applying air pressure to the sample. To maintain consistent fluidic resistance, we ensure the same length of tubing is used across all experiments. For experiments with cells and gel particles, PDMS devices are used 48 hours after plasma treatment and bonding. For experiments with oil droplets, PDMS channel hydrophilicity is maintained after plasma treatment by filling channels with deionized water; transit time



is measured within 1 hour after plasma treatment. Transit videos are captured at 200 frames/s with a high-speed camera (MiroEx4, Vision Research, Wayne, NJ, USA) mounted on an inverted light microscope (Zeiss Observer, Zeiss, Oberkochen, Germany) with a 20×/0.40 objective (LD Achromat, Zeiss, Oberkochen, Germany).

**Transit time analysis.** Videos from microfluidic experiments are processed using a custom code in MATLAB (Mathworks, Torrance, CA, USA) (S. Fig. 5). In brief, the code detects particles, tracks their location, records their size, and determines the time for the leading edge of particles to transit through the constriction region (Fig. 1C). Expanding on previously described tracking algorithms (27), we apply here a rigorous protocol for cell detection and tracking: to determine the spatial bounds of the device constriction region, we perform an automated fit of a mask to remove regions outside of the microfluidic constrictions; to locate individual particles, we apply a set of filters, which include thresholding, dilation, erosion, median smoothing, and closing; to determine the start and end of transit, we measure the time required for the front of a particle to enter and exit the constriction region. Statistical analysis is performed using OriginPro software (OriginLab Corporation, Northampton, MA, USA). For all samples, we exclude particles with diameters smaller than 5  $\mu\text{m}$  to ensure all measured particles are sufficiently deformed as they flow through the constrictions. After these filtering procedures, we obtain  $90 \pm 30$  cell transit measurements per minute. To determine how transit time depends on mechanical properties, we apply Pearson's chi squared test on the log transforms of the median data and mechanical properties. To distinguish statistically significant differences across cell treatment populations, we employ the Mann-Whitney U test, which enables us to compare the non-normal distributions of transit times.

## Bibliography

1. Henry, T.K., D.R. Gossett, Y.S. Moon, M. Masaeli, M. Sohsman, Y. Ying, K. Mislick, R.P. Adams, J. Rao, and D. Di Carlo. 2013. Quantitative diagnosis of malignant pleural effusions by single-cell mechanophenotyping. *Sci. Transl. Med.* 5: 212ra163--212ra163.
2. Liu, X., Y. Wang, and Y. Sun. 2007. Real-time high-accuracy micropipette aspiration for characterizing mechanical properties of biological cells. In: *Robotics and Automation, 2007 IEEE International Conference on*. . pp. 1930–1935.
3. Cross, S.E., Y.-S. Jin, J. Rao, and J.K. Gimzewski. 2007. Nanomechanical analysis of cells from cancer patients. *Nat. Nanotechnol.* 2: 780–3.
4. Xu, W., R. Mezencev, B. Kim, L. Wang, J. McDonald, and T. Sulchek. 2012. Cell stiffness is a biomarker of the metastatic potential of ovarian cancer cells. *PLoS One.* 7: e46609.
5. Guck, J., S. Schinkinger, B. Lincoln, F. Wottawah, S. Ebert, M. Romeyke, D. Lenz, H.M. Erickson, R. Ananthakrishnan, D. Mitchell, others, J. Käs, S. Ulvick, and C. Bilby. 2005. Optical deformability as an inherent cell marker for testing malignant transformation and metastatic competence. *Biophys. J.* 88: 3689–98.
6. Rosenbluth, M.J., W.A. Lam, and D.A. Fletcher. 2008. Analyzing cell mechanics in hematologic diseases with microfluidic biophysical flow cytometry. *Lab Chip.* 8: 1062–1070.
7. Hou, H.W., Q.S. Li, G.Y.H. Lee, a. P. Kumar, C.N. Ong, and C.T. Lim. 2009. Deformability study of breast cancer cells using microfluidics. *Biomed. Microdevices.* 11: 557–564.
8. Rowat, A.C., D.E. Jaalouk, M. Zwerger, W.L. Ung, I. a Eydelnant, D.E. Olins, A.L. Olins, H. Herrmann, D. a Weitz, and J. Lammerding. 2013. Nuclear envelope composition determines the ability of neutrophil-type cells to passage through micron-scale constrictions. *J. Biol. Chem.* 288: 8610–8.

9. Byun, S., S. Son, D. Amodei, N. Cermak, J. Shaw, J. Ho, and V.C. Hecht. 2013. Characterizing deformability and surface friction of cancer cells. .
10. Gossett, D.R., H.T.K. Tse, S. a Lee, Y. Ying, A.G. Lindgren, O.O. Yang, J. Rao, A.T. Clark, D. Di Carlo, and T.K. Henry. 2012. Hydrodynamic stretching of single cells for large population mechanical phenotyping. *Proc. Natl. Acad. Sci. U. S. A.* 109: 7630–5.
11. Otto, O., P. Rosendahl, A. Mietke, S. Golfier, C. Herold, D. Klaue, S. Girardo, S. Pagliara, A. Ekpenyong, A. Jacobi, M. Wobus, N. Töpfner, U.F. Keyser, J. Mansfeld, E. Fischer-Friedrich, and J. Guck. 2015. Real-time deformability cytometry: on-the-fly cell mechanical phenotyping. *Nat. Methods.* 12.
12. Faigle, C., F. Lautenschläger, G. Whyte, P. Homewood, E. Martín-Badosa, and J. Guck. 2015. A monolithic glass chip for active single-cell sorting based on mechanical phenotyping. *Lab Chip.* 15: 1267–1275.
13. Yang, T., P. Paiè, G. Nava, F. Bragheri, R.M. Vazquez, P. Minzioni, M. Vegliione, M. Di Tano, C. Mondello, R. Osellame, and others. 2015. An integrated optofluidic device for single-cell sorting driven by mechanical properties. *Lab Chip.* 15: 1262–1266.
14. Vazquez, R.M., G. Nava, M. Vegliione, T. Yang, F. Bragheri, P. Minzioni, E. Bianchi, M. Di Tano, I. Chiodi, R. Osellame, and others. 2015. An optofluidic constriction chip for monitoring metastatic potential and drug response of cancer cells. *Integr. Biol.* 7: 477–484.
15. Chen, J., Y. Zheng, Q. Tan, E. Shojaei-Baghini, Y.L. Zhang, J. Li, P. Prasad, L. You, X.Y. Wu, and Y. Sun. 2011. Classification of cell types using a microfluidic device for mechanical and electrical measurement on single cells. *Lab Chip.* 11: 3174–3181.
16. Zhao, Y., X.T. Zhao, D.Y. Chen, Y.N. Luo, M. Jiang, C. Wei, R. Long, W.T. Yue, J.B. Wang, and J. Chen. 2014. Tumor cell characterization and classification based on cellular specific membrane capacitance and cytoplasm conductivity. *Biosens. Bioelectron.* 57: 245–253.

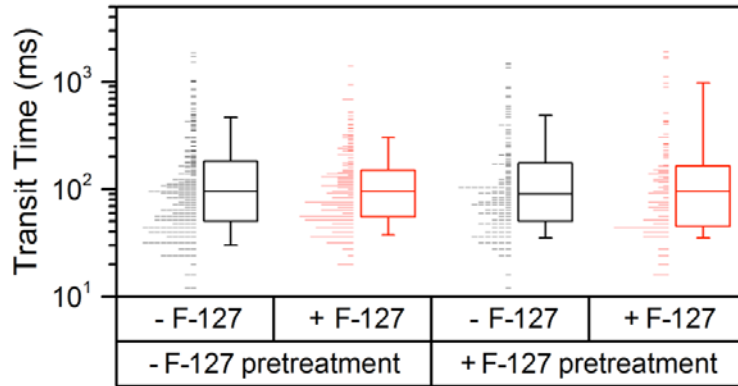
17. Jia, Z., L. Barbier, H. Stuart, M. Amraei, S. Pelech, J.W. Dennis, P. Metalnikov, P. O'Donnell, and I.R. Nabi. 2005. Tumor cell pseudopodial protrusions. Localized signaling domains coordinating cytoskeleton remodeling, cell adhesion, glycolysis, RNA translocation, and protein translation. *J. Biol. Chem.* 280: 30564–30573.
18. Lange, J.R., J. Steinwachs, T. Kolb, L.A. Lautscham, I. Harder, G. Whyte, and B. Fabry. 2015. Microconstriction Arrays for High-Throughput Quantitative Measurements of Cell Mechanical Properties. *Biophys. J.* 109: 26–34.
19. Cai, P., Y. Mizutani, M. Tsuchiya, J.M. Maloney, B. Fabry, K.J. Van Vliet, and T. Okajima. 2013. Quantifying cell-to-cell variation in power-law rheology. *Biophys. J.* 105: 1093–1102.
20. Zhou, E.H., S.T. Quek, and C.T. Lim. 2010. Power-law rheology analysis of cells undergoing micropipette aspiration. *Biomech Model Mechanobiol.* 9: 563–572.
21. Tsai, M.A., R.S. Frank, and R.E. Waugh. 1993. Passive mechanical behavior of human neutrophils: power-law fluid. *Biophys. J.* 65: 2078–2088.
22. Evans, E., and A. Yeung. 1989. Apparent viscosity and cortical tension of blood granulocytes determined by micropipet aspiration. *Biophys. J.* 56: 151.
23. Needham, D., and R.M. Hochmuth. 1990. Rapid flow of passive neutrophils into a 4 microns pipet and measurement of cytoplasmic viscosity. *J. Biomech. Eng.* 112: 269–276.
24. Maloney, J.M., D. Nikova, F. Lautenschläger, E. Clarke, R. Langer, J. Guck, and K.J. Van Vliet. 2010. Mesenchymal stem cell mechanics from the attached to the suspended state. *Biophys. J.* 99: 2479–2487.
25. Ekpenyong, A.E., G. Whyte, K. Chalut, S. Pagliara, F. Lautenschläger, C. Fiddler, S. Paschke, U.F. Keyser, E.R. Chilvers, and J. Guck. 2012. Viscoelastic Properties of Differentiating Blood Cells Are Fate- and Function-Dependent. *PLoS One.* 7.

26. Morra, M., E. Occhiello, R. Marola, F. Garbassi, P. Humphrey, and D. Johnson. 1990. On the aging of oxygen plasma-treated polydimethylsiloxane surfaces. *J. Colloid Interface Sci.* 137: 11–24.
27. Hoelzle, D.J., B.A. Varghese, C.K. Chan, and A.C. Rowat. 2014. A Microfluidic Technique to Probe Cell Deformability. *JoVE.* 91: e51474–e51474.
28. Gabriele, S., A.M. Benoliel, P. Bongrand, and O. Théodoly. 2009. Microfluidic investigation reveals distinct roles for actin cytoskeleton and myosin II activity in capillary leukocyte trafficking. *Biophys. J.* 96: 4308–4318.
29. Eddington, D.T., W.C. Crone, and D.J. Beebe. 2003. Development of process protocols to fine tune polydimethylsiloxane material properties. In: *7th International Conference on Miniaturized Chemical and Biochemical Analysis Systems.* . pp. 1089–1092.
30. Kumachev, A., E. Tumarkin, G.C. Walker, and E. Kumacheva. 2013. Characterization of the mechanical properties of microgels acting as cellular microenvironments. *Soft Matter.* 9: 2959.
31. Kalwarczyk, T., N. Ziębacz, A. Bielejewska, E. Zaboklicka, K. Koynov, J. Szymański, A. Wilk, A. Patkowski, J. Gapiński, H.J. Butt, and R. Hołyst. 2011. Comparative analysis of viscosity of complex liquids and cytoplasm of mammalian cells at the nanoscale. *Nano Lett.* 11: 2157–2163.
32. Rowat, A.C., J. Lammerding, and J.H. Ipsen. 2006. Mechanical properties of the cell nucleus and the effect of emerin deficiency. *Biophys. J.* 91: 4649–4664.
33. Henriksen, J.R., and J.H. Ipsen. 2004. Measurement of membrane elasticity by micro-pipette aspiration. *Eur. Phys. J. E.* 14: 149–167.
34. Hanse, F.K., and G. Rodsrud. 1991. Surface Tension by Pendant Drop. *J. Colloid Interface Sci.* 141: 1–9.
35. Patist, A., S.S. Bhagwat, K.W. Penfield, P. Aikens, and D.O. Shah. 2000. On the measurement of

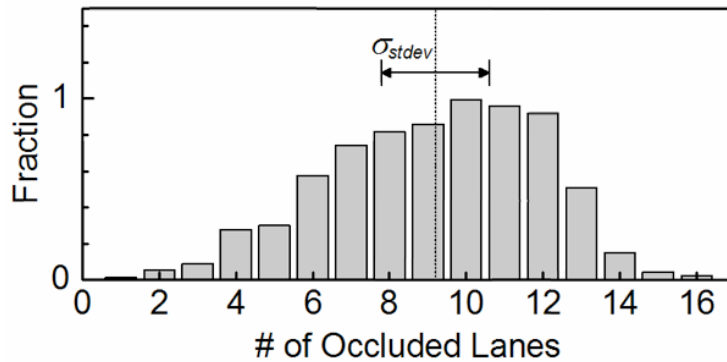
- critical micelle concentrations of pure and technical-grade nonionic surfactants. *J. Surfactants Deterg.* 3: 53–58.
36. Rowat, A.C., J. Lammerding, H. Herrmann, and U. Aebi. 2008. Towards an integrated understanding of the structure and mechanics of the cell nucleus. *Bioessays.* 30: 226–236.
  37. Guilak, F., J.R. Tedrow, and R. Burgkart. 2000. Viscoelastic properties of the cell nucleus. *Biochem. Biophys. Res. Commun.* 269: 781–786.
  38. Webster, M., K.L. Witkin, and O. Cohen-Fix. 2009. Sizing up the nucleus: nuclear shape, size and nuclear-envelope assembly. *J. Cell Sci.* 122: 1477–86.
  39. Tsai, M. a, R.E. Waugh, and P.C. Keng. 1996. Cell cycle-dependence of HL-60 cell deformability. *Biophys. J.* 70: 2023–2029.
  40. Lieleg, O., K.M. Schmoller, M. Claessens, and A.R. Bausch. 2009. Cytoskeletal polymer networks: viscoelastic properties are determined by the microscopic interaction potential of cross-links. *Biophys. J.* 96: 4725–4732.
  41. Lin, Y.-C., N.Y. Yao, C.P. Broedersz, H. Herrmann, F.C. MacKintosh, and D.A. Weitz. 2010. Origins of elasticity in intermediate filament networks. *Phys. Rev. Lett.* 104: 58101.
  42. Deng, L., X. Trepate, J.P. Butler, E. Millet, K.G. Morgan, D.A. Weitz, and J.J. Fredberg. 2006. Fast and slow dynamics of the cytoskeleton. *Nat. Mater.* 5: 636–640.
  43. Hoffman, B.D., G. Massiera, K.M. Van Citters, and J.C. Crocker. 2006. The consensus mechanics of cultured mammalian cells. *Proc. Natl. Acad. Sci.* 103: 10259–10264.
  44. Kasza, K.E., A.C. Rowat, J. Liu, T.E. Angelini, C.P. Brangwynne, G.H. Koenderink, and D.A. Weitz. 2007. The cell as a material. *Curr. Opin. Cell Biol.* 19: 101–107.
  45. Fabry, B., G.N. Maksym, J.P. Butler, M. Glogauer, D. Navajas, and J.J. Fredberg. 2001. Scaling the microrheology of living cells. *Phys. Rev. Lett.* 87: 148102.

46. Rotsch, C., and M. Radmacher. 2000. Drug-induced changes of cytoskeletal structure and mechanics in fibroblasts: an atomic force microscopy study. *Biophys. J.* 78: 520–535.
47. Mietke, A., O. Otto, S. Girardo, P. Rosendahl, A. Taubenberger, S. Golfier, E. Ulbricht, S. Aland, J. Guck, and E. Fischer-Friedrich. 2015. Extracting Cell Stiffness from Real-Time Deformability Cytometry: Theory and Experiment. *Biophys. J.* 109: 2023–2036.
48. Duffy, D.C., J.C. McDonald, O.J. Schueller, and G.M. Whitesides. 1998. Rapid Prototyping of Microfluidic Systems in Poly(dimethylsiloxane). *Anal. Chem.* 70: 4974–84.
49. Normand, V., D.L. Lootens, E. Amici, K.P. Plucknett, and P. Aymard. 2000. New insight into agarose gel mechanical properties. *Biomacromolecules.* 1: 730–738.

## Supplemental Figures

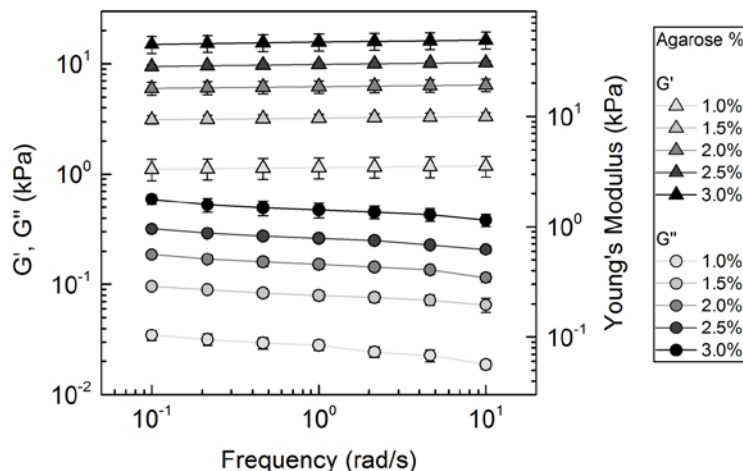


**S. Fig. 1. Effect of Pluronic F-127 on HL-60 cell transit time.** Devices +F-127 pretreatment: microfluidic devices are pretreated with 0.1% (w/w) Pluronic F-127 in RPMI medium for 1 hour prior to flowing cells through the device. +F-127: 0.1% (w/w) Pluronic F-127 is added to the cell suspension as denoted by the red boxplots. Boxplots show medians denoted by the line, interquartile ranges represented by boxes, and 10<sup>th</sup> and 90<sup>th</sup> percentiles shown by whiskers.  $N > 120$  cells for each sample.

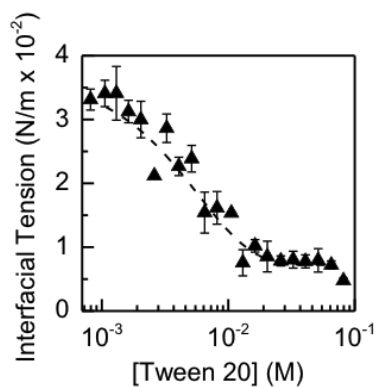


**S. Fig. 2. Simultaneous lane occlusions during transit of WT HL-60 cells.** Histogram of the number of occluded lanes during the transit of each cell. Transit time measurements are performed under standard conditions for HL-60 cells with driving pressure 28 kPa, channel width  $5.3 \times 5.2 \mu\text{m}^2$ . Dotted line represents the mean, while the black arrow represents the standard deviation.

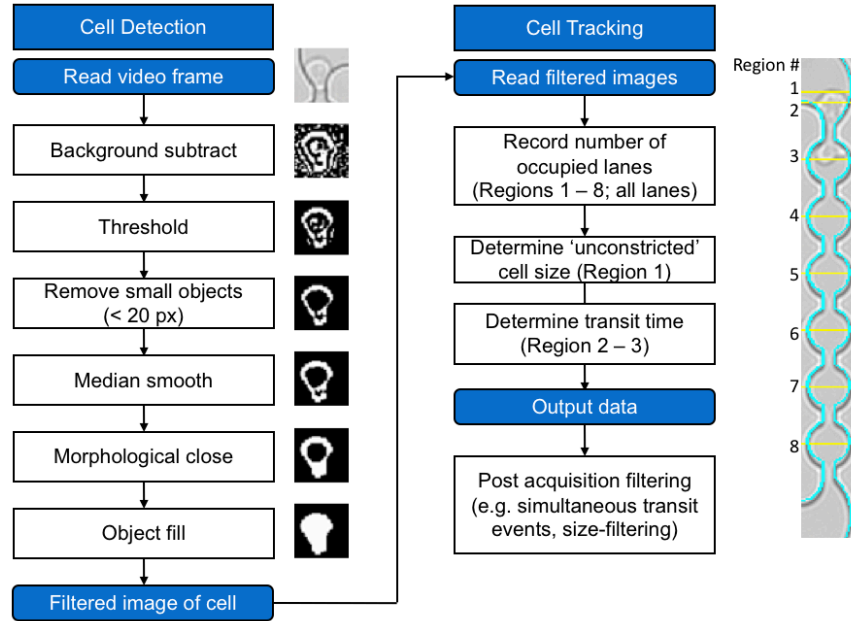




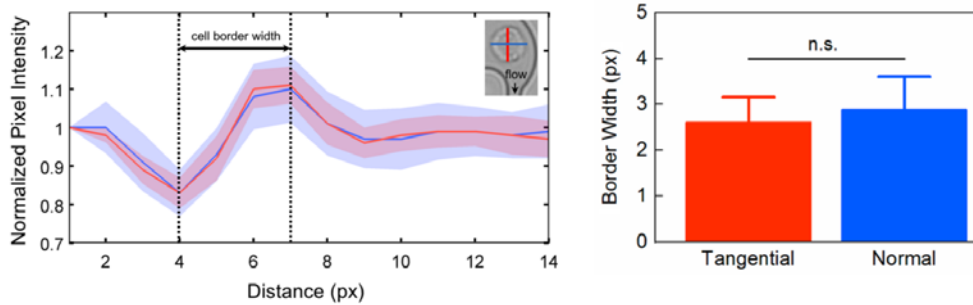
**S. Fig. 3. Mechanical properties of agarose gel slabs.** Rheology measurements of the elastic storage ( $G'$ ) and viscous loss ( $G''$ ) moduli (left axis) of low gel-temperature agarose gels as a function of agarose density (w/w%). To calculate the Young's modulus (right axis, triangles), we use a Poisson ratio of 0.5. Error bars represent  $\pm 1$  standard deviation for  $N = 3$  replicates at each agarose density.



**S. Fig. 4. Interfacial tension as a function of Tween 20 concentration.** Interfacial tension measured by the pendant drop technique. Data points represent the average interfacial tension obtained from independent experiments ( $N = 3$ ). Error bars represent the standard deviation.



**S. Fig. 5. Flowchart illustrating the algorithm used for image analysis.** Images show a representative HL-60 cell flowing through a constriction with a  $5.3 \mu\text{m}$  height  $\times$   $5.2 \mu\text{m}$  width.



**S. Fig. 6. Quantification of object blurring during cell transit.** Image blurring is assessed by measuring the width of the cell border in directions both tangential and normal to flow. Bar plots represent the average border width. Error bars denote the standard deviation ( $N = 35$ ).

## Supplemental Video

### **S.Video. 1. Pluronic F-127 can minimize cell-wall adhesion during transit through a PDMS**

**microfluidic device.** Pancreatic ductal epithelial (HPDE) cells transiting through  $9 \times 10$  constrictions (A) without Pluronic F-127, and (B) with 0.1% (w/w) Pluronic F-127 in the cell media. While we qualitatively observe a difference in the transit behavior of these pancreatic ductal epithelial (HPDE) cells, other cell types, such as HL-60 cells, show no significant difference in transit times with and without Pluronic F-127 surfactant (S. Fig. 1). Videos are acquired at 2000 fps. Videos are slowed down by 10x.

## CHAPTER 2

### *Quantitative Deformability Cytometry (q-DC): rapid, calibrated measurements of single cell viscoelastic properties*

#### **Abstract**

Advances in methods that determine cell mechanical phenotype, or mechanotype, have demonstrated the utility of biophysical markers in clinical and research applications, ranging from cancer diagnosis to stem cell enrichment. Here, we introduce quantitative deformability cytometry (q-DC), a method for rapid, calibrated, single cell mechanotyping. We track changes in cell shape as cells deform into microfluidic constrictions, and calibrate the mechanical stresses using gel beads. We observe the time-dependent strain follows power law rheology, enabling single cell measurements of apparent elastic modulus,  $E_a$ , and power law exponent,  $\beta$ . To validate our method, we mechanotype human promyelocytic leukemia (HL-60) cells, and thereby confirm q-DC measurements of  $E_a = 0.53 \pm 0.04$  kPa. We also demonstrate q-DC is sensitive to pharmacological perturbations of the cytoskeleton, as well as differences in the mechanotype of human breast cancer cell lines ( $E_a = 2.1 \pm 0.1$  and  $0.80 \pm 0.19$  kPa for MCF-7 and MDA-MB-231 cells). To establish an operational framework for q-DC, we investigate the effects of applied stress and cell-to-pore-size ratio on mechanotype measurements. We show that  $E_a$  increases with applied stress, which is consistent with stress stiffening behavior of cells. We also find that  $E_a$  increases for larger cell-to-pore size ratios, even when the same applied stress is maintained; these results indicate strain stiffening and/or the dependence of mechanotype on deformation depth. Taken together, the calibrated measurements enabled by q-DC should advance applications of cell mechanotype in basic research and clinical settings.

## Introduction

Eukaryotic cells are complex, viscoelastic materials that undergo changes in their mechanical phenotype, or mechanotype, during many physiological and disease processes. For example, pluripotent stem cells become more resistant to deformation as they differentiate (1–4), and the deformability of cancer cells is associated with their invasive potential (5–7). Thus, cell mechanotype is emerging as a label-free biomarker for altered cell and pathological states. In addition, mechanotyping methods have demonstrated the potential for enhancing cancer diagnoses (8) and enriching stem cell populations (9). Rapid, calibrated measurements of cell viscoelastic properties could enable robust longitudinal and cross-study comparisons, and thus further advance the utility of cell mechanotyping.

Standardized measurements of cell mechanical properties, such as elastic modulus,  $E$ , compliance,  $J$ , or viscosity,  $\eta$ , are acquired by probing cells with well-defined stresses and measuring the resultant deformations. Such measurements can be achieved using atomic force microscopy (AFM) (5, 10, 11), micropipette aspiration (12–14), optical stretching (2, 15–17), and microplate compression (18, 19), and can reveal physical principles that underlie cell mechanical properties, including viscoelastic and stress stiffening behaviors (20–22). Identifying such universal characteristics of cells can deepen our understanding of the role of mechanotype in physiology and disease. Moreover, standardized measurements enable accurate longitudinal and cross-study comparisons (11). However, measurements of mechanical moduli, for example, those obtained using AFM or micropipette aspiration, are typically acquired at rates of <1 cell/min. Higher throughputs are critical for measuring large numbers of single cells in clinical samples (23, 24) and elucidating the origins of phenotypic variability within a population.

Fluid-based deformability cytometry (DC) enables rapid single cell mechanotyping at faster rates of  $10^2$  –  $10^6$  cells per minute. Such DC methods demonstrate the potential of mechanotype for varying applications such as classifying cells at different stages of the cell cycle by their distinct mechanical properties (23) and enhancing the accuracy of clinical diagnoses by mechanotyping pleural effusions (8). In one DC method,

the hydrodynamic forces of inertial flow deform cells on the microsecond timescale (25). While this method facilitates the analysis of large populations, the external stresses on single cells are challenging to model and calculate. In the real-time DC (rt-DC) method, the shear stresses of fluid flow induce cell deformations; as these shape changes are well described by a continuum elastic model (26),  $E$  can be measured for single cells on millisecond to microsecond timescales (23). With the transit DC method, cells are driven to deform and transit through microfluidic constrictions on millisecond timescales (16, 27–34). The time required for cells to transit through microfluidic constrictions can depend on cell size, mechanical properties, and surface properties, but the initial deformation into microfluidic constrictions is dominated by cell deformability (32, 33, 35); cells and particles that have a higher  $E$  exhibit longer deformation timescales (16, 35, 36). Such transit experiments are widely used to mechanotype various cell types from breast cancer cells to neutrophils based on relative deformation timescales (27, 30). The average  $E$  of a population can be determined by driving cells through microfluidic constrictions with a range of pressures and fitting a viscoelastic model to the resultant strain and transit time data for thousands of cells (31, 34). However, single cell analysis is critical for characterizing population heterogeneity (37).

Here we demonstrate rapid, calibrated, mechanical measurements of single cells using quantitative deformability cytometry (q-DC). We drive cells to deform through micron-scale constrictions at rates of thousands of cells per minute by applying a pressure gradient across the microfluidic device (29). To obtain quantitative measurements of cell mechanotype, we track the time-dependent strain of individual cells and calibrate the applied stresses using gel particles with well-defined elastic moduli. Our results show that the deformation response of single cells follows power law rheology (PLR), which enables us to determine an apparent elastic modulus,  $E_a$ , and power law exponent,  $\beta$  or fluidity, for single cells. We validate our q-DC method by measuring  $E_a$  and  $\beta$  for human promyelocytic leukemia (HL-60) cells. We find that  $E_a$  increases with cell strain and applied stress on these time and length scales. We also demonstrate that q-DC is sensitive to changes in HL-60 mechanotype following treatment with cytoskeletal-perturbing drugs. Differences in the mechanotype between human breast cancer cell lines, MCF-7 and MDA-MB-231 cells,

can also be detected. Taken together, the q-DC platform enables rapid, calibrated mechanotyping, which should deepen our understanding of cells as materials.

## **Materials and Methods**

**Cell culture.** Cells are cultured at 37°C with 5% CO<sub>2</sub>. Cell media and L-Glutamine are from Life Technologies, Carlsbad, CA, USA; fetal bovine serum (FBS) and penicillin-streptomycin are from Gemini BioProducts, West Sacramento, CA, USA. Human promyelocytic leukemia (HL-60) cells are cultured in RPMI-1640 medium with L-Glutamine, 10% FBS, and 1% penicillin-streptomycin. To perturb the cytoskeleton, cells are treated for 1 hr with: 2 μM cytochalasin D (Santa Cruz Biotechnology, Santa Cruz, CA, USA), 100 μM blebbistatin (Santa Cruz Biotechnology, Santa Cruz, CA, USA), and 100 nM jasplakinolide (Life Technologies, Carlsbad, CA, USA). Cell viability is determined using trypan blue staining (S. Table 1). Human breast cancer cell lines, MCF-7 and MDA-MB-231, are cultured in high glucose, L-glutamine, sodium pyruvate Dulbecco's Modified Eagle Medium (DMEM) medium with 10% fetal bovine serum and 1% penicillin-streptomycin. The human promyelocytic leukemia (HL-60) cells and human breast cancer cell lines (MCF-7 and MDA-MB-231) are from the American Type Culture Collection (ATCC). The identity of each cell line is confirmed using multiplex short tandem repeat (STR) profiling (Laragen Inc., Culver City, CA, USA).

**Fabrication of calibration particles.** Silicone oil droplets and gel particles are fabricated using methods previously described (35). In brief, silicone oil droplets are formed by generating oil-in-water emulsions where the dynamic viscosity of the silicone oil varies from 10<sup>-2</sup> to 10<sup>1</sup> Pa·s (Sigma-Aldrich, St. Louis, MO, USA). Deionized (DI) water with silicone oil (1:5 v/v) and 4% (w/v) Tween 20 surfactant (Sigma-Aldrich, St. Louis, MO, USA) are vortexed for 1 minute. The concentration of Tween 20 is significantly larger than the critical micelle concentration of 0.01% (w/v), such that the droplet surface is saturated with surfactant and the droplets are effectively stabilized while transiting through the microfluidic device. Prior to transit experiments, the emulsion is centrifuged at 157 x g for 3 minutes to remove air bubbles and filtered through

a 35  $\mu\text{m}$  mesh filter (BD Biosciences, Franklin Lakes, NJ, USA) to create a size distribution of droplets that is similar to cells (35). To further ensure droplet stability during transit through the microfluidic devices, experiments are conducted within one hour after plasma treatment to maintain hydrophilic surface properties. Channels are also filled with DI water 5 min after plasma treatment to reduce hydrophobic recovery.

To fabricate agarose microgels, water-in-oil emulsions are generated, such that the aqueous phase contains the desired w/w percentage of low gelling temperature agarose (#A4018-5G, Sigma-Aldrich, St. Louis, MO, USA). The agarose/DI water mixture is heated to 90°C on a heating block for 10 minutes until the agarose is fully dissolved. The liquid agarose solution is then vortexed with mineral oil (1:5 v/v) together with 1% w/w Span 80 for 30 seconds. After filtering the resultant emulsion through a 35  $\mu\text{m}$  mesh filter (BD Biosciences, Franklin Lakes, NJ, USA), the sample is immediately placed on ice for 1 hour to promote gelation and then stored in 4°C overnight. Thereafter, the microgels are removed from the oil phase by adding 5 mL of DI water and centrifuging at 157 x g for 10 minutes. To increase the yield, the samples are shaken vigorously after being removed from the centrifuge and spun down three more times removing the oil from the top of the solution by pipetting. Washing steps are repeated three times to ensure sufficient separation of the water and oil phases. The suspension is filtered one last time through a 35  $\mu\text{m}$  mesh filter.

**Young's modulus characterization of agarose calibration particles.** To determine the elastic modulus of microgels with varying compositions of agarose from 1 to 3% (w/w), particles are indented using an AFM (MFP 3D-BIO system, Asylum Research, Goleta, CA, USA) that is mounted on an inverted microscope (Nikon Ti-E, Tokyo, Japan). To anchor the particles during AFM measurements, we incubate agarose microgels for 30 minutes on a glass substrate pretreated with 0.01% (w/v) poly-L-lysine overnight prior to AFM (Sigma-Aldrich, St. Louis, MO, USA). AFM is performed using a silicon nitride cantilever with an attached 12  $\mu\text{m}$ -diameter borosilicate glass sphere as an indenter (Product #HYDRA6R-200NG-BSG-B-5, AppNano, Mountain View, CA, US). The particles are probed using a 1  $\mu\text{m/s}$  approach velocity. Thereafter, the AFM force curves are fit to the Hertz model with a spherical indenter to determine the



Young's moduli of the agarose microgels (Fig. 2A). We use a Poisson ratio of 0.5. By brightfield imaging of each particle prior to AFM indentation, we measure particle size and confirm that there is no observable dependence of elastic modulus on particle size (S. Fig. 1A).

**Microfluidic device fabrication.** Microfluidic devices are fabricated using standard soft lithography methods (38). To fabricate the master wafer, SU-8 3005 or 3010 (MicroChem, Westborough, MA, USA) is spin-coated on a silicon wafer to a final thickness of 5  $\mu\text{m}$  or 10  $\mu\text{m}$ . A negative photomask is placed on the SU-8-coated wafer and the photoresist is crosslinked upon exposure to UV light with 100  $\text{mJ}/\text{cm}^2$  of exposure energy (35). The height of the resulting relief of the microfluidic channels is measured using a Dektak 150 Surface Profilometer (Veeco, Fullerton, CA). A 10:1 w/w mixture of base and curing agent for polydimethylsiloxane (PDMS) (Sylgard Dow Corning, Midland, MI, USA) is poured onto the master wafer. The mixture is degassed for 1 hour under vacuum and cured in a 65°C oven for 2 hours. Prior to bonding, inlets and outlets are excised using a biopsy punch with a 0.75 mm bore size. To bond the PDMS to a coverglass (#1.5 thickness), the complementary surfaces are exposed to plasma for 30 seconds and press together with light pressure. After bonding, the microfluidic devices are baked at 80°C for 20 minutes to further promote covalent attachment between PDMS and glass. To reduce possible measurement artifacts due to temporal changes in surface properties, devices are consistently used 24 hours after plasma bonding (35).

**q-DC device design.** The q-DC microfluidic device consists of a bifurcating network of channels that extends into a parallel array of 16 channels that contain micron-scale constrictions (27, 28). To reduce the effect of transient channel occlusions as multiple cells transit simultaneously through the constriction region, a bypass channel is included in the device design and post-acquisition filtering is performed to exclude data when more than 10 channels, or 65% of the channels, are occupied (35). Below this cutoff, there are fluctuations in flow rate below 7% variability (35).

**q-DC microfluidic experiment.** To perform q-DC experiments, microfluidic devices are mounted onto an inverted microscope (Zeiss Observer, Zeiss, Oberkochen, Germany) that is equipped with a 20×/0.40 NA objective. To drive the suspension of cells through the channels, constant air pressure is applied to the device inlet, which is regulated using a pneumatic valve (OMEGA Engineering, Inc., Norwalk, CT, USA). As cells flow into the device, a downstream filter traps foreign particles and cell aggregates that are larger than 20  $\mu\text{m}$ . As cells deform through the constrictions (29), brightfield images are acquired at rates of 200 to 2000 frames per second using a CMOS camera (MircoEx4, Vision Research, Wayne, NJ, USA) in order to track cell shape and displacement (Fig. 1A, B). This enables measurements of cell size  $D_{cell}$ , time-dependent strain  $\epsilon(t)$ , critical strain  $\epsilon_{critical}$ , creep time  $T_c$ , and transit time  $T_T$ . When a driving pressure of 28 kPa (4 psi) is applied to a cell suspension with a density of  $2 \times 10^6$  cells/mL, single-cell measurements can be acquired at rates of  $\sim 10^3$  cells/min. For applied pressures of 69 kPa (10 psi), measurements can be acquired at  $\sim 10^4$  cells/min.

To minimize cell-surface interactions, measurements are conducted in the presence of 0.01% (w/v) Pluronic F-127 surfactant (Sigma-Aldrich, St. Louis, MO, USA). For some cell types such as human pancreatic ductal epithelial (HPDE) cells, we qualitatively observe a decrease in cell-PDMS adhesion when Pluronic F-127 surfactant is added to the cell suspension (35); therefore we consistently use this treatment across all cell types. There is no significant quantitative or qualitative effect of F-127 treatment on the  $E_a$  values of HL-60 cells (S. Fig. 2). While cell-surface interactions can contribute to cell transit through long, narrow microfluidic channels, the timescale required by cells to enter microfluidic constrictions is largely determined by cell deformability (32, 33, 35).

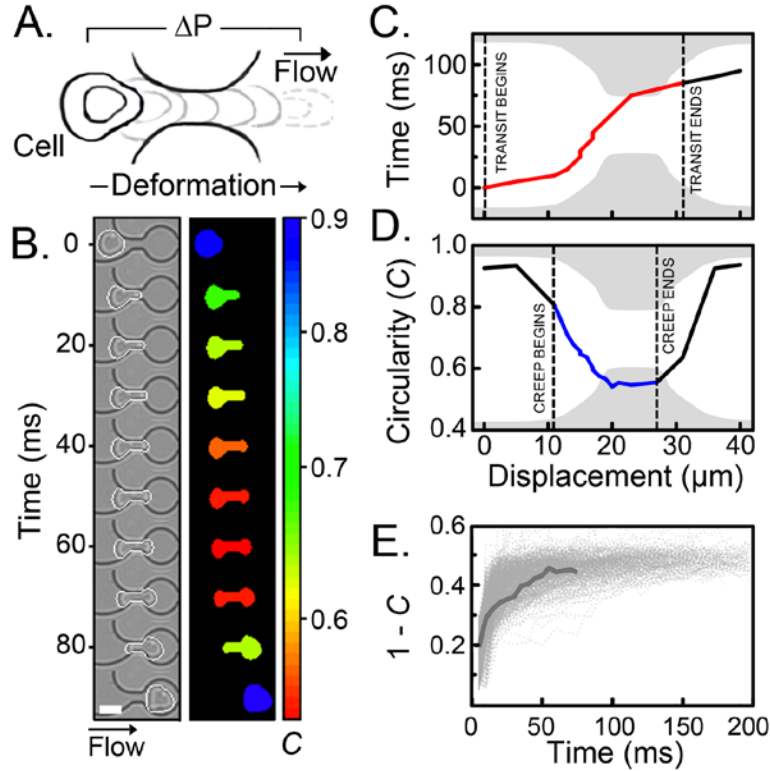


**Fig. 1. Cell shape changes during transit through microfluidic constrictions.** (A) Schematic of a single cell transiting through a micron-scale constriction by pressure-driven flow where  $\Delta P$  is the pressure drop across the cell. Cell shape is evaluated by measuring circularity,  $C(t) = 4\pi A(t)/P(t)^2$ , during transit, and the time-dependent strain,  $\epsilon(t)$ , is defined as  $1 - C(t)$ . (B) Time sequence of a representative HL-60 cell transiting through a microfluidic constriction that exhibits the median transit time and cell size of the cell population. The white border illustrates the cell boundary, as detected by our imaging algorithm. Color overlay illustrates the change in circularity,  $C$ , during deformation. Scale,  $15 \mu\text{m}$ . (C-D) Timescale and shape change during transit through a microfluidic constriction. The x-axis represents the position of the centroid of the cell. We extract: (C) transit time, which is the time required for the leading edge of the cell to enter and exit the constriction region; and (D) time-dependent strain or creep  $\epsilon$ , which is determined by the changes in shape (circularity) of the cell as it deforms into the pore. The creep time begins when the leading edge of the cell enters the constriction; it ends when the centroid exits the constriction, as illustrated by the dashed lines. (E) Creep trajectories for the population of HL-60 cells ( $N = 550$ ). The gray dotted lines represent data from individual cells. The solid gray line represents the creep trajectory of the representative HL-60 cell.

**Tracking of cell strain during deformation through microfluidic constrictions.** To extract cell mechanical properties from transit experiments, cell position and shape are tracked by applying thresholding and morphological filters to the high frame rate images in a MATLAB code (Mathworks, Natick, MA; code available online on GitHub). The creep function,  $J(t)$ , is determined as the ratio between the observed strain and applied stress:

$$J(t) = \frac{\epsilon(t)}{\bar{\sigma}}, \quad \text{Eq. 1}$$

where  $\epsilon(t)$  is the strain and  $\bar{\sigma}$  is the time-averaged stress. Here, the strain is measured as the change in circularity,  $C$ :

$$\epsilon(t) = \frac{C_o - C(t)}{C_o}, \quad \text{Eq. 2}$$

where  $C(t) = 4\pi A(t)/P(t)^2$ . We find that circularity compared to length extension and width compression more robustly captures the deformation of cells through the curved microfluidic constrictions. Prior to entering the constriction, circularity values are close to 1, the value of a perfect circle. Therefore, the initial circularity is set to  $C_o = 1$ . As a cell deforms through a constriction, the strain reaches a maximum as the cell extends and deforms through the narrow gap (Fig. 1B-D). The quantification of creep begins one frame after the leading edge of the particle reaches the constriction, which corresponds to the initial projection of the cell into the constriction, and ends when the centroid of the cell leaves the constriction (Fig. 1). We use a minimum of four frames to achieve sufficient fits for the creep trajectories of individual cells. While fitting to a larger number of >15 frames can improve fitting accuracy, as indicated by the residuals (S. Fig. 3), this would exclude all cells that transit within less than 15 frames, or 7.5 ms. Increasing the frame rate captures cell deformations with higher temporal resolution, but the duration of the video is reduced to 3.7 seconds due to hardware limitations at the maximum frame rate of 3500 frames/sec. Therefore, using a 4 frame cutoff for acquiring q-DC measurements enables us to resolve the power law behavior of individual

cells that are representative of the population by acquiring data across a range of cell deformation timescales from milliseconds to seconds.

**Calibration of time-averaged stress using gel particles.** Since the device has a finite fluidic resistance, the stress applied to a cell as it deforms in the microfluidic constriction does not equate to the applied driving pressure, or  $P_{applied}$ , but rather scales with  $P_{applied}$  as

$$\bar{\sigma} = AP_{applied}, \quad \text{Eq. 3}$$

where  $\bar{\sigma}$  is the time-averaged stress at the constriction region and  $A$  is the calibration factor. To determine  $A$ , we calibrate the system using agarose particles with elastic moduli ( $E$ ) ranging from  $660 \pm 86$  Pa to  $2.4 \pm 0.44$  kPa (average  $\pm$  standard error), as confirmed by AFM (Fig 2A); similar values are observed for agarose particles generated using droplet microfluidics (39).

To achieve particle transit through a fixed pore size, the applied stress must induce a minimum, critical strain,  $\epsilon_{critical}$ . Assuming linear elastic behavior, the scaling factor,  $A$ , can be determined by the stress-strain relation at the threshold conditions where  $P_{applied} = P_{threshold}$ :

$$A = \frac{E\epsilon_{critical}}{P_{threshold}}. \quad \text{Eq. 4}$$

We define the threshold pressure as the minimum applied pressure needed to drive the transit of over ~80% of the particles through the constrictions. For example, when calibration particles with  $E = 1.5 \pm 0.1$  kPa are driven through a  $5 \mu\text{m} \times 5 \mu\text{m}$  device using an applied pressure below  $P_{threshold} = 41$  kPa, the majority of particles occlude the microfluidic constrictions on the experimental timescale of 1 minute. By contrast, with applied pressures above  $P_{threshold}$ , over 80% of particles transit within this timescale. As we use a heterogeneous size distribution of particles, we determine  $P_{threshold}$  and  $\epsilon_{critical}$  for the largest (top 50<sup>th</sup> to 100<sup>th</sup> size percentile) gels that transit through the constriction for a given bead stiffness at  $P_{threshold}$  (S. Fig.

1B). Here, we calculate the critical strain as  $\epsilon_{\text{critical}} = (D_{\text{agarose}} - w_{\text{constriction}})/D_{\text{agarose}}$ . Across the range of particle stiffnesses (0.6 – 2.4 kPa) and strains (40 - 60%) that we investigated, we find a linear relation between stress and strain (Fig 2B), which validates our assumption of linear elasticity.

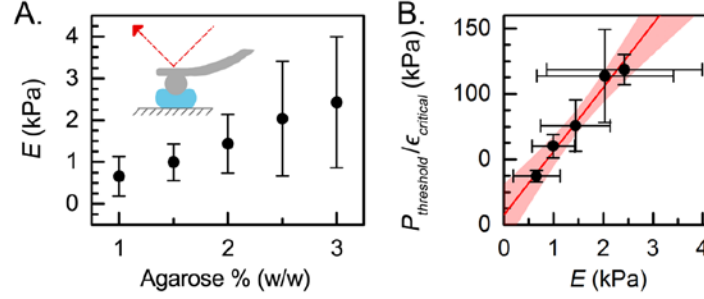


**Fig. 2. Stress calibration using agarose gel particles.** (A) Elastic moduli of gel particles made with varying concentrations of agarose from 1.0 – 3.0% (w/w) as measured by AFM. Data represent average  $\pm$  standard deviation for  $N = 12 - 53$  particles over two independent experiments. (B) Agarose calibration particles are used to determine the applied stresses in the q-DC device by measuring the minimum threshold pressure  $P_{\text{threshold}}$  required to induce a critical strain  $\epsilon_{\text{critical}}$  for a particle to deform through a constricted channel. Shown here is representative data for  $N > 140$  particles transiting through a  $5 \mu\text{m} \times 5 \mu\text{m}$  channel. X-error bars represent the standard deviation of the elastic modulus as in Fig. 2A. Y-error bars represent the standard deviation of the threshold pressure-to-particle strain ratio. The red line is the linear fit determined by the Deming method. The red shaded region illustrates the 95% confidence interval of the fit. The inverse of the slope characterizes the calibration factor,  $A$ .

By performing linear regression using the Deming method on  $P_{\text{threshold}}/\epsilon_{\text{critical}}$  versus  $E$  for our panel of calibration particles, we determine  $A$  for each device geometry (Fig. 2B, S. Fig. 4) (40). We find that  $A$  is  $0.021 \pm 0.002$ , which yields  $\bar{\sigma} \approx 568 \pm 53 \text{ Pa}$  for  $P_{\text{applied}} = 28 \text{ kPa}$  in the  $5 \mu\text{m} \times 5 \mu\text{m}$  device geometry. Combining Eqs. 3 and 4, the resultant creep  $J(t)$  for the  $5 \mu\text{m} \times 5 \mu\text{m}$  device is defined as

$$J(t) = \frac{\epsilon(t)}{0.021 P_{\text{applied}}} . \quad \text{Eq. 5}$$

The Deming method also enables us to determine the error in  $A$  as it considers the error in both  $P_{threshold}/\epsilon_{critical}$  and  $E$ . In addition to the variability in elastic moduli of the calibration particles, error in  $A$  may arise due to fluctuations in applied stress as particles transit and occlude neighboring channels. In our previous analysis of cell transit times, we found transit times significantly decrease when more than 10 neighboring lanes are occupied (35); therefore we analyze data from particles and cells that transit when 10 or less neighboring lanes are occupied. Kirchoff's Law reveals that the flow rate can change by 7% within our experimental range of occluded neighboring lanes of 0 – 10 lanes; this is reflected in the error of applied stress of 10% (35).

**Viscoelastic Cell Adhesion Model (VECAM) simulations.** To provide insight into the stresses on cells as they deform through microfluidic pores, we use VECAM, a three-dimensional multiphase flow algorithm in which each of the phases is modeled as a viscoelastic or Newtonian fluid. The viscoelasticity of the cells and walls of the microchannel are described by the Oldroyd-B constitutive model (41, 42). Similar to our experiments, cells flow through the microchannel of a PDMS device in response to an applied pressure (S. Fig. 6A). The simulations determine the total stresses acting on cells, including fluid shear stresses and normal stresses that result from the pressure drop across the cell as it transiently occludes the pore. To reduce the computational expense of the simulations, cells are modeled to have  $E = 10$  Pa and an apparent viscosity of 1.0 Pa·s. To maintain the same ratio between cell and PDMS stiffness as in our experiments ( $E_{PDMS}/E_{cell} \sim 10^3$ ), the stiffness of the microchannel is modeled as  $E \sim 10^4$  Pa. The carrier fluid of the cells during transit in the device is modeled as a Newtonian fluid.

## Results and Discussion

**Time-dependent cell strain follows power law rheology.** Determining the material properties of cells from transit experiments requires a physical model to describe the relationship between stress and strain. To simplify analysis, we consider the cell as a homogeneous, isotropic, and incompressible material. This enables us to fit mechanical models to the creep trajectories for individual cells, such as the liquid drop and

Kelvin-Voigt models. The deformation of cells entering microfluidic constrictions can be assessed using models that describe cells as liquid droplets (32), elastic solids (26), as well as viscoelastic (43) and soft glassy (31) materials. However, it is not *a priori* known which model best describes the deformations of cells into the microfluidic constriction and provides the most accurate measurement of cell mechanical properties. Here, we evaluate how effectively four viscoelastic models – the Maxwell solid, Kelvin-Voigt, standard linear solid (SLS), and power law rheology (PLR) – describe cell creep through microfluidic constrictions. These models are described in greater detail in the supplemental materials (SI Material).

Our analysis reveals that PLR provides the best fit to our data: the least squares residuals are the lowest for PLR ( $3.9 \pm 0.2 \times 10^{-9} \text{ Pa}^{-2}$ ) compared to other standard viscoelastic models ( $4.8 \pm 0.3 \times 10^{-9} \text{ Pa}^{-2}$  to  $8.0 \pm 0.2 \times 10^{-9} \text{ Pa}^{-2}$ ) (Fig. 3A,B). While an increasing number of fitting parameters can naturally result in reduced residuals, PLR has only two fitting parameters. By contrast, the SLS model has three fitting parameters, but the least squares residuals are higher than for PLR ( $6.0 \pm 0.1 \times 10^{-9} \text{ Pa}^{-2}$ ,  $p \ll 0.001$ ). Our results are consistent with observations of PLR behavior in cells that are subjected to stresses by micropipette aspiration (44), optical stretching (2), transit DC (31, 34), AFM (20), and magnetic twisting cytometry (45).

Using PLR, we extract the mechanical properties of single cells as they deform through microfluidic constrictions by analysis of the time-dependent creep function,

$$J(t) = \frac{1}{E} \left( \frac{t}{\tau} \right)^\beta, \quad \text{Eq. 6}$$

where  $\tau$  is the characteristic timescale, which is commonly set to 1 s;  $E$  is the elastic modulus when  $t = \tau$ ; and  $\beta$  is the power law exponent that reflects the rate of stress dissipation and thus provides a measure of cell fluidity. When  $\beta = 0$ , the creep function describes a purely elastic material and Eq. 6 reduces to Hooke's law; when  $\beta = 1$ , Eq. 6 reduces to the Newtonian liquid drop model, reflecting a purely viscous material. While our data is consistent with PLR, we refer to the elastic modulus that we measure using q-DC as the



apparent elastic modulus  $E_a$  because of the potential nonlinear effects that may contribute to our measurements with the large 30 to 60 % strains in q-DC.

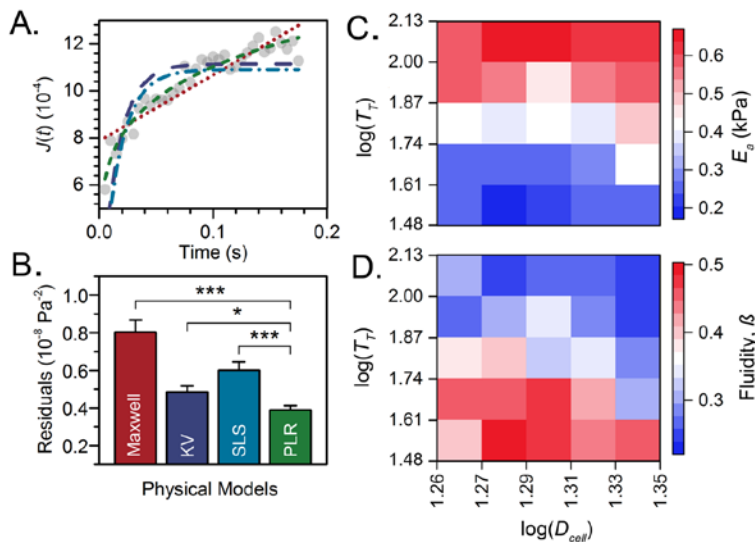


**Fig. 3. Power law rheology for cell mechanotyping by q-DC.** (A) Creep trajectory for a single, representative HL-60 cell (gray dots). Lines represent the least-squares fits of viscoelastic models to the creep data: Maxwell (red dotted line); Kelvin-Voigt (KV, purple long-dashed line); standard linear solid (SLS, blue dot-dashed line); and power law rheology (PLR, green short-dashed line). (B) Residuals for the least-squares fits of the viscoelastic models to the creep trajectories of a population of HL-60 cells ( $N = 550$ ), as shown in Fig. 1E. Shown here are the bootstrapped median residuals; error bars represent the bootstrapped confidence interval.  $*p < 0.05$ ,  $***p \ll 0.001$ . (C-D) Heat maps show the (C) apparent elastic modulus,  $E_a$ , and (D) fluidity,  $\beta$ , of HL-60 cells as a function of transit time,  $T_T$ , and cell diameter,  $D_{cell}$ , which is measured in the microfluidic channel before the cell enters the constriction. Each bin represents the median  $E_a$  or  $\beta$  of  $N = 3 - 47$  single cells.

We also recognize that these mechanical measurements assume constant stress during cell transit. As shown by Viscoelastic Cell Adhesion Model (VECAM) simulations, the total stress on a cell varies as it deforms through a pore (S. Fig. 6). As the cell transits through the pore, there is a drop in the hydrodynamic forces on the cell, which are proportional to the cell velocity according to Stokes' law (S. Fig. 6B). In addition, there is a pressure drop across the cell, where the applied pressure  $P_{app}$  at the trailing edge is higher than the pressure at the cell's leading edge, which is approximated by atmospheric pressure,  $P_{atm}$  (S. Fig. 6C).

Thus, when the cell is transiently occluding the pore, there are positive normal forces that deform the cell, and which vary during cell translocation due to the curved geometry of the pore.

**Validation of PLR using oil droplets.** To validate the use of PLR in q-DC, we first quantify  $\beta$ , or fluidity, for droplets of silicone oil. We predict  $\beta = 1$  for droplets of silicone oils, which are Newtonian fluids. We generate oil droplets that have a range of molecular weights and thus dynamic viscosities,  $\eta$ , from  $10^{-2}$  to  $10^1$  Pa·s, and flow them through the constrictions at a constant driving pressure of 28 kPa. From 1000 random samplings of the  $\beta$  distributions, we obtain median bootstrapped values and confidence intervals of  $\beta$ . We observe  $\beta = 0.78 \pm 0.08$  for the lowest viscosity silicone oil ( $\eta = 10^{-2}$  Pa·s) (S. Fig. 4), which is close to purely viscous behavior. With increasing viscosity, we observe decreasing  $\beta$ , where the highest viscosity oil droplets ( $\eta = 10^1$  Pa·s) exhibit  $\beta = 0.54 \pm 0.02$ . This decrease in  $\beta$  with increasing viscosity suggests a progressively increasing elastic response, which occurs due to the fast millisecond timescales of our measurements compared to the timescale of molecular rearrangements in the silicone oils that have increased molecular weight.

**Single cell measurements of elastic modulus and fluidity.** To demonstrate the utility of q-DC for cell mechanotyping, we measure HL-60 cells, whose mechanical properties are well characterized using methods such as micropipette aspiration (46), AFM (47, 48), and optical stretching (16) (S. Table 3). Our results show that HL-60 cells have a median  $E_a$  and confidence interval of  $0.53 \pm 0.04$  kPa ( $\beta = 0.29 \pm 0.02$ ), as measured by 1000 iterations of bootstrapped resampling (Fig. 3, S. Table 2); this is on the same order of magnitude as values obtained using AFM, where  $E = 0.9 \pm 0.7$  kPa (47) and  $E = 0.9 \pm 0.2$  kPa (48) (S. Table 3).

Since q-DC quantifies the mechanotype of single cells, the variability in mechanical properties across a cell population can be determined. To describe cell-to-cell variability, we use the interquartile range (IQR) as a quantitative metric. For HL-60 cells, the IQR spans half an order of magnitude from 0.30 to 0.71 kPa, as

measured by  $\sigma_{\text{IQR}_{E_a}} = \log_{10}(75^{\text{th}}/25^{\text{th}} \text{ percentile}) = 0.35 \pm 0.06$ . We also find significant variability in  $\beta$  with  $\sigma_{\text{IQR}_{\beta}} = 0.25 \pm 0.03$ .

By plotting  $E_a$  and  $\beta$  vs.  $D_{\text{cell}}$ , we observe that larger cells tend to have higher  $E_a$  (Fig. 2C, Fig. 3A) and reduced  $\beta$  (Fig. 2D, Fig. 3A). For example, we find that for cells with  $D_{\text{cell}} = 18 \pm 1 \mu\text{m}$ ,  $E_a = 0.37 \pm 0.06$  kPa and  $\beta = 0.37 \pm 0.04$ , whereas larger cells with  $D_{\text{cell}} = 22 \pm 1 \mu\text{m}$  have  $E_a = 0.59 \pm 0.04$  kPa and  $\beta = 0.26 \pm 0.02$  (Fig. 2C,D). Size-dependence of cell mechanotype is also observed in other DC methods, where larger cells have longer transit times (31–33, 35) and exhibit more significant changes in shape due to forces exerted by fluid flow (23, 25). While larger cells could be inherently stiffer than smaller cells, larger cells undergo larger strains as the constriction width is fixed (S. Fig. 7). Since cells are non-linear materials, the length and time scales of deformation may influence their  $E_a$  as observed in cells (20–22, 49–52) and biopolymer networks (20, 49, 53–55).

**Cell-to-pore size ratio affects mechanotype.** To further investigate the cell-to-pore size dependence of  $E_a$ , we vary the constriction width from 5  $\mu\text{m}$  to 9  $\mu\text{m}$ , while maintaining a constant constriction height of 10  $\mu\text{m}$ ; thus, we achieve median cell-to-pore size ratios of  $\sim 3$  and 1.5. To ensure cells are subjected to the same applied stress while undergoing different critical strains, we utilize the agarose calibration beads to determine the required applied pressures for each constriction geometry:  $P_{\text{applied}} = 14$  kPa for 5  $\mu\text{m} \times 10 \mu\text{m}$  geometry and  $P_{\text{applied}} = 34$  kPa for the 9  $\mu\text{m} \times 10 \mu\text{m}$  device (S. Table. 4). For cells of  $D_{\text{cell}} = 16 \pm 1 \mu\text{m}$ , we observe a significant 70% decrease in  $E_a$  when measured using a 9  $\mu\text{m}$  width constriction ( $E_a = 230 \pm 90$  Pa), as compared to the 5  $\mu\text{m}$ -wide geometry ( $E_a = 860 \pm 230$  Pa,  $p \ll 0.001$ ). These results suggest that the magnitude of cell strain affects  $E_a$  and are consistent with observations of strain stiffening in mechanical measurements of cells and biopolymer networks (10, 54). Our findings of how mechanotype depends on cell-to-pore size ratio also substantiates the comparison of cells of similar sizes across samples.

Cells are also spatially heterogeneous materials. Therefore, the magnitude of deformation depth, or strain, may impact the resultant mechanotype measurements. The nucleus is a major contributor to subcellular

deformations: this organelle is typically 2- to 5-times stiffer than the surrounding cytoplasmic region (11), and rate-limits the deformation of cells through microfluidic channels that are smaller than the diameter of the nucleus (28). HL-60 cell nuclei range in diameter from 5 to 14  $\mu\text{m}$  and have an average size of  $9.2 \pm 2.0 \mu\text{m}$  (S. Fig. 9); thus for most cells, the nucleus must deform when cells transit through a 5  $\mu\text{m}$ - or 9  $\mu\text{m}$ -wide constriction. By quantitative image analysis, we find that larger HL-60 cells tend to have larger nuclei, as indicated by the positive correlation ( $R = 0.8$ ) between nuclear and cellular diameter (S. Fig. 9A). Thus, the increased  $E_a$  observed for larger cells could also result from the increased deformation of the nucleus that is required for transit. A similar increase in Young's modulus is observed with increasing AFM indentation depth into the nucleus (11). The dependence of cell and nuclear size on the deformation response of cells as they deform through pores further underscores the importance of comparing q-DC data from cells that undergo a similar magnitude of strain (S. Fig. 7). These findings also provide a guide for establishing parameters in q-DC experiments: a cell-to-pore size ratio of  $\sim 2$  ensures cell deformation is required for transit through the pore, and typically results in a strain of 35 - 40%, which is on the lower range of cell strains that can be achieved with q-DC, and therefore minimizes strain-stiffening effects.

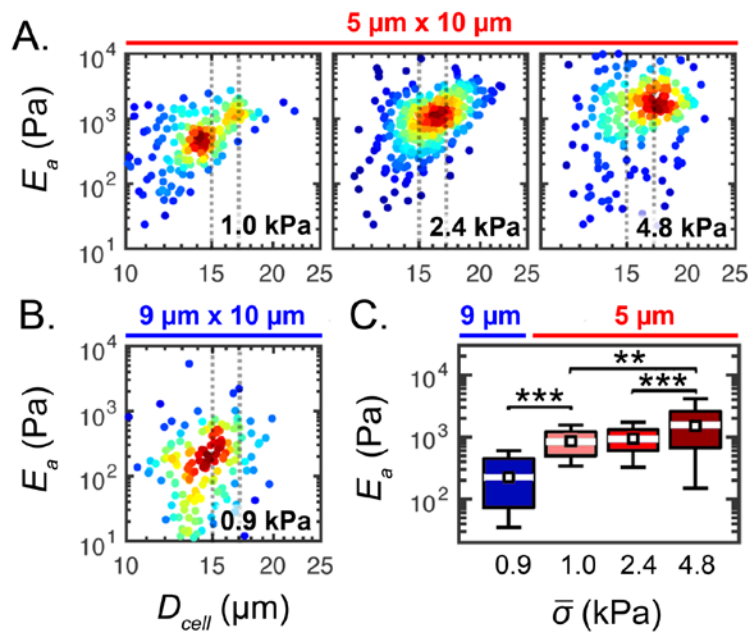


**Fig 4. Mechanotype of HL-60 cells depends on applied pressure and cell-to-pore size ratio.**

(A) Density scatter plots show apparent elastic modulus  $E_a$  as a function of cell size. The cell diameter  $D_{cell}$  is measured in the microfluidic channel before the cell enters the constriction. Data represents the deformation response for HL-60 cells that are driven to deform through  $5 \mu\text{m} \times 10 \mu\text{m}$  constrictions with increasing applied pressure. The calibrated applied stress is marked on the bottom right corner of each panel. Dots represent single cell data. Color represents the density of data points. Cell size measured by q-DC increases with applied pressure, as there is a higher probability that larger cells will transit at higher pressures; at lower pressures, larger cells have a higher probability of occluding constrictions. To compare data sets, we bin cells by the median cell diameter, as indicated by the gray dashed line; the resultant size-binned data is shown in the boxplots. (B) Density scatter plot illustrates elastic modulus  $E_a$  as a function of cell size for HL-60 cells deforming through  $9 \mu\text{m} \times 10 \mu\text{m}$  constrictions. (C) Boxplots show the size-gated distributions of  $E_a$  for HL-60 cells with  $D_{cell} = 16 \pm 1 \mu\text{m}$ . Cells are subject to varying applied stresses,  $\bar{\sigma}$ , and constriction geometries: white lines represent the median, boxes represent the interquartile ranges, whiskers represent the 10<sup>th</sup> and 90<sup>th</sup> percentiles, and white squares represent the bootstrapped median.  $N > 200$  for each cell type. Statistical significance is determined using the Mann-Whitney U test: \* $p < 0.05$ , \*\* $p < 0.01$ , \*\*\* $p < 0.001$ .

**Stress-stiffening behavior of cells using q-DC.** To determine the effects of applied stress on cell deformation behavior in q-DC, we drive HL-60 cells through  $5 \mu\text{m} \times 10 \mu\text{m}$  constrictions with increasing applied pressures from 14 – 69 kPa. From our calibration, we determine the corresponding range of applied stress to be  $\bar{\sigma} = 1.0$  to 4.8 kPa. With an increase in  $\bar{\sigma}$  from 1.0 to 2.4 kPa, we find a small 10%, albeit not significant, increase in elastic modulus ( $p = 0.34$ ). Further increasing  $\bar{\sigma}$  to 4.8 kPa, we observe a statistically significant stiffening reflected by the 60% increase in  $E_a$  ( $p < 0.001$ ). From  $\bar{\sigma} = 1.0$  to 4.8 kPa we observe a significant 70% increase in  $E_a$  from  $860 \pm 230 \text{ Pa}$  to  $1.5 \pm 0.5 \text{ kPa}$  ( $p = 0.003$ ) (Fig. 4A, S. Table. 4). Taken together, these results indicate stress stiffening response of HL-60 cells on these deformation timescales of milliseconds to seconds. The stress stiffening behavior of cells is observed across varying cell types from airway smooth muscle cells to fibroblasts (2, 20, 49, 56). Therefore, we consider cells of similar sizes when comparing between populations of single cells to minimize possible bias from strain and stress on q-DC measurements.

**Validation of mechanical measurements using HL-60 cells.** To demonstrate the sensitivity of q-DC to changes in cytoskeletal structure, we treat HL-60 cells with cytoskeletal perturbing drugs, which are known to alter cell mechanical properties (10, 46, 57, 58). For example, treatment with cytochalasin D inhibits F-actin polymerization (27), while treatment with jasplakinolide inhibits F-actin depolymerization, thus stabilizing actin filaments. To compare cells of similar size, we size bin our data to investigate cells of the median diameter,  $D_{cell} = 21 \pm 1 \mu\text{m}$ , of HL-60 cells across all drug treatments (Fig. 5A). We find that treatment with cytochalasin D results in a small but significant decrease in  $E_a$  from  $0.53 \pm 0.04$  to  $0.39 \pm 0.05$  kPa with an increase in cell-to-cell variability, from  $\sigma_{\text{IQR}_Ea} = 0.35 \pm 0.06$  to  $0.46 \pm 0.08$  ( $p \ll 0.001$ ) (Fig. 5). In addition, we observe cytochalasin D treatment results in a marginal increase in cell fluidity from  $\beta = 0.29 \pm 0.02$ , to  $\beta = 0.34 \pm 0.03$  ( $p = 0.006$ ), as well as an increased variability in fluidity from  $\sigma_{\text{IQR}_\beta} = 0.25 \pm 0.03$  to  $\sigma_{\text{IQR}_\beta} = 0.33 \pm 0.04$  (Fig. 5B). By contrast, stabilizing F-actin with jasplakinolide treatment insignificantly increases  $E_a$  to  $0.54 \pm 0.06$  kPa and  $\sigma_{\text{IQR}_Ea} = 0.30 \pm 0.06$ ; we also observe a concomitant, significant decrease in  $\beta$  to  $0.27 \pm 0.03$  with  $\sigma_{\text{IQR}_\beta} = 0.27 \pm 0.06$  v (Fig. 5B). Our observations of the effects of cytochalasin D and jasplakinolide are consistent with previous studies investigating the contributions of F-actin to cell transit through micron-scale channels (27, 32, 59, 60). These results demonstrate the proof-of-concept and utility of q-DC to achieve mechanical measurements of single cells with increased throughput.

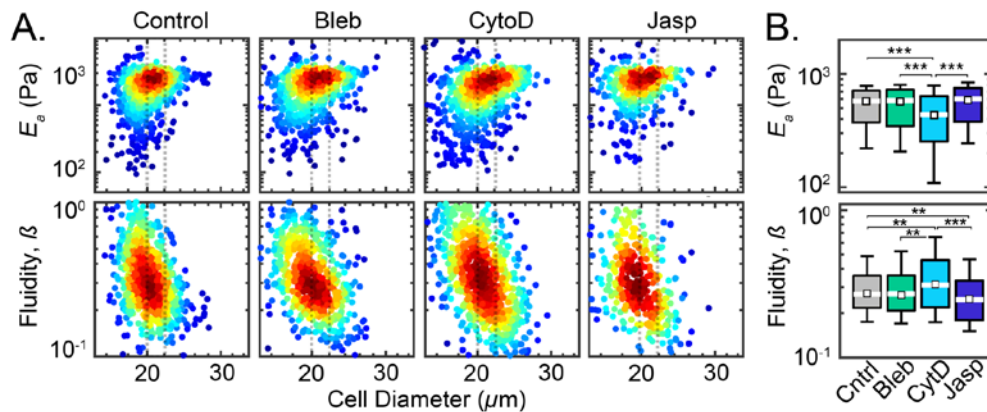


**Fig. 5. Mechanotyping of HL-60 cells treated with cytoskeletal-perturbing drugs using q-DC.**

HL-60 cells are treated with blebbistatin (Bleb), cytochalasin D (CytD), and jasplakinolide (Jasp). (A) Density scatter plots show apparent elastic modulus  $E_a$  and fluidity  $\beta$  as functions of cell size, which is measured in the microfluidic channel before the cell enters the constriction. The cell diameter shown here is larger than the actual cell diameter (S. Fig. 8A) as cells are confined when flowing through the microfluidic device with 5  $\mu\text{m}$  height. Each dot represents a single cell. Color represents the density of data points. To compare data sets, we bin cells by size, as depicted by the gray dotted lines. Cell size distributions are shown in S. Fig. 8. Cell size measured by q-DC in these 5  $\mu\text{m}$ -height devices is larger than cell size in the 10  $\mu\text{m}$ -height devices (Fig 4), due to the axial compression that occurs when the device height is smaller than the cell diameter. (B) Boxplots represent the size-binned distributions of  $E_a$  and  $\beta$  for cells with  $D_{cell} = 21 \pm 1 \mu\text{m}$ , white lines represent the median, boxes represent the interquartile ranges, whiskers represent the 10<sup>th</sup> and 90<sup>th</sup> percentiles, and white squares represent the bootstrapped median.  $N > 500$  for each cell type. Statistical significance is determined using the Mann-Whitney U test: \* $p < 0.05$ , \*\* $p < 0.01$ , \*\*\* $p < 0.001$ .

We also investigate the effects of blebbistatin, which inhibits myosin II activity, and thus reduces crosslinking and actomyosin contractions. We observe no significant change in  $E_a$  following blebbistatin treatment as  $E_a = 0.52 \pm 0.06 \text{ kPa}$  and  $\sigma_{\text{IQR}_Ea} = 0.40 \pm 0.09$ . We observe a slight increase in cell fluidity to  $\beta = 0.29 \pm 0.02$  and  $\sigma_{\text{IQR}_\beta} = 0.28 \pm 0.05$ ; however this difference is not significant (Fig. 5A,B). Previous observations show that blebbistatin treatment decreases the stiffness in adhered cells, as indicated by their reduced  $E$  (61), and suspended cells, as indicated by their reduced transit time (59). However, other measurements of suspended cells show increased stiffness with inhibition of myosin II (36). As minor differences in blebbistatin concentrations and treatment times across studies do not seem to explain the observed differences in the mechanotype of cells in suspension, we speculate that the varied results may be explained by considering deformation depth. In methods that deform cells by  $\sim 5$  to 6  $\mu\text{m}$  (59), the nucleus may contribute more prominently to the deformation response; myosin II inhibition could cause softening of the ‘prestressed’ nucleus as intracellular tension diminishes. By contrast, when cells are subjected to smaller, 1 to 3  $\mu\text{m}$  deformations (36), the cortical region may dominate the response; a less deformable cortex may result from decreased turnover of actin due to blebbistatin treatment. We also acknowledge that

differences in cell genotype, culture conditions, and passage number of cell lines may also contribute to the varied results observed between studies.

**Mechanotyping cancer cell lines.** To further benchmark our q-DC method, we next investigate the human breast cancer cell lines, MCF-7 and MDA-MB-231, whose mechanical properties are well characterized using methods including AFM and transit DC (S. Table 3). Since these breast cancer cells tend to be larger and stiffer than HL-60 cells(11), we use a  $9\ \mu\text{m} \times 10\ \mu\text{m}$  pore size with an applied stress of  $2.2 \pm 0.1\ \text{kPa}$ , which ensures  $>95\%$  of cells transit through the pores on the experimental timescale (S. Fig. 3B); this enables us to acquire single cell measurements with a throughput of  $10^3$  cells/min. For MCF-7 cells with  $D_{cell} = 21 \pm 1\ \mu\text{m}$ , we observe  $E_a = 2.4 \pm 0.2\ \text{kPa}$  (Fig. 6). We also measure MDA-MB-231 cells within the same size range, and find that  $E_a = 0.97 \pm 0.50\ \text{kPa}$ , which is 40% lower than MCF-7 cells ( $p \ll 0.001$ ). Our findings that MDA-MB-231 cells are more compliant than MCF-7 cells are in agreement with previous reports (62, 63) (S. Table 2). Using AFM and magnetic twisting cytometry,  $E$  for MCF-7 cells typically range from 0.2 to 1 kPa (62, 64–67), while for MDA-MB-231 cells  $E$  varies from 0.2 to 0.69 kPa (11, 31, 62, 64, 65, 67). Considering the relatively higher 30 to 60% strains that are applied in q-DC compared to the local,  $< \mu\text{m}$  indentations of AFM, the higher  $E_a$  values for MCF-7 cells that we observe are consistent with the dependence of  $E$  on deformation depth: MDA-MB-231 that are indented with  $0.1\ \mu\text{m}$  deformation depths that penetrate into the nuclear region exhibit a 5-fold increase in Young's moduli compared to  $0.8\text{-}\mu\text{m}$  deformation depths (11, 62). Our measurements also reveal that  $E_a$  and  $\beta$  are inversely correlated for the breast cancer cells, where  $\beta = 0.28 \pm 0.01$  for MCF-7 cells and  $\beta = 0.40 \pm 0.03$  for MDA-MB-231 cells ( $p \ll 0.001$ ) (Fig. 4, S. Fig. 6B); the inverse correlation is consistent soft glassy rheology (2, 20, 31).



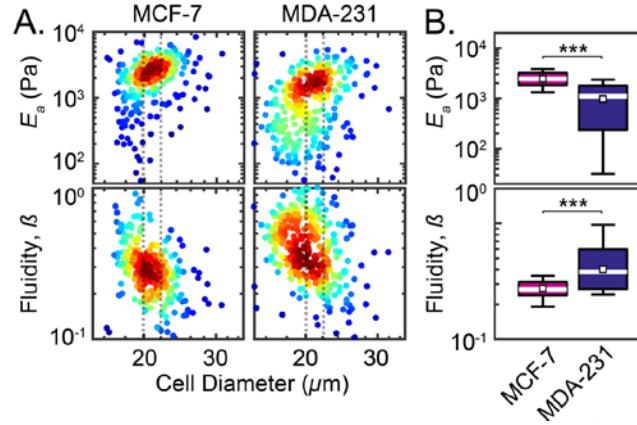


**Fig. 6. Mechanotyping of human breast cancer cell lines using q-DC.** (A) Density scatter plots show  $E_a$  and  $\beta$  as functions of cell size for MCF-7 and MDA-231 cell lines. Color represents the density of data points. To compare cell populations, we bin data by cell size, as depicted by the grey dotted lines. Cell diameter is measured in the microfluidic channel before the cell enters the constriction. (B) Boxplots represent the size-binned distributions of  $E_a$  and  $\beta$  for cells with  $D_{cell} = 21 \pm 1 \mu\text{m}$ . White lines represent the median. Boxes denote the interquartile ranges and whiskers denote the 10<sup>th</sup>–90<sup>th</sup> percentiles. White squares represent the bootstrapped medians.  $N > 100$  for each cell type. The Mann-Whitney U test is used to determine statistical significance: \* $p < 0.05$ , \*\* $p < 0.01$ , \*\*\* $p < 0.001$ .

The differences in the mechanotype of MCF-7 and MDA-MB-231 cells that we observe may reflect underlying molecular differences between these cell lines. These cell types also exhibit distinct invasive behaviors: MDA-MB-231 cells are more invasive than the MCF-7 cells (68). While correlations between cancer cell invasive potential and mechanical properties are observed in other contexts (5, 7, 11, 69), the causal role of cell mechanotype in behaviors such as invasion is still unclear. The mechanotype of cancer cells could also have implications in how disseminated tumor cells resist shear forces during circulation and occlude narrow gaps, which is required for seeding metastatic sites. The ability of cells to transit versus occlude narrow capillaries is also critical for the deformability of blood cells, ranging from sickle cells (70, 71) to immunology (16, 72); in these contexts, changes in cell mechanotype have distinct biological implications. Furthermore, the evidence of stress and strain stiffening that we observe as cells undergo large 40-60% strains through micron-scale gaps may be advantageous for cells to resist significant deformations in vivo.

While the biological relevance of mechanotype – which is most often measured *in vitro* – still remains an open question, it is notable that biological relevance is not a requisite to establish a valuable biomarker. For example, nuclear shape has been a diagnostic biomarker in breast and cervical cancers for decades (73), while the biological significance of the aberrant nuclear morphology of cancer cells remains unclear. Thus, robust differences in mechanotypes across cell types, which can be achieved using calibrated measurements, should have clinical value.

## **Conclusions**

Here we present a framework that uses calibration particles to quantify the external stresses in q-DC, a fluidic-based method that enables rapid measurements of cell mechanical properties. The use of calibration particles should ultimately enable standardized mechanotyping and longitudinal studies in clinical and research settings. To extract quantitative measurements of cell elasticity and fluidity, we use power law rheology (PLR), which is an effective analytical model for describing cell creep through microfluidic constrictions on timescales of milliseconds to seconds. Future studies will clarify the extent to which q-DC mechanotyping results add value as a biomarker, as well as the extent to which cell mechanotype impacts biological processes in physiology and disease.

## References

1. Pajerowski, J.D., K.N. Dahl, F.L. Zhong, P.J. Sammak, and D.E. Discher. 2007. Physical plasticity of the nucleus in stem cell differentiation. *Proc. Natl. Acad. Sci.* 104: 15619–15624.
2. Maloney, J.M., D. Nikova, F. Lautenschläger, E. Clarke, R. Langer, J. Guck, and K.J. Van Vliet. 2010. Mesenchymal stem cell mechanics from the attached to the suspended state. *Biophys. J.* 99: 2479–87.
3. Engler, A.J., S. Sen, H.L. Sweeney, and D.E. Discher. 2006. Matrix Elasticity Directs Stem Cell Lineage Specification. *Cell.* 126: 677–689.
4. Chowdhury, F., S. Na, D. Li, Y.-C. Poh, T.S. Tanaka, F. Wang, and N. Wang. 2010. Material properties of the cell dictate stress-induced spreading and differentiation in embryonic stem cells. *Nat. Mater.* 9: 82–88.
5. Xu, W., R. Mezencev, B. Kim, L. Wang, J. McDonald, and T. Sulchek. 2012. Cell stiffness is a biomarker of the metastatic potential of ovarian cancer cells. *PLoS One.* 7: e46609.
6. Qi, D., N.K. Gill, C. Santiskulvong, J. Sifuentes, O. Dorigo, J. Rao, B. Taylor-Harding, W.R. Wiedemeyer, and A.C. Rowat. 2015. Screening cell mechanotype by parallel microfiltration. *Sci. Rep.* 5.
7. Nguyen, A. V, K.D. Nyberg, M.B. Scott, A.M. Welsh, A.H. Nguyen, N. Wu, S. V Hohlbauch, N.A. Geisse, E.A. Gibb, A.G. Robertson, T.R. Donahue, and A.C. Rowat. 2016. Stiffness of pancreatic cancer cells is associated with increased invasive potential. *Integr. Biol.* .
8. Henry, T.K., D.R. Gossett, Y.S. Moon, M. Masaeli, M. Sohsman, Y. Ying, K. Mislick, R.P. Adams, J. Rao, and D. Di Carlo. 2013. Quantitative diagnosis of malignant pleural effusions by single-cell mechanophenotyping. *Sci. Transl. Med.* 5: 212ra163--212ra163.
9. Lee, W.C., H. Shi, Z. Poon, L.M. Nyan, T. Kaushik, G. V Shivashankar, J.K.Y. Chan, C.T. Lim, J. Han, and K.J. Van Vliet. 2014. Multivariate biophysical markers predictive of mesenchymal

- stromal cell multipotency. *Proc. Natl. Acad. Sci.* 111: E4409-18.
10. Rotsch, C., and M. Radmacher. 2000. Drug-induced changes of cytoskeletal structure and mechanics in fibroblasts: an atomic force microscopy study. *Biophys. J.* 78: 520–535.
  11. Agus, D.B., J.F. Alexander, W. Arap, S. Ashili, J.E. Aslan, R.H. Austin, V. Backman, K.J. Bethel, R. Bonneau, W.-C. Chen, C. Chen-Tanyolac, N.C. Choi, S.A. Curley, M. Dallas, D. Damania, P.C.W. Davies, P. Decuzzi, L. Dickinson, L. Estevez-Salmeron, V. Estrella, M. Ferrari, C. Fischbach, J. Foo, S.I. Fraley, C. Frantz, A. Fuhrmann, P. Gascard, R.A. Gatenby, Y. Geng, S. Gerecht, R.J. Gillies, B. Godin, W.M. Grady, A. Greenfield, C. Hemphill, B.L. Hempstead, A. Hielscher, W.D. Hillis, E.C. Holland, A. Ibrahim-Hashim, T. Jacks, R.H. Johnson, A. Joo, J.E. Katz, L. Kelbaskas, C. Kesselman, M.R. King, K. Konstantopoulos, C.M. Kraning-Rush, P. Kuhn, K. Kung, B. Kwee, J.N. Lakins, G. Lambert, D. Liao, J.D. Licht, J.T. Liphardt, L. Liu, M.C. Lloyd, A. Lyubimova, P. Mallick, J. Marko, O.J.T. McCarty, D.R. Meldrum, F. Michor, S.M. Mumenthaler, V. Nandakumar, T. V O'Halloran, S. Oh, R. Pasqualini, M.J. Paszek, K.G. Philips, C.S. Poultney, K. Rana, C.A. Reinhart-King, R. Ros, G.L. Semenza, P. Senechal, M.L. Shuler, S. Srinivasan, J.R. Staunton, Y. Stypula, H. Subramanian, T.D. Tlsty, G.W. Tormoen, Y. Tseng, A. van Oudenaarden, S.S. Verbridge, J.C. Wan, V.M. Weaver, J. Widom, C. Will, D. Wirtz, J. Wojtkowiak, and P.-H. Wu. 2013. A physical sciences network characterization of non-tumorigenic and metastatic cells. *Sci. Rep.* 3: 1449.
  12. Evans, E., and A. Yeung. 1989. Apparent viscosity and cortical tension of blood granulocytes determined by micropipet aspiration. *Biophys. J.* 56: 151–160.
  13. Needham, D., and R.M. Hochmuth. 1990. Rapid flow of passive neutrophils into a 4 microns pipet and measurement of cytoplasmic viscosity. *J. Biomech. Eng.* 112: 269–76.
  14. Tsai, M.A., R.S. Frank, and R.E. Waugh. 1993. Passive mechanical behavior of human neutrophils: power-law fluid. *Biophys. J.* 65: 2078–2088.
  15. Zhang, H., and K.-K. Liu. 2008. Optical tweezers for single cells. *J. R. Soc. Interface.* 5: 671–690.

16. Ekpenyong, A.E., G. Whyte, K. Chalut, S. Pagliara, F. Lautenschläger, C. Fiddler, S. Paschke, U.F. Keyser, E.R. Chilvers, and J. Guck. 2012. Viscoelastic Properties of Differentiating Blood Cells Are Fate- and Function-Dependent. *PLoS One*. 7.
17. Guck, J., S. Schinkinger, B. Lincoln, F. Wottawah, S. Ebert, M. Romeyke, D. Lenz, H.M. Erickson, R. Ananthkrishnan, D. Mitchell, J. Käs, S. Ulvick, and C. Bilby. 2005. Optical Deformability as an Inherent Cell Marker for Testing Malignant Transformation and Metastatic Competence. *Biophys. J.* 88: 3689–3698.
18. Thoumine, O., and A. Ott. 1997. Time scale dependent viscoelastic and contractile regimes in fibroblasts probed by microplate manipulation. *J. Cell Sci.* 110 ( Pt 1: 2109–2116.
19. Caille, N., O. Thoumine, Y. Tardy, and J.-J. Meister. 2002. Contribution of the nucleus to the mechanical properties of endothelial cells. *J. Biomech.* 35: 177–187.
20. Fabry, B., G.N. Maksym, J.P. Butler, M. Glogauer, D. Navajas, and J.J. Fredberg. 2001. Scaling the microrheology of living cells. *Phys. Rev. Lett.* 87: 148102.
21. Desprat, N., A. Richert, J. Simeon, and A. Asnacios. 2005. Creep function of a single living cell. *Biophys. J.* 88: 2224–2233.
22. Deng, L., X. Trepate, J.P. Butler, E. Millet, K.G. Morgan, D.A. Weitz, and J.J. Fredberg. 2006. Fast and slow dynamics of the cytoskeleton. *Nat. Mater.* 5: 636–640.
23. Otto, O., P. Rosendahl, A. Mietke, S. Golfier, C. Herold, D. Klaue, S. Girardo, S. Pagliara, A. Ekpenyong, A. Jacobi, M. Wobus, N. Töpfner, U.F. Keyser, J. Mansfeld, E. Fischer-Friedrich, and J. Guck. 2015. Real-time deformability cytometry: on-the-fly cell mechanical phenotyping. *Nat. Methods.* 12.
24. Che, J., V. Yu, M. Dhar, C. Renier, M. Matsumoto, K. Heirich, E.B. Garon, J. Goldman, J. Rao, G.W. Sledge, M.D. Pegram, S. Sheth, S.S. Jeffrey, R.P. Kulkarni, E. Sollier, and D. Di Carlo. 2016. Classification of large circulating tumor cells isolated with ultra-high throughput

- microfluidic Vortex technology. *Oncotarget*. 7: 12748–12760.
25. Gossett, D.R., H.T.K. Tse, S. a. Lee, Y. Ying, A.G. Lindgren, O.O. Yang, J. Rao, A.T. Clark, and D. Di Carlo. 2012. Hydrodynamic stretching of single cells for large population mechanical phenotyping. *Proc. Natl. Acad. Sci.* 109: 7630–5.
  26. Mietke, A., O. Otto, S. Girardo, P. Rosendahl, A. Taubenberger, S. Golfier, E. Ulbricht, S. Aland, J. Guck, and E. Fischer-Friedrich. 2015. Extracting Cell Stiffness from Real-Time Deformability Cytometry: Theory and Experiment. *Biophys. J.* 109: 2023–2036.
  27. Rosenbluth, M.J., W. a Lam, and D. a Fletcher. 2008. Analyzing cell mechanics in hematologic diseases with microfluidic biophysical flow cytometry. *Lab Chip*. 8: 1062–1070.
  28. Rowat, A.C., D.E. Jaalouk, M. Zwerger, W.L. Ung, I.A. Eydelnant, D.E. Olins, A.L. Olins, H. Herrmann, D.A. Weitz, and J. Lammerding. 2013. Nuclear Envelope Composition Determines the Ability of Neutrophil-type Cells to Passage through Micron-scale Constrictions. *J. Biol. Chem.* 288: 8610–8618.
  29. Hoelzle, D.J., B.A. Varghese, C.K. Chan, and A.C. Rowat. 2014. A Microfluidic Technique to Probe Cell Deformability. *JoVE*. 91: e51474–e51474.
  30. Hou, H.W., Q.S. Li, G.Y.H. Lee, a. P. Kumar, C.N. Ong, and C.T. Lim. 2009. Deformability study of breast cancer cells using microfluidics. *Biomed. Microdevices*. 11: 557–564.
  31. Lange, J.R., J. Steinwachs, T. Kolb, L.A. Lautscham, I. Harder, G. Whyte, and B. Fabry. 2015. Microconstriction Arrays for High-Throughput Quantitative Measurements of Cell Mechanical Properties. *Biophys. J.* 109: 26–34.
  32. Byun, S., S. Son, D. Amodei, N. Cermak, J. Shaw, J.H. Kang, V.C. Hecht, M.M. Winslow, T. Jacks, P. Mallick, and S.R. Manalis. 2013. Characterizing deformability and surface friction of cancer cells. *Proc. Natl. Acad. Sci.* 110: 7580–7585.
  33. Shaw Bagnall, J., S. Byun, S. Begum, D.T. Miyamoto, V.C. Hecht, S. Maheswaran, S.L. Stott, M.

- Toner, R.O. Hynes, and S.R. Manalis. 2015. Deformability of Tumor Cells versus Blood Cells. *Sci. Rep.* 5: 18542.
34. Lange, J.R., C. Metzner, S. Richter, W. Schneider, M. Spermann, T. Kolb, G. Whyte, and B. Fabry. 2017. Unbiased High-Precision Cell Mechanical Measurements with Microconstrictions. *Biophys. J.* 112: 1472–1480.
35. Nyberg, K.D., M.B. Scott, S.L. Bruce, A.B. Gopinath, D. Bikos, Tt.G. Mason, J.W. Kim, H.S. Choi, and A.C. Rowat. 2016. The physical origins of transit time measurements for rapid, single cell mechanotyping. *Lab Chip.* 16: 3330–3339.
36. Chan, C.J., A.E. Ekpenyong, S. Golfier, W. Li, K.J. Chalut, O. Otto, J. Elgeti, J. Guck, and F. Lautenschläger. 2015. Myosin II Activity Softens Cells in Suspension. *Biophys. J.* 108: 1856–1869.
37. Cai, P., Y. Mizutani, M. Tsuchiya, J.M. Maloney, B. Fabry, K.J. Van Vliet, and T. Okajima. 2013. Quantifying Cell-to-Cell Variation in Power-Law Rheology. *Biophys. J.* 105: 1093–1102.
38. Duffy, D.C., J.C. McDonald, O.J.A. Schueller, and G.M. Whitesides. 1998. Rapid prototyping of microfluidic systems in poly(dimethylsiloxane). *Anal. Chem.* 70: 4974–4984.
39. Kumachev, A., E. Tumarkin, G.C. Walker, and E. Kumacheva. 2013. Characterization of the mechanical properties of microgels acting as cellular microenvironments. *Soft Matter.* 9: 2959.
40. Deming, W.E. 1966. Some theory of sampling. Courier Corporation.
41. Khismatullin, D.B., and G.A. Truskey. 2012. Leukocyte Rolling on P-Selectin: A Three-Dimensional Numerical Study of the Effect of Cytoplasmic Viscosity. *Biophys. J.* 102: 1757–1766.
42. Khismatullin, D.B., and G.A. Truskey. 2005. Three-dimensional numerical simulation of receptor-mediated leukocyte adhesion to surfaces: effects of cell deformability and viscoelasticity. *Phys. Fluids.* 17: 31505.

43. Bathe, M., A. Shirai, C.M. Doerschuk, and R.D. Kamm. 2002. Neutrophil transit times through pulmonary capillaries: the effects of capillary geometry and fMLP-stimulation. *Biophys. J.* 83: 1917–33.
44. Zhou, E.H., S.T. Quek, and C.T. Lim. 2010. Power-law rheology analysis of cells undergoing micropipette aspiration. *Biomech. Model. Mechanobiol.* 9: 563–572.
45. Puig-De-Morales, M., M. Grabulosa, J. Alcaraz, J. Mullol, G.N. Maksym, J.J. Fredberg, and D. Navajas. 2001. Measurement of cell microrheology by magnetic twisting cytometry with frequency domain demodulation. *J. Appl. Physiol.* 91: 1152–1159.
46. Tsai, M.A., R.E. Waugh, and P.C. Keng. 1996. Cell cycle-dependence of HL-60 cell deformability. *Biophys. J.* 70: 2023–9.
47. Rosenbluth, M.J., W.A. Lam, and D.A. Fletcher. 2006. Force microscopy of nonadherent cells: a comparison of leukemia cell deformability. *Biophys. J.* 90: 2994–3003.
48. Wang, G., K. Crawford, C. Turbyfield, W. Lam, A. Alexeev, and T. Sulchek. 2015. Microfluidic cellular enrichment and separation through differences in viscoelastic deformation. *Lab Chip.* 15: 532–540.
49. Fernandez, P., P.A. Pullarkat, and A. Ott. 2006. A master relation defines the nonlinear viscoelasticity of single fibroblasts. *Biophys. J.* 90: 3796–3805.
50. Marcy, Y., J. Prost, M.-F. Carlier, and C. Sykes. 2004. Forces generated during actin-based propulsion: a direct measurement by micromanipulation. *Proc. Natl. Acad. Sci.* 101: 5992–5997.
51. Bieling, P., T.-D. Li, J. Weichsel, R. McGorty, P. Jreij, B. Huang, D.A. Fletcher, and R.D. Mullins. 2016. Force Feedback Controls Motor Activity and Mechanical Properties of Self-Assembling Branched Actin Networks. *Cell.* 164: 115–127.
52. Icard-Arcizet, D., O. Cardoso, A. Richert, and S. Henon. 2008. Cell stiffening in response to external stress is correlated to actin recruitment. *Biophys. J.* 94: 2906–2913.



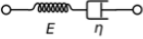
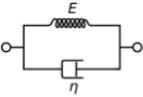
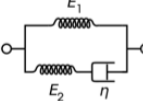
53. Hoffman, B.D., G. Massiera, K.M. Van Citters, and J.C. Crocker. 2006. The consensus mechanics of cultured mammalian cells. *Proc. Natl. Acad. Sci.* 103: 10259–10264.
54. Janmey, P.A., U. Euteneuer, P. Traub, and M. Schliwa. 1991. Viscoelastic properties of vimentin compared with other filamentous biopolymer networks. *J. Cell Biol.* 113: 155–160.
55. Gardel, M.L., F. Nakamura, J.H. Hartwig, J.C. Crocker, T.P. Stossel, and D.A. Weitz. 2006. Prestressed F-actin networks cross-linked by hinged filamins replicate mechanical properties of cells. *Proc. Natl. Acad. Sci.* 103: 1762–1767.
56. An, S.S., R.E. Laudadio, J. Lai, R.A. Rogers, and J.J. Fredberg. 2002. Stiffness changes in cultured airway smooth muscle cells. *Am. J. Physiol. Physiol.* 283: C792--C801.
57. Ting-Beall, H.P., a S. Lee, and R.M. Hochmuth. 1995. Effect of cytochalasin D on the mechanical properties and morphology of passive human neutrophils. *Ann. Biomed. Eng.* 23: 666–671.
58. Maniotis, A.J., C.S. Chen, and D.E. Ingber. 1997. Demonstration of mechanical connections between integrins, cytoskeletal filaments, and nucleoplasm that stabilize nuclear structure. *Proc. Natl. Acad. Sci. U. S. A.* 94: 849–54.
59. Gabriele, S., A.-M. Benoliel, P. Bongrand, and O. Théodoly. 2009. Microfluidic investigation reveals distinct roles for actin cytoskeleton and myosin II activity in capillary leukocyte trafficking. *Biophys. J.* 96: 4308–4318.
60. Mak, M., and D. Erickson. 2013. A serial micropipette microfluidic device with applications to cancer cell repeated deformation studies. *Integr. Biol. (Camb).* 5: 1374–84.
61. Martens, J.C., and M. Radmacher. 2008. Softening of the actin cytoskeleton by inhibition of myosin II. *Pflugers Arch. Eur. J. Physiol.* 456: 95–100.
62. Calzado-Martín, A., M. Encinar, J. Tamayo, M. Calleja, A. San Paulo, A. Calzado-Martin, M. Encinar, J. Tamayo, M. Calleja, and A. San Paulo. 2016. Effect of actin organization on the stiffness of living breast cancer cells revealed by peak-force modulation atomic force microscopy.

- ACS Nano. 10: 3365–3374.
63. Coceano, G., M.S. Yousafzai, W. Ma, F. Ndoye, L. Venturelli, I. Hussain, S. Bonin, J. Niemela, G. Scoles, D. Cojoc, and E. Ferrari. 2016. Investigation into local cell mechanics by atomic force microscopy mapping and optical tweezer vertical indentation. *Nanotechnology*. 27: 65102.
  64. Corbin, E.A., F. Kong, C.T. Lim, W.P. King, and R. Bashir. 2015. Biophysical properties of human breast cancer cells measured using silicon MEMS resonators and atomic force microscopy. *Lab Chip*. 15: 839–847.
  65. Omidvar, R., M. Tafazzoli-Shadpour, M.A. Shokrgozar, and M. Rostami. 2014. Atomic force microscope-based single cell force spectroscopy of breast cancer cell lines: an approach for evaluating cellular invasion. *J. Biomech*. 47: 3373–3379.
  66. Li, Q.S., G.Y.H. Lee, C.N. Ong, and C.T. Lim. 2008. AFM indentation study of breast cancer cells. *Biochem. Biophys. Res. Commun*. 374: 609–613.
  67. Rother, J., H. Noding, I. Mey, and A. Janshoff. 2014. Atomic force microscopy-based microrheology reveals significant differences in the viscoelastic response between malign and benign cell lines. *Open Biol*. 4: 140046.
  68. Gordon, L.A., K.T. Mulligan, H. Maxwell-Jones, M. Adams, R.A. Walker, and J.L. Jones. 2003. Breast cell invasive potential relates to the myoepithelial phenotype. *Int. J. cancer*. 106: 8–16.
  69. Swaminathan, V., K. Mythreye, E.T. O'Brien, A. Berchuck, G.C. Blobe, and R. Superfine. 2011. Mechanical stiffness grades metastatic potential in patient tumor cells and in cancer cell lines. *Cancer Res*. 71: 5075–5080.
  70. Evans, E., N. Mohandas, and A. Leung. 1984. Static and dynamic rigidities of normal and sickle erythrocytes. Major influence of cell hemoglobin concentration. *J. Clin. Invest*. 73: 477.
  71. Higgins, J.M., D.T. Eddington, S.N. Bhatia, and L. Mahadevan. 2007. Sickle cell vasoocclusion and rescue in a microfluidic device. *Proc. Natl. Acad. Sci*. 104: 20496–20500.

72. Rowat, A.C., D.E. Jaalouk, M. Zwerger, W.L. Ung, I. a Eydelnant, D.E. Olins, A.L. Olins, H. Herrmann, D. a Weitz, and J. Lammerding. 2013. Nuclear envelope composition determines the ability of neutrophil-type cells to passage through micron-scale constrictions. *J. Biol. Chem.* 288: 8610–8.
73. Elston, C.W., and I.O. Ellis. 1991. Pathological prognostic factors in breast cancer. I. The value of histological grade in breast cancer: experience from a large study with long-term follow-up. *Histopathology.* 19: 403–410.

## SUPPLEMENTAL INFORMATION

**Viscoelastic Models.** To measure the mechanical properties of cells from individual creep trajectories, we evaluate the quality of fit of standard viscoelastic models. The Maxwell, Kelvin-Voigt, and Standard Linear Solid models are represented by combinations of springs and dashpots. Similar to the springs and dashpot models, Power Law Rheology (PLR) provides a measure of elastic and viscous components of cells, whereby the power law exponent, or fluidity, reflects the viscous behavior (1). While we show in this study that PLR minimizes the residuals for HL-60 cells, certain cell types may be better described using other viscoelastic models (2).

Maxwell	$J_M(t) = k_1 + k_2 t$	
Kelvin-Voigt	$J_{KV}(t) = k_1(1 - e^{-k_2 t})$	
Standard Linear Solid	$J_{SLS}(t) = \frac{1}{k_1} e^{-k_2 k_3 t} + \frac{k_1 + k_2}{k_1 k_2} (1 - e^{-k_2 k_3 t})$	
Power Law Rheology	$J_{PLR}(t) = k_1 t^\beta$	

**Data analysis.** Analysis of q-DC data is performed using MATLAB (MathWorks, Natick, MA, USA). The video processing code is available on Github. Median residuals and corresponding confidence intervals are determined by bootstrapping 5000 iterations of theoretical fits to single cell data. Residual fits are determined using the least squares method. A value reported in the text as ‘X ± Y’ is the bootstrapped median, ‘X’, using bootstrapped resampling with the confidence interval, ‘2\*Y’. This bootstrapping method is also employed for determining  $\beta$  values, as well as the interquartile ranges. To compare the distributions of q-DC outputs between cell lines and drug treatments, we apply the pairwise, nonparametric Mann-Whitney U statistical test as most q-DC parameters are not normally distributed. Density scatter plots are created using the dscatter function (R. Henson, Mathworks File Exchange). We assess the strength of

correlations between q-DC outputs by determining Pearson's correlation coefficients for pairs of parameters.

## SUPPLEMENTAL TABLES

**S. Table 1. Viability of HL-60 cells after pharmacological perturbations.** Cell viability is determined using a Trypan blue assay.

Treatment	Viability
DMSO (Control)	$97.6 \pm 0.8\%$
Cytochalasin D	$86.4 \pm 2.7\%$
Blebbistatin	$84.5 \pm 1.1\%$
Jasplakinolide	$90.3 \pm 2.3\%$

**S. Table 2.  $E_a$  and  $\beta$  values from q-DC measurements.** The median  $E_a$  and  $\beta$  are determined by 1000 bootstrapped samples from the density-gated q-DC data. Error represents the corresponding confidence intervals.

Geometry w x h ( $\mu\text{m}^2$ )	$P_{\text{applied}}$ (kPa)	Cell Line	Treatment	$E_a$ (kPa)	$\sigma_{\text{IQR}_Ea}$	$\beta$	$\sigma_{\text{IQR}_\beta}$
5 x 5	28	HL-60	DMSO (Control)	$0.53 \pm 0.04$	$0.35 \pm 0.06$	$0.29 \pm 0.02$	$0.25 \pm 0.03$
5 x 5	28	HL-60	Cytochalasin D	$0.52 \pm 0.06$	$0.40 \pm 0.08$	$0.29 \pm 0.02$	$0.28 \pm 0.05$
5 x 5	28	HL-60	Blebbistatin	$0.39 \pm 0.05$	$0.46 \pm 0.08$	$0.34 \pm 0.03$	$0.33 \pm 0.04$
5 x 5	28	HL-60	Jasplakinolide	$0.55 \pm 0.07$	$0.30 \pm 0.06$	$0.27 \pm 0.03$	$0.27 \pm 0.06$
5 x 10	14	HL-60	-	$0.52 \pm 0.10$	$0.66 \pm 0.09$	$0.49 \pm 0.04$	$0.22 \pm 0.04$
5 x 10	34	HL-60	-	$0.99 \pm 0.08$	$0.49 \pm 0.06$	$0.46 \pm 0.02$	$0.19 \pm 0.03$
5 x 10	69	HL-60	-	$1.4 \pm 0.21$	$0.70 \pm 0.16$	$0.39 \pm 0.03$	$0.27 \pm 0.05$
9 x 10	28	HL-60	-	$0.15 \pm 0.03$	$0.86 \pm 0.18$	$0.50 \pm 0.04$	$0.28 \pm 0.05$
9 x 10	69	MCF-7	-	$2.1 \pm 0.14$	$0.41 \pm 0.09$	$0.28 \pm 0.01$	$0.19 \pm 0.03$
9 x 10	69	MDA-MB-231	-	$0.80 \pm 0.19$	$0.84 \pm 0.10$	$0.40 \pm 0.03$	$0.33 \pm 0.04$

**S. Table 3.  $E$  and  $\beta$  values from literature.**

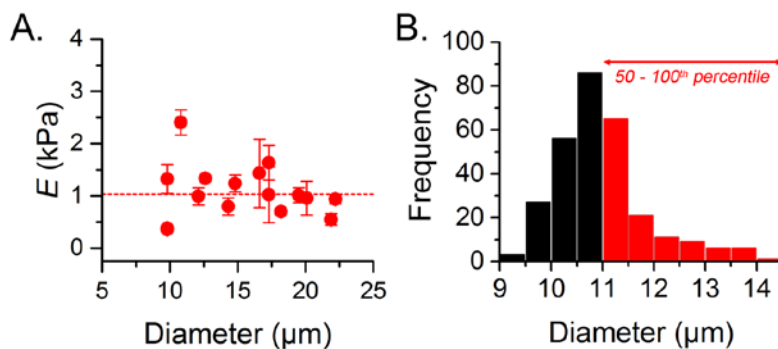
Cell Line	Method	Elastic Modulus $E$	Fluidity $\beta$	Ref.
HL-60	AFM	$855 \pm 670$ Pa	-	(3)
	OS	$34.5 \pm 36.5$ Pa	$0.65 \pm 0.5$	(2)
		$23.8 \pm 7.4$ Pa	$0.82 \pm 0.2$	(4)
MCF-7	AFM	$0.285 \pm 0.127$ kPa	-	(5)
		$1.04 \pm 0.27$ kPa	-	(6)
		$50.2 \pm 38.5$ kPa to $87.3 \pm 47.8$ kPa	-	(7)
		$0.5 \pm 0.1$ to $28 \pm 12$ kPa	-	(8)
		$0.420 - 1.210$ kPa	-	(9)
		$0.25 \pm 0.02$ kPa	$0.25 \pm 0.02$	(10)
MDA-MB-231	AFM	$0.277 \pm 0.063$ kPa	-	(5)
		$0.63 \pm 0.21$ kPa	-	(6)
		$28.7 \pm 26.1$ kPa to $55.6 \pm 20.1$ kPa	-	(7)
		$0.3 \pm 0.1$ kPa to $25 \pm 13$ kPa	-	(8)
		$0.69 \pm 0.06$ kPa	$0.22 \pm 0.01$	(10)
		$0.20 - 0.30$ kPa to $0.19-0.23$ kPa	-	(11)
	DC	$0.58$ kPa	$0.27$	(12)

**S. Table 4. Calibration for applied stress in varying device geometries.** The calibration factors are determined by the threshold pressure method. Utilizing agarose calibration particles, we are able to determine the applied stress at the constriction region.

Geometry	$A$	$P_{applied}$ (kPa)	$\sigma$ (Pa)
$w \times h$ ( $\mu\text{m}^2$ )			

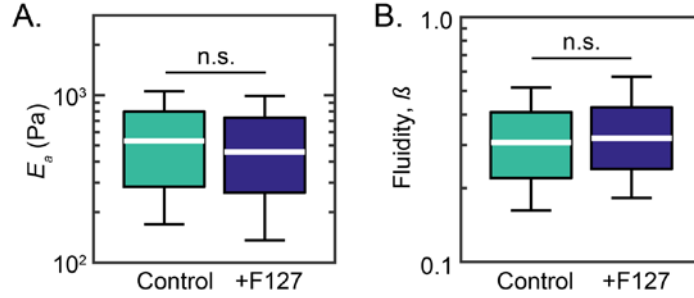
5x5	$0.021 \pm 0.002$	28	$570 \pm 50$
5x10	$0.070 \pm 0.018$	14	$960 \pm 250$
		34	$2400 \pm 630$
		69	$4800 \pm 1300$
9x10	$0.032 \pm 0.002$	34	$1100 \pm 60$

## SUPPLEMENTAL FIGURES

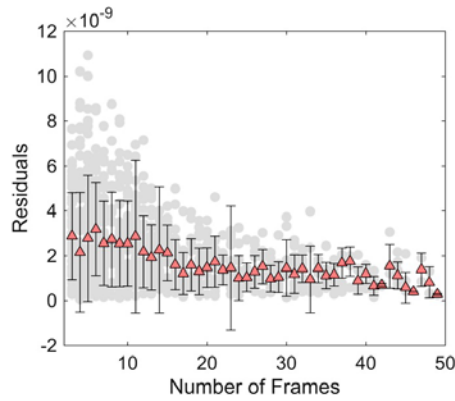


**S. Fig. 1. Agarose calibration particles exhibit size-independent elastic moduli.** (A) Elastic modulus of particles composed of 1.5% (w/w) agarose as a function of particle diameter as measured by AFM. Data represents the mean  $\pm$  standard deviation for each particle probed 2-5 times. The red dotted line illustrates the average elastic modulus. Data collected over two independent experiments ( $N = 15$ ). (B) Distribution of diameters for particles composed of 1.5% (w/w) agarose as they transit through  $5 \mu\text{m} \times 5 \mu\text{m}$  constrictions. The 50<sup>th</sup> – 100<sup>th</sup> percentile of sizes are considered to determine the median maximum strain at the threshold pressure conditions as depicted by the red bars ( $N = 220$ ).

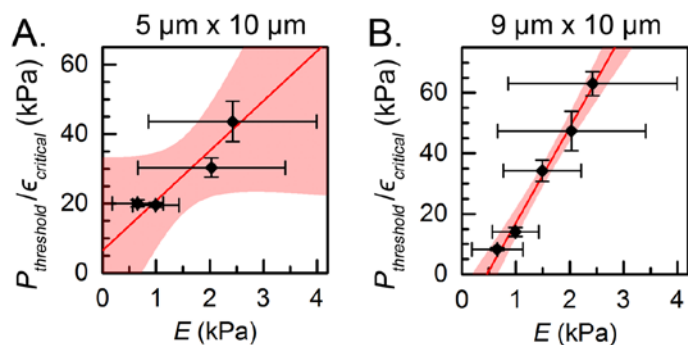




**S. Fig. 2. Effects of surfactant on cell mechanotyping.** Apparent elastic modulus  $E_a$  and fluidity  $\beta$  values of HL-60 cells treated with pluronic F-127 during transit through microfluidic constrictions. White lines represent the median  $E_a$  and  $\beta$ . Boxes represent the interquartile ranges and whiskers represent the 10<sup>th</sup>–90<sup>th</sup> percentiles ( $N > 500$ ). The Mann-Whitney U test is used to evaluate statistical significance. n.s. denotes  $p \geq 0.05$ .

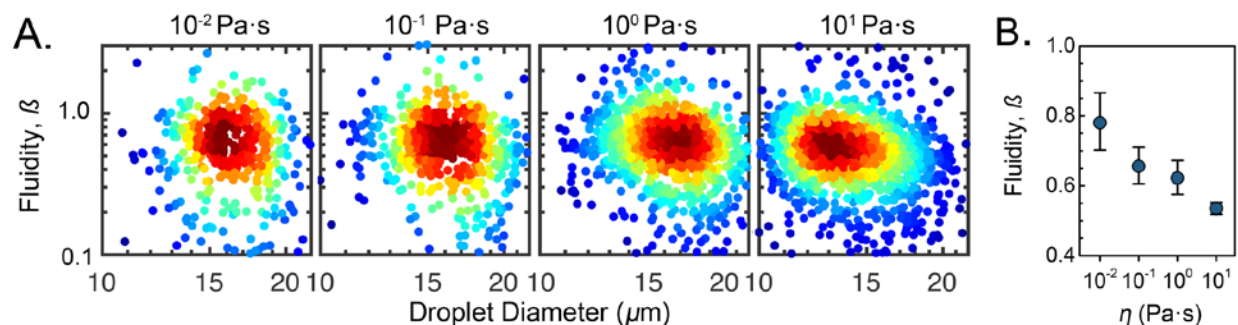


**S. Fig. 3. Residuals of PLR creep fit depends on frame number.** Scatter plot of the residuals per frame for HL-60 cells. The gray dots represent the residuals for individual cells. The orange triangles illustrate the median residual for each number of frames. The error bars represent the interquartile range.  $N = 550$ . There exists a trade-off between the quality of PLR fitting and the dynamic range of q-DC. By minimizing the required number of frames for creep trajectories, the dynamic range extends to sample longer deformation timescales within a population of cells.

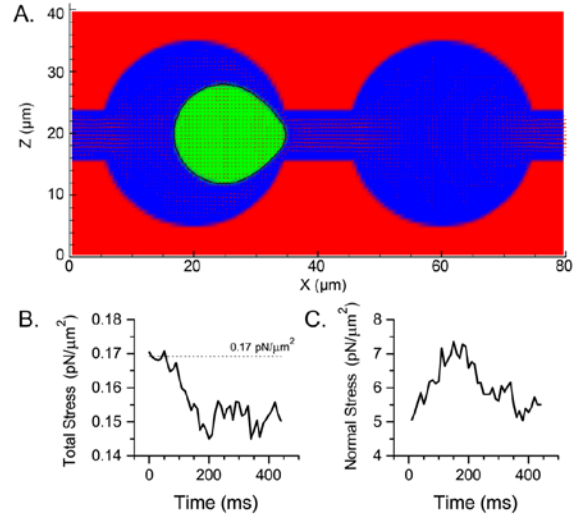


**S. Fig. 4. Threshold transit conditions for characterizing applied stress in microfluidic constrictions.**

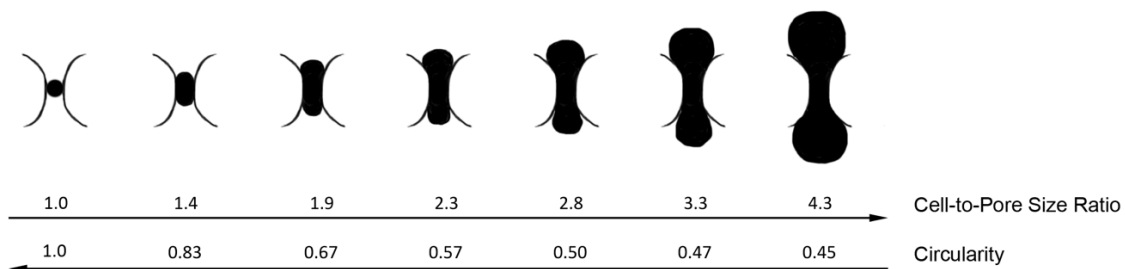
Threshold applied pressures in the (A)  $5\ \mu\text{m} \times 10\ \mu\text{m}$  and (B)  $9\ \mu\text{m} \times 10\ \mu\text{m}$  microfluidic device geometries for calibration particles with a range of elastic moduli,  $0.6 - 2.4\ \text{kPa}$ . X-error bars represent the standard deviation of the elastic modulus as determined by AFM. Y-error bars represent the standard deviation of the pressure-to-particle strain ratio. The red line is the linear fit; the red shaded region illustrates the 95% confidence interval of the linear fit. The inverse of the slope characterizes the applied pressure-to-stress scaling factor.  $N > 650$  for strain measurements at each threshold condition.



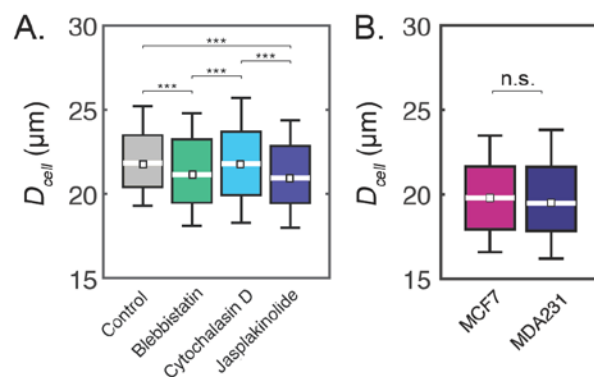
**S. Fig. 5. Power law exponent for oil particles.** (A) Validation of power law rheology using oil-in-water emulsion droplets made with silicone oils of varying viscosities. Power law exponents,  $\beta$ , for oil droplets calculated by the least-squares fit of deformation trajectories with power law rheology model. Density scatter plots represent  $\beta$  as a function of droplet size. Each dot represents a single cell. Color represents the density of points. White diamonds show the highest density of points.  $N > 500$  oil droplets. (B) Bootstrapped median values of  $\beta$  for droplets of silicone oils. Error bars denote the bootstrapped confidence intervals.



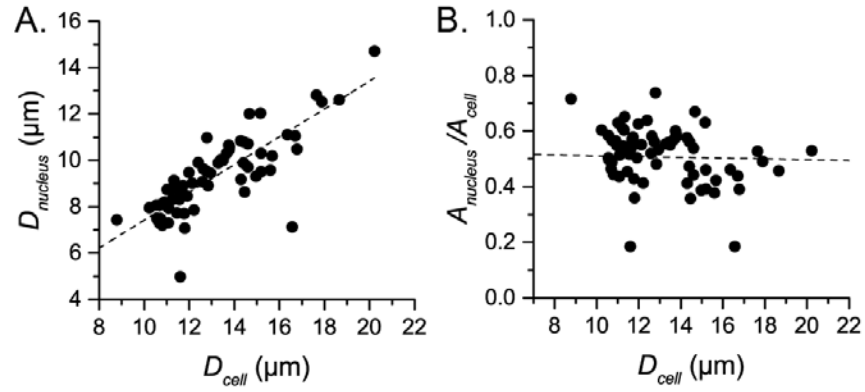
**S. Fig. 6. Numerical simulations of single cells deforming through a constriction.** (A) Simulation of a cell deforming through a micron-scale constriction. Shown here is a representative cell with a diameter of  $16.3\ \mu\text{m}$  transiting through a constriction with a width of  $8.1\ \mu\text{m}$ ; the cell-to-pore size ratio is 2. The red arrows represent the flow vector field. (B-C) The total hydrodynamic stress (B) and normal stress (C) acting on a cell as it transits through a constriction; cell-to-pore size ratio is 1. When the cell is transiently occluding the pore, there are positive normal forces that deform the cell. As the transiting cell continually deforms through the constriction, there is also a drop in hydrodynamic force: according to Stokes' law, the hydrodynamic force is proportional to the cell velocity and thus a decrease in the cell velocity leads to a decrease in the hydrodynamic force. The black dotted line represents the baseline hydrodynamic stress acting on the cell before it reaches the constriction.



**S. Fig. 7. Shape library.** Graphic representation of shape changes in cells with a range of sizes during transit through a microfluidic constriction. Cell-to-pore size ratio is determined by the ratio between the unconstrained cell diameter and the width of the constriction, where the unconstrained cell diameter is calculated as the diameter of a perfect circle with an area of the cell's projected area.



**S. Fig. 8. Size distributions of HL-60 cells treated with cytoskeletal-perturbing drugs and breast cancer cell lines.** Box plots represent the cell diameters as determined by brightfield imaging during q-DC measurements. White lines represent the median, boxes represent the interquartile ranges, whiskers represent the 10<sup>th</sup> and 90<sup>th</sup> percentiles, and white squares represent the bootstrapped median.



**S. Fig. 9. Cell and nuclear size in HL-60 cells.** Scatter plots of (A) nuclear diameter versus cell diameter and (B) nuclear-to-cell area ratio versus cell diameter for HL-60 cells. Cells are stained with Hoechst and Calcein AM; thereafter, samples are imaged via confocal microscopy. Each point represents data for a single cell. Black dotted line shows linear fit to the data.

## SUPPLEMENTAL BIBLIOGRAPHY

1. Fabry, B., G.N. Maksym, J.P. Butler, M. Glogauer, D. Navajas, and J.J. Fredberg. 2001. Scaling the microrheology of living cells. *Phys. Rev. Lett.* 87: 148102.
2. Ekpenyong, A.E., G. Whyte, K. Chalut, S. Pagliara, F. Lautenschläger, C. Fiddler, S. Paschke, U.F. Keyser, E.R. Chilvers, and J. Guck. 2012. Viscoelastic Properties of Differentiating Blood Cells Are Fate- and Function-Dependent. *PLoS One.* 7.
3. Rosenbluth, M.J., W.A. Lam, and D.A. Fletcher. 2006. Force microscopy of nonadherent cells: a comparison of leukemia cell deformability. *Biophys. J.* 90: 2994–3003.
4. Chan, C.J., A.E. Ekpenyong, S. Golfier, W. Li, K.J. Chalut, O. Otto, J. Elgeti, J. Guck, and F. Lautenschläger. 2015. Myosin II Activity Softens Cells in Suspension. *Biophys. J.* 108: 1856–1869.
5. Corbin, E.A., F. Kong, C.T. Lim, W.P. King, and R. Bashir. 2015. Biophysical properties of human breast cancer cells measured using silicon MEMS resonators and atomic force microscopy. *Lab Chip.* 15: 839–847.
6. Omidvar, R., M. Tafazzoli-Shadpour, M.A. Shokrgozar, and M. Rostami. 2014. Atomic force microscope-based single cell force spectroscopy of breast cancer cell lines: an approach for evaluating cellular invasion. *J. Biomech.* 47: 3373–3379.
7. Coceano, G., M.S. Yousafzai, W. Ma, F. Ndoye, L. Venturelli, I. Hussain, S. Bonin, J. Niemela, G. Scoles, D. Cojoc, and E. Ferrari. 2016. Investigation into local cell mechanics by atomic force microscopy mapping and optical tweezer vertical indentation. *Nanotechnology.* 27: 65102.
8. Calzado-Martín, A., M. Encinar, J. Tamayo, M. Calleja, A. San Paulo, A. Calzado-Martín, M. Encinar, J. Tamayo, M. Calleja, and A. San Paulo. 2016. Effect of actin organization on the stiffness of living breast cancer cells revealed by peak-force modulation atomic force microscopy. *ACS Nano.* 10: 3365–3374.
9. Li, Q.S., G.Y.H. Lee, C.N. Ong, and C.T. Lim. 2008. AFM indentation study of breast cancer cells. *Biochem. Biophys. Res. Commun.* 374: 609–613.

10. Rother, J., H. Noding, I. Mey, and A. Janshoff. 2014. Atomic force microscopy-based microrheology reveals significant differences in the viscoelastic response between malignant and benign cell lines. *Open Biol.* 4: 140046.
11. Agus, D.B., J.F. Alexander, W. Arap, S. Ashili, J.E. Aslan, R.H. Austin, V. Backman, K.J. Bethel, R. Bonneau, W.-C. Chen, C. Chen-Tanyolac, N.C. Choi, S.A. Curley, M. Dallas, D. Damania, P.C.W. Davies, P. Decuzzi, L. Dickinson, L. Estevez-Salmeron, V. Estrella, M. Ferrari, C. Fischbach, J. Foo, S.I. Fraley, C. Frantz, A. Fuhrmann, P. Gascard, R.A. Gatenby, Y. Geng, S. Gerecht, R.J. Gillies, B. Godin, W.M. Grady, A. Greenfield, C. Hemphill, B.L. Hempstead, A. Hielscher, W.D. Hillis, E.C. Holland, A. Ibrahim-Hashim, T. Jacks, R.H. Johnson, A. Joo, J.E. Katz, L. Kelbaskas, C. Kesselman, M.R. King, K. Konstantopoulos, C.M. Kraning-Rush, P. Kuhn, K. Kung, B. Kwee, J.N. Lakins, G. Lambert, D. Liao, J.D. Licht, J.T. Liphardt, L. Liu, M.C. Lloyd, A. Lyubimova, P. Mallick, J. Marko, O.J.T. McCarty, D.R. Meldrum, F. Michor, S.M. Mumenthaler, V. Nandakumar, T. V O'Halloran, S. Oh, R. Pasqualini, M.J. Paszek, K.G. Philips, C.S. Poultney, K. Rana, C.A. Reinhart-King, R. Ros, G.L. Semenza, P. Senechal, M.L. Shuler, S. Srinivasan, J.R. Staunton, Y. Stypula, H. Subramanian, T.D. Tlsty, G.W. Tormoen, Y. Tseng, A. van Oudenaarden, S.S. Verbridge, J.C. Wan, V.M. Weaver, J. Widom, C. Will, D. Wirtz, J. Wojtkowiak, and P.-H. Wu. 2013. A physical sciences network characterization of non-tumorigenic and metastatic cells. *Sci. Rep.* 3: 1449.
12. Lange, J.R., J. Steinwachs, T. Kolb, L.A. Lautscham, I. Harder, G. Whyte, and B. Fabry. 2015. Microconstriction Arrays for High-Throughput Quantitative Measurements of Cell Mechanical Properties. *Biophys. J.* 109: 26–34.

## CHAPTER 3

### *Label-Free Prediction of Cancer Cell Invasion by Single-Cell Physical Phenotyping*

#### **Abstract**

The physical properties of cells, such as cell deformability, are promising label-free biomarkers for cancer diagnosis and prognosis. Here we determine the physical phenotypes that best distinguish human cancer cell lines, and their relationship to cell invasion. We use the high throughput, single-cell microfluidic method, quantitative deformability cytometry (q-DC), to measure six physical phenotypes including elastic modulus, cell fluidity, transit time, creep time, cell size, and maximum strain at rates of  $10^2$  cells/s. By training a simple k-nearest neighbor machine learning algorithm, we demonstrate that multiparameter analysis of physical phenotypes enhances the accuracy of classifying pancreatic cancer cell lines compared to single parameters alone. We also discover a set of four physical phenotypes that predict invasion; using these four parameters, we generate the physical phenotype model of invasion by training a machine learning algorithm with experimental data from a set of human ovarian cancer (HEYA8) cells that overexpress a panel of tumor suppressor microRNAs. We validate the model using breast and ovarian human cancer cell lines with both genetic and pharmacologic perturbations. Our results reveal that the physical phenotype model correctly predicts the invasion of five cancer cell samples. We also identify a context where our model does not accurately predict invasion, which incites deeper investigation into the role of additional physical phenotypes in cancer cell invasion. Taken together, our results highlight how physical phenotyping of single cells coupled with machine learning provide a complementary biomarker to predict the invasion of cancer cells.



## Introduction

Predicting disease and treatment outcomes based on single cell phenotypes is critical in medicine from cancer diagnosis to stem cell therapies. In clinical oncology and immunology, single cell analysis of protein markers and DNA content using flow cytometry is used for diagnosis, prognosis, and monitoring patient response to therapy (1). Yet pathological and physiological changes can also manifest as altered cell physical phenotypes, including cell and nuclear size, stiffness, and viscosity, which are convenient, label-free biomarkers. For example, grading of tumor biopsies based on nuclear morphology is widely used for cancer prognosis (2–4). The mechanical phenotype, or ‘mechanotype’, of cancer cells also shows promise as a prognostic biomarker, since more invasive cancer cells have altered mechanotype compared to less invasive cells (5–16). While cell mechanotype impacts the ability of cells to deform through narrow gaps and can thus have consequences for functional behaviors, such as invasion, the relationship between invasion and cell stiffness remains unclear: many studies show that more invasive cancer cells tend to be more compliant than less invasive or benign cells (5–11); however, there are also contexts where more invasive cells are found to be stiffer (12–16). These contrasting results motivate deeper investigation into additional physical phenotypes that may collectively be stronger predictors of invasion.

Microfluidic methods are especially valuable for physical phenotyping, as they enable rapid measurements of single cells. One such method is transit-based deformability cytometry, which probes physiologically-relevant deformations of cells through narrow gaps across varying deformation time and length scales (10, 17–20). While transit time  $T_T$  is a relative measurement, this parameter can distinguish sets of two to three cancer cell lines (10, 19). However, a population of cells typically exhibits  $T_T$  that span several orders of magnitude (21); together with the inherent variability of  $T_T$  measurements, it is thus challenging to robustly compare cell samples, scale up measurements to larger panels of cells, and achieve successful translation to clinical applications. We recently presented the quantitative deformability cytometry (q-DC) method, which uses calibration particles and power law rheology to obtain calibrated single-cell measurements of elastic modulus  $E$  and fluidity  $\beta$  (22). Measuring additional

physical phenotypes, such as  $E$  and  $\beta$ , could achieve more robust classification of cells using transit-based deformability cytometry.

Studies of cell physical phenotypes using atomic force microscopy (AFM)(23–27), cross-slot deformability cytometry (28), and optofluidic time-stretch microscopy (29) demonstrate that multiple physical phenotypes, such as cell morphology, stiffness, and relaxation time, can enhance the accuracy of cell classification. Multiparameter analysis of physical phenotypes can also result in clinical benefits; biophysical signatures of mesenchymal stromal cells are predictive of their regenerative capability as indicated by *in vivo* ectopic bone formation in mouse models (30). However, it is unclear which additional parameters can enhance the use of transit-based deformability cytometry to classify cancer cells. More broadly, identifying the physical phenotypes of cancer cells that are predictors of invasion would provide a set of valuable complementary biomarkers for metastatic potential.

Here we investigate the relationship between physical phenotypes and invasion of human cancer cell lines. We perform multiparameter analyses of six physical phenotypes across nineteen cancer cell samples. To measure the physical phenotypes of single cells, we use quantitative deformability cytometry (q-DC) to obtain calibrated measurements of elastic modulus  $E$  and cell fluidity  $\beta$ , as well as transit time  $T_T$ , creep time  $T_C$ , cell size  $D_{cell}$ , and maximum strain  $\epsilon_{max}$ , at rates of  $10^2$  cells/s (22). We show that multiparameter analysis of these physical phenotypes can enhance classification of cancer cell lines. From our analysis across well-established pancreatic cancer cell lines as well as ovarian cancer cells that overexpress tumor-suppressor microRNAs, we build the predictive physical phenotyping model for invasion, which we validate using both genetic and pharmacologic perturbations of cancer cells. Our results demonstrate the predictive power of physical phenotypes and machine learning to generate complementary biomarkers for invasion.

## Materials and Methods

**Cell culture.** HPDE cells are obtained from Dr. Ming-Sound Tsao (University Health Network-Princess Margaret Hospital, Canada and University of Toronto, Canada). HPDE cells are cultured in Keratinocyte-SFM medium supplemented with prequalified human recombinant Epidermal Growth Factor 1-53, Bovine Pituitary Extract, and 1% penicillin-streptomycin. The human pancreatic ductal adenocarcinoma (PDAC) cell lines (AsPC-1, Hs766T, MIA PaCa-2, and PANC-1) are from the American Type Culture Collection (ATCC). AsPC-1, Hs766T, MIA PaCa-2 and PANC-1 cells are grown in high glucose, L-glutamine without sodium pyruvate DMEM medium with 10% heat-inactivated fetal bovine serum and 1% penicillin-streptomycin. Fetal bovine serum and penicillin-streptomycin are from Gemini BioProducts, West Sacramento, CA. All cell media and additional media supplements are from Thermo Fisher Scientific Inc., Canoga Park, CA. Human ovarian cancer (HEYA8) cells, microRNA mimics, mock, and scrambled (SCR) negative controls are from Dr. Preethi Gunaratne (University of Houston, USA)(31, 32). HEYA8 cells are cultured in RPMI 1640 medium supplemented with 10% fetal bovine serum and 1% of penicillin-streptomycin. Cells are transiently transfected at 24 nM using Lipofectamine 2000 in serum-free OptiMEM medium, followed by the addition of 10% fetal bovine serum after 4 hours in serum-free conditions. All assays are performed 72 hours post transfection. Human ovarian cancer (OVCA433-GFP, OVCA433-Snail) cells are from Dr. Ruprecht Wiedemeyer (Cedars-Sinai Medical Center, USA) (33). OVCA433 cells are cultured in DMEM medium with L-Glutamine, Glucose, and Sodium Pyruvate. Medium is supplemented with 10% fetal bovine serum, 1% Anti-anti, and 2.5 µg/ml Plasmocin Prophylactic with 5 µg/ml blasticidin S HCl.

A highly metastatic variant of the MDA-MB-231 cells (MDA-MB-231-HM, gift from Dr. Zhou Ou, Fudan University Shanghai Cancer Center, China)(34) is cultivated in DMEM medium with L-Glutamine, Glucose, and Sodium Pyruvate, supplemented with 10% fetal bovine serum and 1% penicillin-streptomycin. The agonist (isoproterenol) for the  $\beta$ -adrenergic receptor is from Sigma-Aldrich (St. Louis, MO). Cells are treated for 24 hours prior to measurements.

All cells are cultured at 37°C with 5% CO<sub>2</sub>. Cell line authentication is performed using short tandem repeat (STR) profiling (Laragen Inc., Culver City, CA, USA and CellBank Australia, Westmead, NSW, Australia). Prior to deformability measurements, 0.01% (v/v) Pluronic F-127 surfactant (Sigma-Aldrich, St. Louis, MO, USA) is added to the cell suspension to reduce cell adhesion to the PDMS walls. While F-127 treatment does not significantly affect *E* values of suspended cells (22), we observe a significant decrease in cell-to-PDMS adhesion in some cell types such as HPDE cells (21).

**Microfluidic chip fabrication.** Negative photomasks are designed in AutoCAD (Autodesk, Inc., San Rafael, CA) and printed on chrome by the Nanolab at UCLA. The design of the q-DC devices is described previously (21). Silicone masters are fabricated using soft photolithography techniques (35). Polydimethylsiloxane (PDMS) (Sylgard Dow Corning, Midland, MI, USA) with a 10:1 w/w ratio of base and curing agent is poured onto the master wafer and placed under vacuum to degas for 1 hour. To cure the PDMS, the wafer and PDMS mixture is placed in a 65°C oven for 2 hours. Inlets and outlets are created using a biopsy punch with a 0.75 mm bore size (Sigma-Aldrich, St. Louis, MO, USA). The devices are then bonded to coverglass (#1.5 thickness) by plasma and baked at 80°C for 5 minutes to facilitate bonding. To ensure consistent device surface properties, q-DC experiments are performed 24 h after plasma treatment (21).

**q-DC microfluidic experiment.** To measure the physical properties of single cells, we use the q-DC method as previously reported (22). In brief, q-DC microfluidic devices are mounted onto an inverted microscope (Zeiss Observer, Zeiss, Oberkochen, Germany) that is equipped with a 20×/0.40 NA objective. A constant air pressure (69 kPa) drives cell suspensions to flow through the channels. As cells deform through microfluidic constrictions with 10 μm height and 9 μm width, a CMOS camera (MicroRNacoEx4, Vision Research, Wayne, NJ, USA) is used to capture brightfield images at rates of 600 to 2000 frames per second. For cell suspensions with a density of 2 x 10<sup>6</sup> cells/mL that are driven by an applied pressure of 69 kPa (10 psi), single cell measurements can be acquired at rates of 10<sup>2</sup> cells/s. While the timescale of the initial cell deformation into microfluidic constrictions is largely determined by

cell deformability (32–34), 0.01% (w/v) pluronic F-127 surfactant (Sigma-Aldrich, St. Louis, MO, USA) is added to the cell media to minimize cell-surface interactions.

**Physical property measurements using q-DC.** To conduct multiparameter analysis of cell physical properties, the displacement and shape of single cells are tracked using a MATLAB code (Mathworks, Natick, MA, USA; code available online on GitHub) (22). This enables us to acquire cell size  $D_{cell}$ , maximum strain  $\epsilon_{max}$ , creep time  $T_C$ , and transit time  $T_T$ . To extract elastic modulus  $E$  and cell fluidity  $\beta$ , the applied stress during cell deformation is measured using agarose calibration particles with well-characterized Young's moduli for the  $9 \times 10 \mu\text{m}^2$  and  $7 \times 10 \mu\text{m}^2$  device geometries (22). By tracking the change in cell strain during deformation and fitting power law rheology to the creep function, we can extract elastic modulus and cell fluidity. The creep function,  $J(t)$ , is defined as the ratio between the strain and applied stress:

$$J(t) = \frac{\epsilon(t)}{\bar{\sigma}}, \quad \text{Eq. 1}$$

where  $\epsilon(t)$  is the strain and  $\bar{\sigma}$  is the time-averaged stress. Here, strain is measured as  $\epsilon(t) = \frac{C_o - C(t)}{C_o}$ , where  $C$  is the circularity,  $C(t) = \frac{4\pi A(t)}{P(t)^2}$ . We set the initial circularity value as  $C_o = 1$ , which is the value of a perfect circle, since the cells exhibit a circularity close to 1 prior to deformation through the constrictions. Using least squares residual fitting, we fit the power law model to the creep trajectories of individual cells:

$$J(t) = \frac{\epsilon(t)}{0.032 P_{applied}}, \quad \text{Eq. 2}$$

where  $E$  is the elastic modulus when  $t = \tau$ ;  $\tau$  is the characteristic timescale, set to 1 s; and  $\beta$  is the power law exponent, which represents cell fluidity. For purely elastic materials,  $\beta = 0$ ; for purely viscous materials,  $\beta = 1$ . As elastic modulus  $E$ , cell fluidity  $\beta$ , creep time  $T_C$ , and transit time  $T_T$  depend on cell size, we analyze only cells that have  $D_{cell}$  that is the population median  $\pm 1 \mu\text{m}$ .

**Classification using q-DC.** To evaluate the power of q-DC parameters to classify cells, we perform supervised machine learning using the k-nearest neighbor (k-NN) algorithm. The k-NN classification algorithm assigns the output class as the most common class of an integer, k, closest neighbors; in this study we use  $k = 10$ . The distance is defined as the Euclidian distance between input feature vectors—in our case the sets of qDC predictors. We supply a known set of input data by generating 500 randomly-sampled subsets with replacement, containing 100 single cells, for each cancer cell line and measuring the medians of the corresponding q-DC parameters for each sample set, such as median cell size and maximum strain. Using the summary statistics dataset in custom Python code, we train classification models based on the k-NN algorithm for sets of q-DC predictors. We execute the training with 5-fold cross validation, which enables us to determine the classification accuracy. Here, the classification accuracy is defined as the percentage of correct predictions on each observation in the validation sets.

**Physical phenotype model of invasion using q-DC.** The physical phenotype model of invasion is determined by multiple linear regression in MATLAB (Mathworks, Natick, MA, USA). To evaluate linear regression error, we utilize the single-cell q-DC data to train linear regression models using 1000 bootstrapped samples of single-cell physical phenotypes. Each bootstrapped sample generates a linear combination of physical phenotypes to predict invasion and their associated coefficients that minimize residuals. The physical phenotype model is determined by the median coefficient for each parameter. The correlation coefficient between predicted invasion and measured invasion is determined as the average correlation coefficient. Similar to the training analysis, we predict invasion using the physical phenotype model with 1000 bootstrapped samples of the q-DC data of single-cells; this enables us to determine the average predicted invasion.

## **Results**

**Multiparameter physical phenotyping by q-DC.** To rapidly measure the physical phenotypes of single cells, we use transit-based deformability cytometry; this microfluidic device consists of an array of

branching channels (18, 20, 21, 36, 37), which lead to micron-scale constrictions. The timescale for cells to transit through the micron-scale constrictions of these channels provides a simple measure of cell deformability (Fig. 1A,B): stiffer cells tend to have longer transit times ( $T_T$ ) compared to more compliant cells (38). We recently developed quantitative deformability cytometry (q-DC), which enables calibrated single-cell measurements of physical phenotypes including elastic modulus  $E$  and fluidity  $\beta$  that are extracted using power law rheology. Using q-DC, we also obtain cell size  $D_{cell}$ , from the diameter of the unconstrained cell prior to deformation; maximum strain  $\epsilon_{max}$ , based on the minimum circularity that occurs as the cell deforms through the constriction; and creep time  $T_C$ , which is the time required for a cell to reach maximum strain (Fig 1A). While q-DC enables measurements of physical phenotypes in addition to  $T_T$ , it is not clear how this added information benefits cell classification and prediction of invasion.

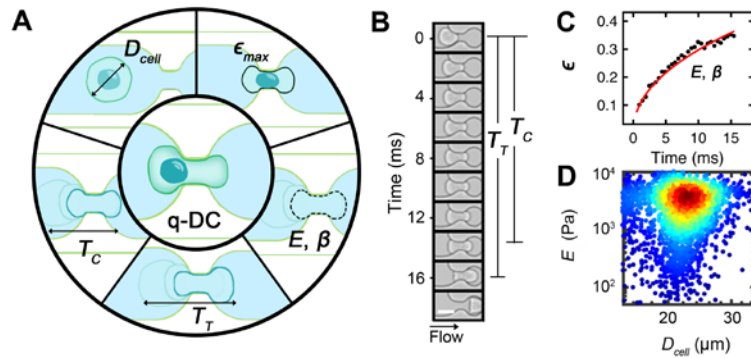


**Fig 1. Overview of cell physical phenotyping by quantitative deformability cytometry (q-DC).** (A) Overview of physical phenotypes measured by q-DC: elastic modulus  $E$ , cell fluidity  $\beta$ , transit time  $T_T$ , creep time  $T_C$ , cell size  $D_{cell}$ , and maximum strain  $\epsilon_{max}$ . (B) A representative cell deforming through a microfluidic channel of the q-DC device. Creep time  $T_C$  is the time required for a cell to reach maximum strain  $\epsilon_{max}$ ; transit time  $T_T$  is the time required for the cell to transit through the constriction. Scale bar, 20  $\mu\text{m}$ . (C) Black dots represent the strain of the single cell shown in panel B as a function of time. Red solid line represents power law fit to single-cell strain trajectory over the creep timescale,  $T_C$ . Using power law rheology, we extract elastic modulus,  $E$ , and fluidity exponent,  $\beta$ . (D) Representative scatter plot of  $E$  and  $D_{cell}$  for human pancreatic ductal

epithelial (HPDE) cells. Each dot represents a single cell and color denotes number density. Shown here are a total of  $N = 3231$  cells.

**Pairwise correlation analysis of q-DC parameters.** To assess the value of multiple biophysical parameters for classification of different cell types, we use q-DC to measure physical phenotypes of human pancreatic ductal adenocarcinoma (PDAC) cell lines that are derived from primary tumors (PANC-1 and MIA PaCa-2), and secondary sites (AsPC-1 and Hs766T), as well as a nontransformed human ductal pancreatic epithelial (HPDE) control cell line. These cell lines exhibit distinct differences in invasion (12), and therefore provide a model system for testing q-DC classification of cells.

To identify which physical phenotypes provide unique information and which ones are statistically redundant for classifying populations of single cells, we first evaluate the correlation strength between pairs of the six q-DC outputs,  $E$ ,  $\beta$ ,  $T_T$ ,  $T_C$ ,  $D_{cell}$ , and  $\epsilon_{max}$  (Fig. 2A, S. Table. 1). Spearman's rank correlation coefficients of -1 and +1 reflect pairs of parameters that are highly correlated and statistically dependent on each other. By contrast, correlation coefficients with a low absolute value indicate pairs of parameters that are weakly correlated with each other; each parameter from a weakly correlated pair will more likely provide unique information, as they are more statistically independent from each other.

Analysis of the Spearman's correlation coefficients reveals that  $T_T$  and  $T_c$  are highly correlated ( $r = 0.94$ ;  $p \ll 0.001$ ) (Fig. 2A, S. Table. 1); this is expected as the first stage of cell transit through a pore requires cell creep. We also find that  $\beta$  and  $E$  are strongly correlated ( $r = -0.88$ ;  $p \ll 0.001$ ); this scaling of  $E$  and  $\beta$  is consistent with the behavior of soft glassy materials (17, 39). All other pairwise comparisons between parameters, such as  $D_{cell}$  to  $\epsilon_{max}$ ,  $T_T$ ,  $E$ , are weakly correlated with  $-0.14 < r < 0.41$  (S. Table 1), suggesting that combinations of these parameters could provide unique information for characterizing cell lines.

**Multiparameter analysis for classification of pancreatic cells.** To assess the value of q-DC data sets in classifying PDAC cell lines, we use the simple yet powerful k-nearest neighbors (k-NN) algorithm to



classify cell lines based on physical phenotypes. In the k-NN method, training data establishes a multidimensional feature space, where q-DC parameters define each dimension; cells are then classified based on the identity of their k nearest neighbors in the pre-established feature space. To evaluate how the number of predictors and combinations thereof affect classification accuracy, we first assess single physical phenotypes. We find that single parameters alone offer low classification accuracy of cell lines:  $T_T$  yields 65% accuracy in predicting the correct cell line from our panel of PDAC cell lines,  $E$  yields 59% accuracy, and  $D_{cell}$  gives 52% (Fig. 2B).

The inclusion of additional physical phenotypes can significantly enhance classification accuracy:  $\{E, T_T\}$  provide a model accuracy of 87% and with  $\{T_T, D_{cell}\}$ , the model accuracy increases to 91% (Fig. 2B, S. Fig. 1). Other combinations of two parameters yield accuracies ranging from 69% to 89% (S. Fig. 1). Including an additional third parameter further improves accuracy, but with smaller gains: both  $\{E, T_T, D_{cell}\}$  and  $\{E, \epsilon_{max}, D_{cell}\}$  result in 94% accuracy. The highest accuracy of 96% can be obtained using four parameters  $\{E, T_T, D_{cell}, \epsilon_{max}\}$  (Fig. 2B). Surprisingly, we find that using additional q-DC parameters does not improve classification accuracy, which ranges from 92% to 96% when using five and six physical phenotypes; this highlights how highly correlated parameters, such as  $T_T$  and  $T_C$ , do not add unique value to cell classification accuracy. Therefore,  $\{E, T_T, D_{cell}, \epsilon_{max}\}$  constitute the ‘reduced set’ of parameters as they provide the highest classification accuracy with the least amount of parameters.

Since transit time  $T_T$  is a common metric for mechanotype that is obtained by transit-based deformability cytometry (20), we next evaluate the benefit of q-DC parameters by comparing the performance of the k-NN algorithm using the reduced set of parameters to  $T_T$  alone (Fig. 2C,D). For the k-NN algorithm using  $T_T$  as a single predictor, we find the algorithm performs poorly: the true positive rate for each cell line ranges from 0.33 to 0.86 (Fig. 2C). For example, the true positive rate for PANC-1 cells is 0.33, indicating that only 33% of PANC-1 samples are correctly identified as PANC-1 cells, 41% are incorrectly identified as HPDE cells, and 26% as AsPC-1 cells (Fig. 2C). When  $\{T_T\}$  is used, the true positive rate averaged across all cell lines is 0.65 and the false positive rate is 0.35. By contrast, the

reduced set of q-DC parameters  $\{E, T_T, D_{cell}, \epsilon_{max}\}$  significantly improves the average true positive rate to 0.96. For example, the true positive rate for PANC-1 cells is 1.0, where 100% of PANC-1 samples are correctly identified. Additionally, the true positive rate for Hs766T is 0.94, where 94% of Hs766T samples are correctly identified, while 6% are identified as MIA PaCa-2 (Fig. 2D). We also observe the reduced set  $\{E, T_T, D_{cell}, \epsilon_{max}\}$  decreases the false positive rate, which ranges from 0 to 0.06 (average = 0.04) (Fig. 2D). Taken together, these findings indicate that q-DC predictors increase the accuracy for classifying PDAC cell lines compared to  $T_T$  alone.

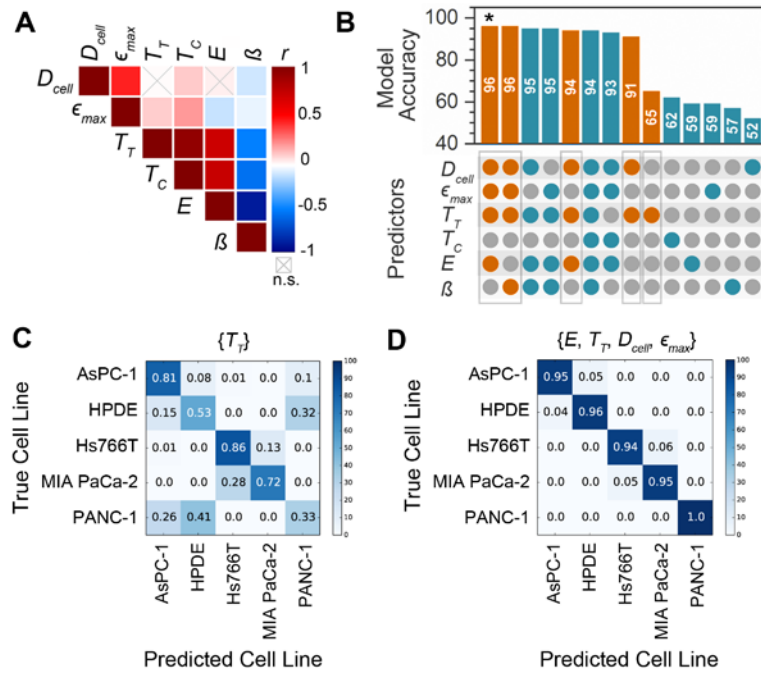


**Fig. 2. Predictive power of q-DC outputs for cell classification.** (A) Spearman's rank correlation coefficients for pairs of q-DC outputs: elastic modulus  $E$ , cell fluidity  $\beta$ , transit time  $T_T$ , creep time  $T_C$ , cell size  $D_{cell}$ , and maximum strain  $\epsilon_{max}$ . Color represents the magnitude of the correlation coefficient,  $r$ , as detailed in S. Table. 1. Gray 'X' denotes not statistically significant (n.s.). (B) Accuracy of k-nearest neighbor machine learning algorithm for classifying human pancreatic cell lines. Each bar represents the accuracy of models built with varying combinations of q-DC predictors as indicated by the colored dots; grey dots represent excluded predictors. Orange bars and dots represent the highest accuracy that can be achieved with a set of one, two, three, and four physical phenotypes. Turquoise bars and dots show accuracy obtained by all other

combinations of physical phenotypes. Asterisk shows the reduced set of predictors that provides the greatest accuracy with the least number of parameters. White numbers show the accuracy, which is calculated as the percentage of data subsets that are correctly identified as one of the five pancreatic cell lines. S. Fig. 1 illustrates the accuracy of models using additional combinations of q-DC predictors. (C-D) Confusion matrices show the performance of the k-NN algorithm for (C) transit time  $T_T$ , and (D) reduced set of q-DC predictors: elastic modulus  $E$ , transit time  $T_T$ , cell size  $D_{cell}$ , and maximum strain  $\epsilon_{max}$ . Rows represent the true cell line; columns represent the predicted cell line. Color scale denotes the proportion of cells predicted as each cell type.

**Relationship of physical phenotypes to cancer cell invasion.** Defining how cancer cell physical phenotypes relate to functional behaviors, such as invasion, could provide valuable biomarkers that have physiologically relevant predictive power. Invasion is fundamentally a physical process, whereby cells deform and move through narrow gaps of the extracellular matrix. The invasion of cancer cells is associated with physical phenotypes such as cell stiffness or elastic modulus: while in some contexts more invasive cells are more compliant (5–11), there are other cases where more invasive cells are stiffer (12–16). Other physical phenotypes, such as cell size and deformation timescale can also determine the ability of cells to deform through narrow gaps (21). While correlations between individual physical phenotypes and invasion have been investigated (12, 32, 40), it is not known how these phenotypes could collectively provide an improved biomarker for invasion.

To determine the relationship between the reduced set of physical phenotypes  $\{E, T_T, D_{cell}, \epsilon_{max}\}$  and cancer cell invasion (Fig. 3A), we first evaluate the correlation between invasion and single physical phenotypes. Across the panel of PDAC cell lines, we find that individual parameters from the reduced set have poor to moderate correlations with invasion as measured using a 3D scratch wound invasion assay (12, 32): Pearson’s correlation yields  $R^2$  that range from  $R_{D-Inv}^2 = 0.05 \pm 0.001$  to  $R_{E-Inv}^2 = 0.45 \pm 0.006$  (Fig. 3B). We find the strongest correlation of a single parameter with invasion for  $E$  ( $R_{E-Inv}^2 = 0.45 \pm 0.006$ ), whereby cells that are more invasive tend to have lower  $E$  (Fig. 3B). This trend of more invasive cells being more compliant is consistent with previous reports in breast and ovarian cancer cells (5–11). However, the inverse relationship between invasion and  $E$  does not hold across all PDAC cell lines as

MIA PaCa-2 cells exhibit the lowest elastic modulus yet reduced invasion compared to Hs766T and PANC-1 cells (Fig. 3B).

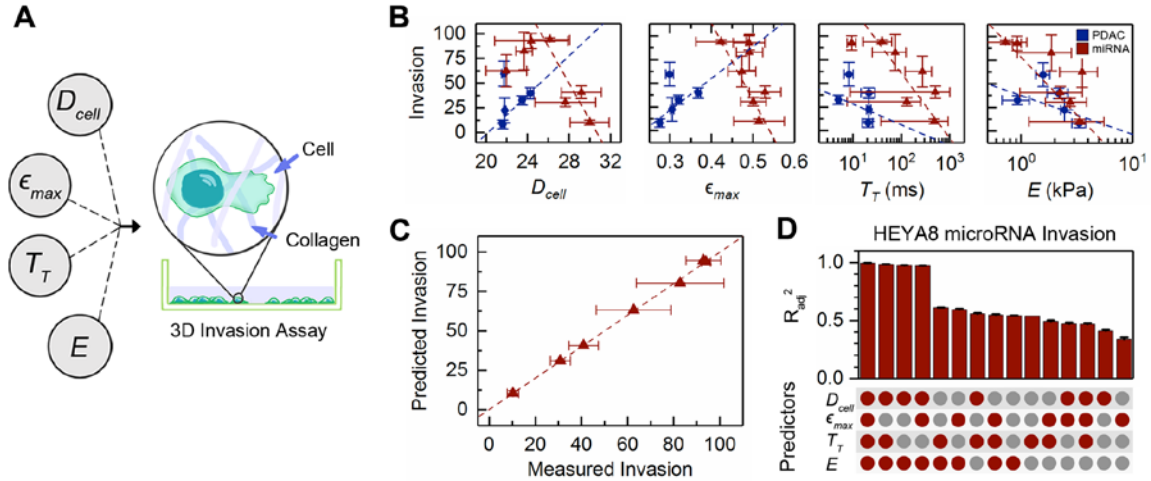


**Fig. 3. Relationship of q-DC parameters and invasion across cancer cell types.** (A) Schematic illustration the reduced set of physical phenotypes, which we use to predict cell invasion, elastic modulus  $E$ , transit time  $T_T$ , cell size  $D_{cell}$ , and maximum strain  $\epsilon_{max}$ , as measured using 3D invasion assay. (B) Plots showing invasion versus single physical phenotypes for pancreatic adenocarcinoma (PDAC) cell lines (blue circles) and ovarian cancer (HEYA8) cells that overexpress a panel of tumor suppressor microRNAs (red triangles). Each data point represents the median value for a cell sample. Error bars represent standard deviation. Dashed lines show best linear fits. (C) Correlation between measured and predicted invasion using the physical phenotype model for invasion. Dashed lines show best linear fit for the microRNA-overexpressing cells. Data points represent the average value for a cell sample. Error bars represent standard deviation. (D) The strength of correlations between measured and predicted invasion from linear regression models built with combinations of physical phenotypes for microRNA-overexpressing ovarian cancer cells. Colored circles illustrate the set of predictors used in the model. Bars represent adjusted- $R^2$  ( $R_{adj}^2$ ) values, which reflect the average strength of the correlation, while accounting for the number of fitting parameters to data points. Error bars represent standard deviation.

We also physical phenotype seven ovarian cancer cell samples that overexpress distinct tumor-suppressor microRNAs; higher levels of expression of these microRNAs are associated with improved patient survival, as identified through Cancer Genome Atlas (TCGA) data (31). We previously found that these

tumor suppressor microRNAs decrease cell invasion (31, 32) and tend to increase cell transit time (32). Physical phenotyping by q-DC reveals that individual phenotypes of microRNA-overexpressing cells also exhibit only moderate correlations to invasion (Fig. 3B). While we find that higher  $E$  and  $T_T$  are associated with decreased invasion across both established pancreatic cancer cell lines and ovarian cancer cells with manipulated microRNA levels, we find opposite trends for  $D_{cell}$  and  $\epsilon_{max}$  (Fig. 3B); these discrepancies further substantiate the low predictive power of individual physical phenotypes. As single physical phenotypes are not sufficient to predict invasion, we next investigate if multiparameter analysis using the reduced set of four physical phenotypes can collectively predict cancer invasion.

To develop a model that can predict cell invasion on the basis of physical phenotypes, we train a multiple linear regression model using  $\{E, T_T, D_{cell}, \epsilon_{max}\}$  and invasion data. While we use data from numerous cell samples, linear regression can be susceptible to overfitting when the number of fitting parameters approaches the number of data points. Therefore, we account for the number of predictors in the strength of correlation between the measured and predicted invasion using the adjusted- $R^2$  ( $R^2_{adj}$ ),

$$R^2_{adj} = 1 - \left[ \frac{(1-R^2)(n-1)}{n-m-1} \right], \quad \text{Eq. 3}$$

where  $n$  is the number of observations and  $m$  is the number of predictors. For the PDAC cell lines, an  $R^2_{adj}$  value does not exist, as there are four fitting parameters in the reduced set and only five cell lines. Reducing the number of predictors only yields  $R^2_{adj}$  that are similar to correlations between single parameters and invasion (S. Fig. 2). However, building the linear regression model using invasion and physical phenotype data  $\{E, T_T, D_{cell}, \epsilon_{max}\}$  from seven ovarian cancer cell samples that overexpress distinct microRNAs results in invasion values that are highly correlated with experimental observations, as indicated by the high  $R^2_{adj} = 1.00 \pm 0.002$  (Fig. 3D); we call this multiple linear regression model built with the reduced set the ‘physical phenotype model for invasion’, as it demonstrates robustness to predict invasion. We also train models with smaller sets of predictors; however, we find that reduced set of

physical phenotypes ( $E$ ,  $T_T$ ,  $D_{cell}$ ,  $\epsilon_{max}$ ) yields the highest  $R_{adj}^2$  value, and thus generates the strongest predictive model with the smallest number of parameters (Fig. 3D).

**Predicting invasion using label-free physical phenotypes.** To validate the physical phenotyping model for invasion, we measure physical phenotypes of seven additional cancer cell samples, and determine how accurately we can predict their invasion. We first use q-DC to physical phenotype three breast cancer cell lines, MDA-MB-231, MDA-MB-468, and MCF-7 (Fig 4A). These cell lines are well characterized to have varying invasive potentials, from highest to lowest: MDA-MB-231 > MDA-MB-468 > MCF-7 (41–45). Other key characteristics of progression are also described for these cell lines, including the propensity to form cell colonies (MDA-MB-231 > MDA-MB-468 > MCF-7) (45). By physical phenotyping using q-DC, we find that MDA-MB-231 cells have decreased  $E$  compared to both MDA-MB-468 and MCF-7 cells ( $E_{MDA-MB-231} = 1.2 \pm 0.3$  kPa <  $E_{MCF-7} = 2.0 \pm 0.2$  kPa <  $E_{MDA-MB-468} = 2.7 \pm 0.3$  kPa). Compared to the ranking of invasion of these cells types, we find a weak correlation between  $E$  and invasion, which is further quantified by Spearman’s correlation coefficient ( $r = 0.5$ ); these findings support that  $E$  alone is not sufficient to predict invasion. We find that transit times follow the same ranking as  $E$ , whereby  $T_{T-MDA-MB-231} = 15 \pm 3$  ms <  $T_{T-MCF-7} = 25 \pm 5$  ms <  $T_{T-MDA-MB-468} = 57 \pm 27$  ms (Fig. 4A). Thus, neither  $E$  nor  $T_T$  is sufficient to predict invasion. However, we discover that the physical phenotyping model for invasion correctly ranks the invasion of these breast cancer cell lines, MDA-MB-231 > MDA-MB-468 > MCF-7 (Fig. 4D). These results further substantiate the power of multiparameter analysis to predict invasion based on label-free physical phenotyping of single cancer cells.

To further validate the physical phenotyping model for invasion, we predict the invasion of ovarian cancer (OVCA433) cells that have been genetically manipulated to generate a pair of epithelial- and mesenchymal-like cell lines. Cancer cells with overexpression of Snail (33) (OVCA433-Snail), a key transcription factor in epithelial-to-mesenchymal transition (EMT) (46), are mesenchymal-like and exhibit increased invasion (46). By contrast, the control cells (OVCA433-GFP) are epithelial-type. Using q-DC to physical phenotype this pair of cell lines, we find that OVCA433-Snail cells have a reduced  $E$

compared to the OVCA433-GFP control cells ( $E_{\text{OVCA-GFP}} = 1.8 \pm 0.1$  kPa;  $E_{\text{OVCA-Snail}} = 1.0 \pm 0.7$  kPa;  $p \ll 0.001$ ) (Fig 4B). We also observe that OVCA433-Snail cells exhibit shorter transit times than OVCA433-GFP ( $T_{T-\text{OVCA-GFP}} = 22 \pm 2.8$  ms;  $T_{T-\text{OVCA-Snail}} = 16 \pm 1.2$  ms,  $p \ll 0.001$ ), consistent with the decreased stiffness of the mesenchymal-type OVCA433-Snail cells (Fig. 4B). Using q-DC outputs, we demonstrate that the physical phenotype model for invasion has the power to predict the increased invasion of the OVCA433-Snail cells compared to the control OVCA433-GFP cells (Fig. 4B); these results also demonstrate that physical phenotypes measured by q-DC are consistent with other hallmark characteristics of EMT, such as the increased vimentin to E-cadherin ratio (47) and ability to form cell colonies (48), which are commonly used to define mesenchymal-type cells.

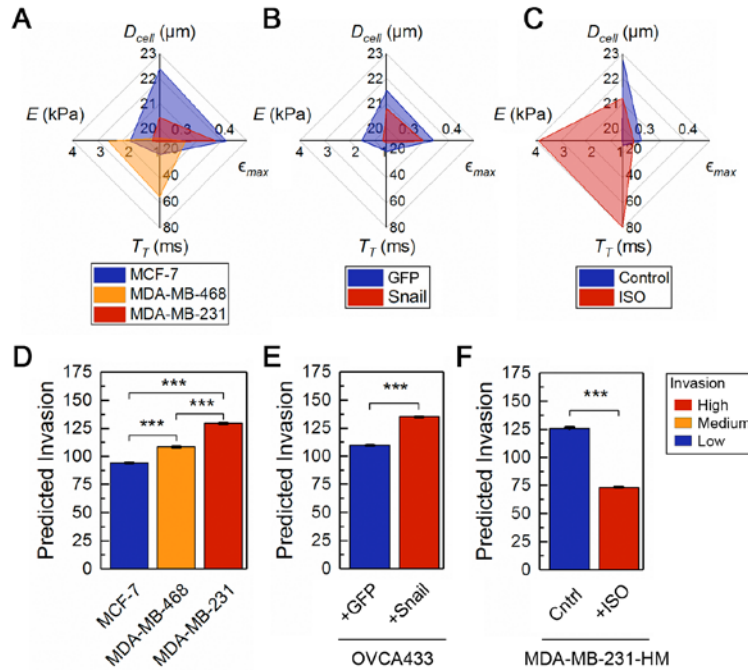


**Fig. 4. Predicting invasion by multiparameter physical phenotyping.** (A-C) The four key physical phenotypes that comprise the reduced set for: (A) breast cancer cells, MCF-7, MDA-MB-468, and MDA-MB-231; (B) ovarian cancer cells, OVCA433-GFP control, and OVCA433 that overexpresses Snail (OVCA433-Snail), a key transcription factor in epithelial-to-mesenchymal transition (EMT); (C) Highly metastatic human breast cancer (MDA-MB-231-HM) cells with activation of  $\beta$ -adrenergic signaling by treatment with 100 nM isoproterenol (+ISO) or vehicle (Control) for 24 h.  $N > 400$ . (D-F) Average predicted invasion as determined by the physical

phenotyping model for invasion. Error bars represent the standard deviation. Colors represent previously determined invasive potentials, as described in literature (13, 42–45).

We next assess how increased cell invasion that is caused by pharmacologic manipulation can be predicted by the physical phenotype model of invasion. We previously showed that cancer cells treated with the  $\beta$ -adrenergic agonist, isoproterenol, have increased invasion *in vitro* (13). Activation of  $\beta$ -adrenergic signaling also promotes metastasis in clinically-relevant orthotopic mouse models of breast cancer (34, 49). Following treatment of highly metastatic human breast cancer (MDA-MB-231-HM) cells with isoproterenol, we find that  $E$  increases from  $E_{\text{Control}} = 0.9 \pm 0.4$  kPa to  $E_{\text{ISO}} = 4.0 \pm 0.6$  kPa ( $p = 0.001$ ) (Fig. 4C). Similarly,  $T_T$  increases from  $T_{T-\text{Control}} = 18 \pm 4.2$  ms to  $T_{T-\text{ISO}} = 81 \pm 31$  ms ( $p \ll 0.001$ ) (13) (Fig. 4C). While we measure statistically significant differences in cell physical phenotypes with this pharmacologic perturbation, the physical phenotyping model for invasion does not accurately predict the effects of isoproterenol on cancer cell invasion (Fig 4F). The inability of the physical phenotyping model to predict the increased invasion caused by this pharmacologic manipulation suggests that there is a fundamentally different relationship between the physical phenotypes of cells with activation of  $\beta$ -adrenergic signaling and invasion compared to the other sets of cancer cells that we investigate here.

## Discussion

Our results across 18 distinct samples of ovarian, breast, and pancreatic cancer cells show that cell stiffness alone, as indicated by  $E$  or  $T_T$ , is not sufficient to predict invasion. Using label-free, multiparameter physical phenotyping of single cells, we develop the physical phenotyping model that can predict invasion using four parameters—elastic modulus  $E$ , transit time  $T_T$ , maximum strain  $\epsilon_{\text{max}}$ , and cell size  $D_{\text{cell}}$ —which can be rapidly measured using q-DC. We demonstrate the model’s predictive power across cell lines, which have inherent differences in invasive potential, as well as for cells that have increased invasive potential caused by genetic manipulations.



**Physical phenotypes as indicators of invasion.** While cell classification is the basis for malignant diagnosis, the ability to rapidly physical phenotype populations of single cells, and predict their invasive ability, would greatly reduce the time required to measure cell invasion, which is typically hours to days. Using q-DC and machine learning, we find that the strongest indicators of invasion for microRNA-overexpressing ovarian cancer cells are  $E$ ,  $T_T$ ,  $\epsilon_{max}$ , and  $D_{cell}$ .

**Elastic modulus.**  $E$  is an essential indicator of invasion in the physical phenotype model. Our investigation of physical phenotypes across 18 cell samples, including established cell lines and a range of genetic and pharmacologic perturbations, provide the opportunity to examine how broadly the relationship between cell stiffness and invasion can be generalized. Interestingly, while we find that  $E$  tends to decrease for cells that are more invasive, we also identify contexts where more invasive cells are stiffer. For example, across pancreatic cancer cell lines, we find that more invasive cells are more compliant. Yet, we also find that PANC-1 and Hs766T cells, which are more invasive, are stiffer compared to MIA PaCa-2 cells. We also observe that while many of the microRNAs cause ovarian cancer (HEYA8) cells to become stiffer and less invasive, overexpression of microRNA 509-5p causes cells to be stiffer and *more* invasive. There are additional examples of more invasive cells being stiffer in the breast cancer panel, where MDA-MB-468 are stiffer, yet more invasive than MCF-7 cells. Treatment of MDA-MB-231 cells with isoproterenol also causes cells to be stiffer and more invasive. These and other cases of more invasive cells that are stiffer (12–16), highlight how the concept that elastic modulus is inversely correlated with invasion is oversimplified.

**Transit time.** While transit time  $T_T$  is commonly used to distinguish cancer cell types (20), this parameter alone is not a strong indicator of invasion. We find moderate to poor correlations between  $T_T$  and invasion across well-characterized cell lines and microRNA-overexpressing cells. The emergence of  $T_T$  as an indicator of invasion in the physical phenotyping model suggests that the ability of cells to continuously deform may be important in invasion. While  $E$  reflects the ability of a cell to resist initial deformation, and thus dominates viscoelastic response on short  $\sim$ ms timescales (21), transit time captures the ability of

a cell to deform through the entire constriction. We showed previously that  $T_T$  depends on both elastic and viscous properties (21); indeed, invasion occurs over hours to days (38), where viscous contributions may be more relevant.

**Size.** We also find that cell size  $D_{cell}$  strengthens the accuracy of the physical phenotype model to predict invasion. We and others previously determined that cell size is inversely correlated with invasion potential (9, 32), which may reflect how smaller cells can more readily invade through a matrix. Cell size also determines the probability of cells to occlude narrow capillaries or pores (50, 51), and thus may be implicated in lodging of cells in metastatic target sites, such as the narrow capillaries of the pulmonary beds of the lung (52). The effects of cell size may also reflect contributions of the cell nucleus to q-DC measurements: nuclear size scales with cell size (12), and the nucleus tends to be stiffer than the surrounding cytoplasm (11). Moreover, increased nuclear-to-cytoplasmic volume is a hallmark of malignant cells with diagnostic value (2, 53, 54). Morphological parameters, such as eccentricity and circularity, are also identified as strong predictors of cancer cell types (25).

**Effects of measurement techniques on multiparameter physical phenotyping.** Since different methods for physical phenotyping probe cells over different time and length scales, it is not clear how broadly the predictors of invasion that we have identified using q-DC may be extended to other methods. Despite differences in the deformation depth and timescale between q-DC and a conventional mechanotyping method, such as AFM, we observe a similar range of elastic modulus values obtained using q-DC and AFM of cells that are cultured under the same conditions (12). However, we find the ranking of elastic moduli determined by q-DC and AFM is not consistent: by q-DC from stiffest to most compliant, AsPC-1 > HPDE > PANC-1 > Hs766T > MIA PaCa-2, and by AFM, Hs766T ~ HPDE > PANC-1 > MIA PaCa-2. One notable difference is the Hs766T cells: they are the stiffest PDAC cell line measured by AFM and second most compliant cell line by q-DC, despite having an elastic modulus of a similar order of magnitude ( $3.0 \pm 2.0$  kPa by AFM and  $1.6 \pm 0.2$  kPa by q-DC). This difference between cell mechanotype measured by these two methods may be attributed to the difference in cell measurement

state: microfluidic methods such as q-DC probe cells in a suspended state, whereas AFM measures adhered cells. When cells lift off from the substrate into a suspended state, they undergo dramatic cytoskeletal rearrangements and exhibit altered distributions of F-actin (55). By contrast, cells that are attached to a substrate also generate intracellular tension, or ‘prestress’ (56), which can contribute to cell stiffness measurements (57, 58). Therefore, the stiffness of the Hs766T cells measured by AFM may reflect their increased contractility and/or stress fiber formation compared to when they are in suspension. Since the stiffness of adhered cells depends on myosin II activity (59–62) and traction stresses scale with cell metastatic potential (63), mechanotyping of adhered cells may thus provide an additional, complementary physical indicator of cell invasion. This example of cell mechanotype differences in adhered and suspended states highlights why measuring the mechanical properties of cells using complementary methods could provide valuable information about the passive and active contributions to cell deformability. Measurements of adhered and suspended cells may also provide deeper insight into the possible functional significance of cell mechanotype. While cell deformations are required for adhered cells during invasion, extravasation, and intravasation (52, 64), cells in a suspended state deform during circulation through the blood and lymphatic vasculature (52, 64).

**Benefits of multiparameter analysis for predicting cell invasion.** Cell physical phenotypes are emerging as valuable, complementary biomarkers for cell classification and clinical benefit (8,22,23,24). While enhanced predictive power can be achieved with additional parameters obtained by q-DC, extra computation is required to extract parameters such as elastic modulus  $E$ , cell fluidity  $\beta$ , creep time  $T_C$ , and maximum strain  $\epsilon_{max}$  (22). The tradeoff between classification accuracy and computational expense will ultimately depend on the specific application. For example, certain cancer cell populations can be distinguished using measurements of  $T_T$  and  $D_{cell}$ , which rely on simple image analysis (10, 19–21, 36, 38). With greater computational investment, including tracking the time-dependent changes in cell shape during deformation and fitting single-cell creep trajectories to power law rheology models, additional parameters such as  $\epsilon_{max}$  and  $E$  can be determined (22). However, such enhanced resolution may not be

essential for specific applications. For example, the invasion of the epithelial-type OVCA433-GFP cells versus the mesenchymal-type OVCA433-Snail cells is accurately ranked by  $E$  alone (Fig 4E). In future applications, more advanced machine learning algorithms could bypass the additional image analysis required for q-DC; for example, neural network algorithms can be trained using images with minimal processing, and thus do not require the additional computational steps to extract physical phenotypes.

Additional biophysical markers may also broaden the application of the physical phenotype model to contexts where the model does not accurately predict invasion, such as in the case of pharmacologic perturbations. Specifically, activation of  $\beta$ -adrenergic signaling alters single-cell physical phenotypes and invasion, but in a way that is not consistent with the other cell samples, including both cell lines and genetically-modified cells, that we investigate here. Further studies of how  $\beta$ -adrenergic signaling alters cell physical phenotypes should deepen our understanding of the relationship between invasion and physical phenotypes and facilitate the discovery of additional biomarkers, such as contractility, for invasion. Invasion is a complex and highly dynamic process requiring deformation through micron-scale pores (52, 65), actin protrusion formation (66), generation of traction forces (63), and secretion of proteases (67–69). For example, the increased stiffness of cells with activation of  $\beta$ -adrenergic signaling requires myosin II activity (13); myosin II is also required for actomyosin contractility, which increases cell stiffness in adhered states (59–62) and generates forces required for cells to invade through 3D matrices (70, 71).

**Navigating the physical fitness landscape of invasion.** While the physical phenotype model for invasion relies on the reduced set of parameters—elastic modulus  $E$ , transit time  $T_T$ , maximum strain  $\epsilon_{max}$ , and cell size  $D_{cell}$ —it is intriguing to speculate if these physical phenotypes reflect a particular strategy for optimizing cell invasion. We observe that more invasive cells tend to have lower elastic modulus and smaller cell size (Fig 3B). However, the predictive power of the physical phenotype model for is based on the multiparameter physical signature of invasive cells. Future studies to better elucidate the interplay

between physical phenotypes in the invasion fitness landscape will deepen our understanding of selective advantages that may be acquired by cancer cells to enhance their invasion.

Our findings that the physical phenotype model for invasion cannot predict the increased invasion of cancer cells with  $\beta$ -adrenergic activation may imply that different physical signatures reflect different strategies for cancer cell invasion. Deeper investigation of contexts where invasion cannot be predicted by the physical phenotype model for invasion may reveal another regime that is described by a different set of phenotypes that can predict invasion. Identifying additional complementary biomarkers could generate a more inclusive—even universal—model to predict invasion across varied contexts.

While we focus here on using physical phenotypes as indicators of invasion, the rapid, calibrated measurements of q-DC have exciting potential to also provide mechanistic insights into the invasive behavior of cancer cells. Since proteins of the mechanome and contractome, which regulate cancer cell physical phenotypes, are also essential in invasion (32), determining the molecular origins of cell physical phenotypes should reveal novel mediators and pathways that can be targeted to stop cancer cell invasion.

## **Conclusion**

The q-DC method for single-cell physical phenotyping coupled with machine learning algorithms provides a crucial step towards enhanced classification of cancer cell types. Our findings also link cancer cell physical phenotypes with functional behaviors such as invasion, establishing a framework for predicting invasion based on label-free biomarkers that can be rapidly measured. The ability of q-DC to enable calibrated, multiparameter cell physical phenotyping to classify cell types and predict cellular behaviors is valuable for biomedical applications, and should offer unprecedented insight into heterogeneous populations of cells that include subpopulations of drug-resistant cancer cells to undifferentiated stem cells.

## References

1. Brown, M., and C. Wittwer. 2000. Flow cytometry: principles and clinical applications in hematology. *Clin. Chem.* 46: 1221–1229.
2. Elston, C.W., and I.O. Ellis. 1991. Pathological prognostic factors in breast cancer. I. The value of histological grade in breast cancer: experience from a large study with long-term follow-up. *Histopathology.* 19: 403–410.
3. Webster, M., K.L. Witkin, and O. Cohen-Fix. 2009. Sizing up the nucleus: nuclear shape, size and nuclear-envelope assembly. *J. Cell Sci.* 122: 1477–86.
4. Guilak, F., J.R. Tedrow, and R. Burgkart. 2000. Viscoelastic properties of the cell nucleus. *Biochem. Biophys. Res. Commun.* 269: 781–786.
5. Guck, J., S. Schinkinger, B. Lincoln, F. Wottawah, S. Ebert, M. Romeyke, D. Lenz, H.M. Erickson, R. Ananthakrishnan, D. Mitchell, others, J. Käs, S. Ulvick, and C. Bilby. 2005. Optical deformability as an inherent cell marker for testing malignant transformation and metastatic competence. *Biophys. J.* 88: 3689–98.
6. Cross, S.E., Y.-S. Jin, J. Rao, and J.K. Gimzewski. 2007. Nanomechanical analysis of cells from cancer patients. *Nat. Nanotechnol.* 2: 780–3.
7. Hur, S.C., N.K. Henderson-MacLennan, E.R.B. McCabe, and D. Di Carlo. 2011. Deformability-based cell classification and enrichment using inertial microfluidics. *Lab Chip.* 11: 912–920.
8. Xu, W., R. Mezencev, B. Kim, L. Wang, J. McDonald, and T. Sulchek. 2012. Cell stiffness is a biomarker of the metastatic potential of ovarian cancer cells. *PLoS One.* 7: e46609.
9. Swaminathan, V., K. Mythreye, E.T. O’Brien, A. Berchuck, G.C. Blobe, and R. Superfine. 2011. Mechanical stiffness grades metastatic potential in patient tumor cells and in cancer cell lines. *Cancer Res.* 71: 5075–5080.
10. Hou, H.W., Q.S. Li, G.Y.H. Lee, a. P. Kumar, C.N. Ong, and C.T. Lim. 2009. Deformability study of breast cancer cells using microfluidics. *Biomed. Microdevices.* 11: 557–564.

11. Agus, D.B., J.F. Alexander, W. Arap, S. Ashili, J.E. Aslan, R.H. Austin, V. Backman, K.J. Bethel, R. Bonneau, W.-C. Chen, C. Chen-Tanyolac, N.C. Choi, S.A. Curley, M. Dallas, D. Damania, P.C.W. Davies, P. Decuzzi, L. Dickinson, L. Estevez-Salmeron, V. Estrella, M. Ferrari, C. Fischbach, J. Foo, S.I. Fraley, C. Frantz, A. Fuhrmann, P. Gascard, R.A. Gatenby, Y. Geng, S. Gerecht, R.J. Gillies, B. Godin, W.M. Grady, A. Greenfield, C. Hemphill, B.L. Hempstead, A. Hielscher, W.D. Hillis, E.C. Holland, A. Ibrahim-Hashim, T. Jacks, R.H. Johnson, A. Joo, J.E. Katz, L. Kelbaskas, C. Kesselman, M.R. King, K. Konstantopoulos, C.M. Kraning-Rush, P. Kuhn, K. Kung, B. Kwee, J.N. Lakins, G. Lambert, D. Liao, J.D. Licht, J.T. Liphardt, L. Liu, M.C. Lloyd, A. Lyubimova, P. Mallick, J. Marko, O.J.T. McCarty, D.R. Meldrum, F. Michor, S.M. Mumenthaler, V. Nandakumar, T. V O'Halloran, S. Oh, R. Pasqualini, M.J. Paszek, K.G. Philips, C.S. Poultney, K. Rana, C.A. Reinhart-King, R. Ros, G.L. Semenza, P. Senechal, M.L. Shuler, S. Srinivasan, J.R. Staunton, Y. Stypula, H. Subramanian, T.D. Tlsty, G.W. Tormoen, Y. Tseng, A. van Oudenaarden, S.S. Verbridge, J.C. Wan, V.M. Weaver, J. Widom, C. Will, D. Wirtz, J. Wojtkowiak, and P.-H. Wu. 2013. A physical sciences network characterization of non-tumorigenic and metastatic cells. *Sci. Rep.* 3: 1449.
12. Nguyen, A. V, K.D. Nyberg, M.B. Scott, A.M. Welsh, A.H. Nguyen, N. Wu, S. V Hohlbauch, N.A. Geisse, E.A. Gibb, A.G. Robertson, T.R. Donahue, and A.C. Rowat. 2016. Stiffness of pancreatic cancer cells is associated with increased invasive potential. *Integr. Biol.* .
13. Kim, T.-H., N.K. Gill, K.D. Nyberg, A. V Nguyen, S. V Hohlbauch, N.A. Geisse, C.J. Nowell, E.K. Sloan, and A.C. Rowat. 2016. Cancer cells become less deformable and more invasive with activation of beta-adrenergic signaling. *J. Cell Sci.* 129: 4563–4575.
14. Liu, C.-Y., H.-H. Lin, M.-J. Tang, and Y.-K. Wang. 2015. Vimentin contributes to epithelial-mesenchymal transition cancer cell mechanics by mediating cytoskeletal organization and focal adhesion maturation. *Oncotarget.* 6: 15966–15983.
15. Rathje, L.-S.Z., N. Nordgren, T. Pettersson, D. Ronnlund, J. Widengren, P. Aspenstrom, and A.K.B. Gad. 2014. Oncogenes induce a vimentin filament collapse mediated by HDAC6 that is

- linked to cell stiffness. *Proc. Natl. Acad. Sci. U. S. A.* 111: 1515–1520.
16. Weder, G., M.C. Hendriks-Balk, R. Smajda, D. Rimoldi, M. Liley, H. Heinzelmann, A. Meister, and A. Mariotti. 2014. Increased plasticity of the stiffness of melanoma cells correlates with their acquisition of metastatic properties. *Nanomedicine.* 10: 141–148.
  17. Lange, J.R., J. Steinwachs, T. Kolb, L.A. Lautscham, I. Harder, G. Whyte, and B. Fabry. 2015. Microconstriction Arrays for High-Throughput Quantitative Measurements of Cell Mechanical Properties. *Biophys. J.* 109: 26–34.
  18. Hoelzle, D.J., B.A. Varghese, C.K. Chan, and A.C. Rowat. 2014. A Microfluidic Technique to Probe Cell Deformability. *JoVE.* 91: e51474–e51474.
  19. Byun, S., S. Son, D. Amodei, N. Cermak, J. Shaw, J.H. Kang, V.C. Hecht, M.M. Winslow, T. Jacks, P. Mallick, and S.R. Manalis. 2013. Characterizing deformability and surface friction of cancer cells. *Proc. Natl. Acad. Sci.* 110: 7580–7585.
  20. Rosenbluth, M.J., W.A. Lam, and D.A. Fletcher. 2008. Analyzing cell mechanics in hematologic diseases with microfluidic biophysical flow cytometry. *Lab Chip.* 8: 1062–1070.
  21. Nyberg, K.D., M.B. Scott, S.L. Bruce, A.B. Gopinath, D. Bikos, T.G. Mason, J.W. Kim, H.S. Choi, and A.C. Rowat. 2016. The physical origins of transit time measurements for rapid, single cell mechanotyping. *Lab Chip.* 16: 3330–3339.
  22. Nyberg, K.D., K.H. Hu, S.H. Kleinman, D.B. Khismatullin, M.J. Butte, and A.C. Rowat. 2017. Quantitative Deformability Cytometry (q-DC): rapid, calibrated measurements of single cell viscoelastic properties. *Biophys. J.* in press.
  23. Bongiorno, T., J.L. Chojnowski, J.D. Lauderdale, and T. Sulchek. 2016. Cellular Stiffness as a Novel Stemness Marker in the Corneal Limbus. *Biophys. J.* 111: 1761–1772.
  24. Bongiorno, T., J. Kazlow, R. Mezencev, S. Griffiths, R. Olivares-Navarrete, J.F. McDonald, Z. Schwartz, B.D. Boyan, T.C. McDevitt, and T. Sulchek. 2014. Mechanical stiffness as an improved single-cell indicator of osteoblastic human mesenchymal stem cell differentiation. *J. Biomech.* 47: 2197–2204.



25. Lin, J., D. Kim, T.T. Henry, P. Tseng, L. Peng, M. Dhar, S. Karumbayaram, and D. Di Carlo. 2017. High-throughput physical phenotyping of cell differentiation. *Microsystems Nanoeng.* 3: 17013.
26. Darling, E.M., M. Topel, S. Zauscher, T.P. Vail, and F. Guilak. 2008. Viscoelastic properties of human mesenchymally-derived stem cells and primary osteoblasts, chondrocytes, and adipocytes. *J. Biomech.* 41: 454–464.
27. Darling, E.M., and F. Guilak. 2008. A neural network model for cell classification based on single-cell biomechanical properties. *Tissue Eng. Part A.* 14: 1507–1515.
28. Tse, H.T.K., D.R. Gossett, Y.S. Moon, M. Masaeli, M. Sohsman, Y. Ying, K. Mislick, R.P. Adams, J. Rao, and D. Di Carlo. 2013. Quantitative diagnosis of malignant pleural effusions by single-cell mechanophenotyping. *Sci. Transl. Med.* 5: 212ra163.
29. Jiang, Y., C. Lei, A. Yasumoto, H. Kobayashi, Y. Aisaka, T. Ito, B. Guo, N. Nitta, N. Kutsuna, Y. Ozeki, A. Nakagawa, Y. Yatomi, and K. Goda. 2017. Label-free detection of aggregated platelets in blood by machine-learning-aided optofluidic time-stretch microscopy. *Lab Chip.* 17: 2426–2434.
30. Lee, W.C., H. Shi, Z. Poon, L.M. Nyan, T. Kaushik, G. V Shivashankar, J.K.Y. Chan, C.T. Lim, J. Han, and K.J. Van Vliet. 2014. Multivariate biophysical markers predictive of mesenchymal stromal cell multipotency. *Proc. Natl. Acad. Sci.* 111: E4409-18.
31. Pan, Y., G. Robertson, L. Pedersen, E. Lim, A. Hernandez-Herrera, A.C. Rowat, S.L. Patil, C.K. Chan, Y. Wen, X. Zhang, U. Basu-Roy, A. Mansukhani, A. Chu, P. Sipahimalani, R. Bowlby, D. Brooks, N. Thiessen, C. Coarfa, Y. Ma, R.A. Moore, J.E. Schein, A.J. Mungall, J. Liu, C. V Pecot, A.K. Sood, S.J.M. Jones, M.A. Marra, and P.H. Gunaratne. 2016. miR-509-3p is clinically significant and strongly attenuates cellular migration and multi-cellular spheroids in ovarian cancer. *Oncotarget.* 7: 25930–25948.
32. Chan, C.K., Y. Pan, K. Nyberg, M.A. Marra, E.L. Lim, S.J.M. Jones, D. Maar, E.A. Gibb, P.H. Gunaratne, A.G. Robertson, and A.C. Rowat. 2016. Tumour-suppressor microRNAs regulate

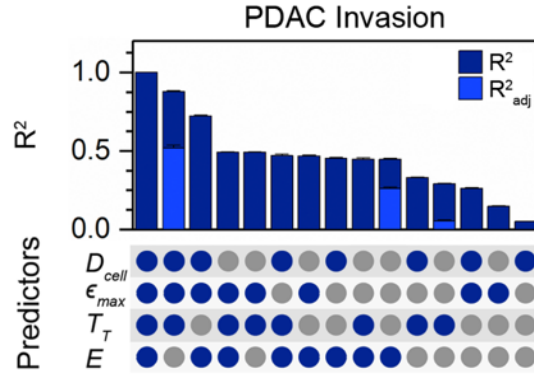
- ovarian cancer cell physical properties and invasive behaviour. *Open Biol.* 6.
33. Qi, D., N.K. Gill, C. Santiskulvong, J. Sifuentes, O. Dorigo, J. Rao, B. Taylor-Harding, W.R. Wiedemeyer, and A.C. Rowat. 2015. Screening cell mechanotype by parallel microfiltration. *Sci. Rep.* 5.
  34. Le, C.P., C.J. Nowell, C. Kim-Fuchs, E. Botteri, J.G. Hiller, H. Ismail, M.A. Pimentel, M.G. Chai, T. Karnezis, N. Rotmensz, G. Renne, S. Gandini, C.W. Pouton, D. Ferrari, A. Moller, S.A. Stacker, and E.K. Sloan. 2016. Chronic stress in mice remodels lymph vasculature to promote tumour cell dissemination. *Nat. Commun.* 7: 10634.
  35. Duffy, D.C., J.C. McDonald, O.J.A. Schueller, and G.M. Whitesides. 1998. Rapid prototyping of microfluidic systems in poly(dimethylsiloxane). *Anal. Chem.* 70: 4974–4984.
  36. Rowat, A.C., D.E. Jaalouk, M. Zwerger, W.L. Ung, I.A. Eydelnant, D.E. Olins, A.L. Olins, H. Herrmann, D.A. Weitz, and J. Lammerding. 2013. Nuclear Envelope Composition Determines the Ability of Neutrophil-type Cells to Passage through Micron-scale Constrictions. *J. Biol. Chem.* 288: 8610–8618.
  37. Lange, J.R., C. Metzner, S. Richter, W. Schneider, M. Spermann, T. Kolb, G. Whyte, and B. Fabry. 2017. Unbiased High-Precision Cell Mechanical Measurements with Microconstrictions. *Biophys. J.* 112: 1472–1480.
  38. Ekpenyong, A.E., G. Whyte, K. Chalut, S. Pagliara, F. Lautenschläger, C. Fiddler, S. Paschke, U.F. Keyser, E.R. Chilvers, and J. Guck. 2012. Viscoelastic Properties of Differentiating Blood Cells Are Fate- and Function-Dependent. *PLoS One.* 7.
  39. Fabry, B., G.N. Maksym, J.P. Butler, M. Glogauer, D. Navajas, and J.J. Fredberg. 2001. Scaling the microrheology of living cells. *Phys. Rev. Lett.* 87: 148102.
  40. Lautscham, L.A., C. Kammerer, J.R. Lange, T. Kolb, C. Mark, A. Schilling, P.L. Strissel, R. Strick, C. Gluth, A.C. Rowat, C. Metzner, and B. Fabry. 2015. Migration in Confined 3D Environments Is Determined by a Combination of Adhesiveness, Nuclear Volume, Contractility, and Cell Stiffness. *Biophys. J.* 109: 900–913.

41. Adams, M., J.L. Jones, R.A. Walker, J.H. Pringle, and S.C. Bell. 2002. Changes in tenascin-C isoform expression in invasive and preinvasive breast disease. *Cancer Res.* 62: 3289–3297.
42. Gordon, L.A., K.T. Mulligan, H. Maxwell-Jones, M. Adams, R.A. Walker, and J.L. Jones. 2003. Breast cell invasive potential relates to the myoepithelial phenotype. *Int. J. cancer.* 106: 8–16.
43. Albini, A., Y. Iwamoto, H.K. Kleinman, G.R. Martin, S.A. Aaronson, J.M. Kozlowski, and R.N. McEwan. 1987. A rapid in vitro assay for quantitating the invasive potential of tumor cells. *Cancer Res.* 47: 3239–3245.
44. Sheridan, C., H. Kishimoto, R.K. Fuchs, S. Mehrotra, P. Bhat-Nakshatri, C.H. Turner, R.J. Goulet, S. Badve, and H. Nakshatri. 2006. CD44+/CD24- breast cancer cells exhibit enhanced invasive properties: an early step necessary for metastasis. *Breast Cancer Res.* 8: R59.
45. Chekhun, S., N. Bezdenezhnykh, J. Shvets, and N. Lukianova. 2013. Expression of biomarkers related to cell adhesion, metastasis and invasion of breast cancer cell lines of different molecular subtype. *Exp. Oncol.* 35: 174–179.
46. De Craene, B., B. Gilbert, C. Stove, E. Bruyneel, F. van Roy, and G. Berx. 2005. The transcription factor snail induces tumor cell invasion through modulation of the epithelial cell differentiation program. *Cancer Res.* 65: 6237–6244.
47. Behrens, J., M.M. Mareel, F.M. Van Roy, and W. Birchmeier. 1989. Dissecting tumor cell invasion: epithelial cells acquire invasive properties after the loss of uvomorulin-mediated cell-cell adhesion. *J. Cell Biol.* 108: 2435–2447.
48. Guadamillas, M.C., A. Cerezo, and M.A. Del Pozo. 2011. Overcoming anoikis--pathways to anchorage-independent growth in cancer. *J. Cell Sci.* 124: 3189–3197.
49. Creed, S.J., C.P. Le, M. Hassan, C.K. Pon, S. Albold, K.T. Chan, M.E. Berginski, Z. Huang, J.E. Bear, J.R. Lane, M.L. Halls, D. Ferrari, C.J. Nowell, and E.K. Sloan. 2015. beta2-adrenoceptor signaling regulates invadopodia formation to enhance tumor cell invasion. *Breast Cancer Res.* 17: 145.
50. Doerschuk, C.M., N. Beyers, H.O. Coxson, B. Wiggs, and J.C. Hogg. 1993. Comparison of

- neutrophil and capillary diameters and their relation to neutrophil sequestration in the lung. *J. Appl. Physiol.* 74: 3040–3045.
51. Bathe, M., A. Shirai, C.M. Doerschuk, and R.D. Kamm. 2002. Neutrophil transit times through pulmonary capillaries: the effects of capillary geometry and fMLP-stimulation. *Biophys. J.* 83: 1917–33.
  52. Wirtz, D., K. Konstantopoulos, and P.C. Searson. 2011. The physics of cancer: the role of physical interactions and mechanical forces in metastasis. *Nat. Rev. Cancer.* 11: 512–522.
  53. Johnston, D.G. 1952. Cytoplasmic:nuclear ratios in the cytological diagnosis of cancer. *Cancer.* 5: 945–949.
  54. Foraker, A.G., and J.W. Reagan. 1956. Nuclear size and nuclear: cytoplasmic ratio in the delineation of atypical hyperplasia of the uterine cervix. *Cancer.* 9: 470–479.
  55. Pietuch, A., and A. Janshoff. 2013. Mechanics of spreading cells probed by atomic force microscopy. *Open Biol.* 3: 130084.
  56. Gardel, M.L., F. Nakamura, J.H. Hartwig, J.C. Crocker, T.P. Stossel, and D.A. Weitz. 2006. Prestressed F-actin networks cross-linked by hinged filamins replicate mechanical properties of cells. *Proc. Natl. Acad. Sci.* 103: 1762–1767.
  57. Park, C.Y., D. Tambe, A.M. Alencar, X. Treppe, E.H. Zhou, E. Millet, J.P. Butler, and J.J. Fredberg. 2010. Mapping the cytoskeletal prestress. *Am. J. Physiol. Cell Physiol.* 298: C1245-52.
  58. Jalilian, I., C. Heu, H. Cheng, H. Freittag, M. Desouza, J.R. Stehn, N.S. Bryce, R.M. Whan, E.C. Hardeman, T. Fath, G. Schevzov, and P.W. Gunning. 2015. Cell elasticity is regulated by the tropomyosin isoform composition of the actin cytoskeleton. *PLoS One.* 10: e0126214.
  59. Martens, J.C., and M. Radmacher. 2008. Softening of the actin cytoskeleton by inhibition of myosin II. *Pflugers Arch. Eur. J. Physiol.* 456: 95–100.
  60. Murrell, M., P.W. Oakes, M. Lenz, and M.L. Gardel. 2015. Forcing cells into shape: the mechanics of actomyosin contractility. *Nat. Rev. Mol. Cell Biol.* 16: 486–498.
  61. Wang, N., K. Naruse, D. Stamenovic, J.J. Fredberg, S.M. Mijailovich, I.M. Tolic-Norrelykke, T.

- Polte, R. Mannix, and D.E. Ingber. 2001. Mechanical behavior in living cells consistent with the tensegrity model. *Proc. Natl. Acad. Sci. U. S. A.* 98: 7765–7770.
62. Wang, N., I.M. Tolic-Norrelykke, J. Chen, S.M. Mijailovich, J.P. Butler, J.J. Fredberg, and D. Stamenovic. 2002. Cell prestress. I. Stiffness and prestress are closely associated in adherent contractile cells. *Am. J. Physiol. Cell Physiol.* 282: C606-16.
63. Kraning-Rush, C.M., J.P. Califano, and C.A. Reinhart-King. 2012. Cellular traction stresses increase with increasing metastatic potential. *PLoS One.* 7: e32572.
64. Chambers, A.F., A.C. Groom, and I.C. MacDonald. 2002. Dissemination and growth of cancer cells in metastatic sites. *Nat. Rev. Cancer.* 2: 563–572.
65. Denais, C.M., R.M. Gilbert, P. Isermann, A.L. McGregor, M. te Lindert, B. Weigelin, P.M. Davidson, P. Friedl, K. Wolf, and J. Lammerding. 2016. Nuclear envelope rupture and repair during cancer cell migration. *Science.* 352: 353–358.
66. Olson, M.F., and E. Sahai. 2009. The actin cytoskeleton in cancer cell motility. *Clin. Exp. Metastasis.* 26: 273–287.
67. Ma, C., B. Wu, X. Huang, Z. Yuan, K. Nong, B. Dong, Y. Bai, H. Zhu, W. Wang, and K. Ai. 2014. SUMO-specific protease 1 regulates pancreatic cancer cell proliferation and invasion by targeting MMP-9. *Tumour Biol.* 35: 12729–12735.
68. Zhao, X., S. Gao, H. Ren, W. Sun, H. Zhang, J. Sun, S. Yang, and J. Hao. 2014. Hypoxia-inducible factor-1 promotes pancreatic ductal adenocarcinoma invasion and metastasis by activating transcription of the actin-bundling protein fascin. *Cancer Res.* 74: 2455–2464.
69. Nabeshima, K., T. Inoue, Y. Shimao, and T. Sameshima. 2002. Matrix metalloproteinases in tumor invasion: role for cell migration. *Pathol. Int.* 52: 255–264.
70. Poincloux, R., O. Collin, F. Lizarraga, M. Romao, M. Debray, M. Piel, and P. Chavrier. 2011. Contractility of the cell rear drives invasion of breast tumor cells in 3D Matrigel. *Proc. Natl. Acad. Sci. U. S. A.* 108: 1943–1948.
71. Petrie, R.J., H. Koo, and K.M. Yamada. 2014. Generation of compartmentalized pressure by a





**S. Fig. 2 Correlation between experimental and predicted invasion of PDAC cells using physical phenotyping.**  $R^2$  and adjusted  $R^2$  ( $R_{adj}^2$ ) values of physical phenotyping models of invasion, which use varying sets of parameters. Blue bars represent  $R^2$  values; navy blue bars represent  $R_{adj}^2$  values, which reflect goodness of fit, while accounting for the number of parameters to data points. Colored circles illustrate the set of predictors.

	$D_{cell}$	$\epsilon_{max}$	$T_T$	$T_C$	$E_a$	$\beta$
$D_{cell}$	1.00	0.41	-0.02	0.07	-0.02	-0.14
$\epsilon_{max}$	0.41	1.00	0.06	0.17	-0.15	-0.10
$T_T$	-0.02	0.06	1.00	0.94	0.69	-0.52
$T_C$	0.07	0.17	0.94	1.00	0.72	-0.57
$E_a$	-0.02	-0.15	0.69	0.72	1.00	-0.88
$\beta$	-0.14	-0.10	-0.52	-0.57	-0.88	1.00

**S. Table 1. Pair-wise Spearman’s rank correlation coefficients.** Matrix of correlation coefficients for pairs of q-DC variables: cell diameter  $D_{cell}$ , maximum strain  $\epsilon_{max}$ , transit time  $T_T$ , creep time  $T_C$ , apparent elastic modulus  $E$ , and fluidity  $\beta$ . Correlation analysis is performed on the q-DC data for human breast and pancreatic cancer cell lines.